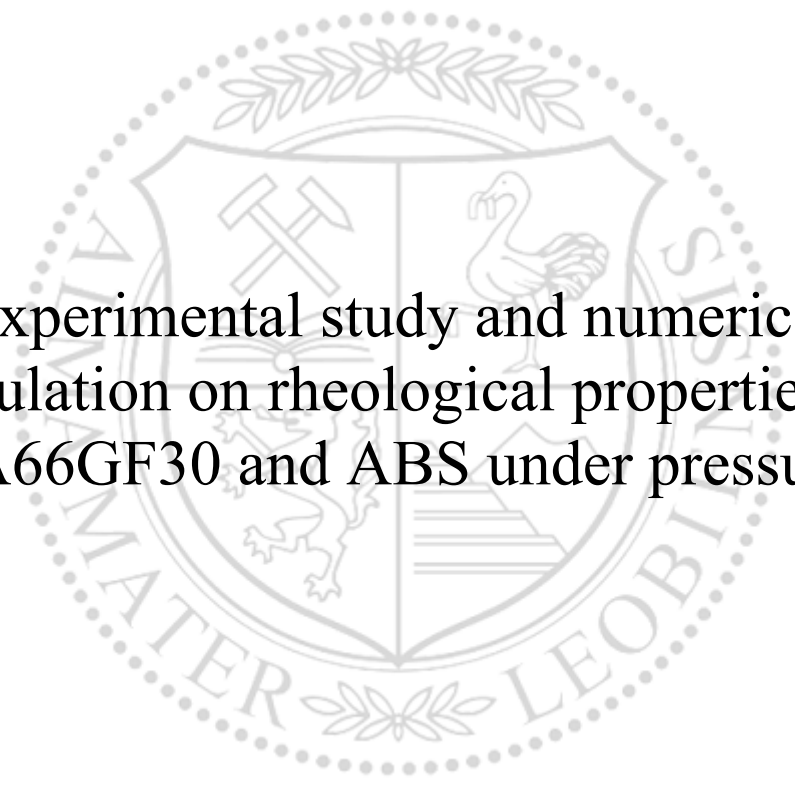




Chair of Injection Moulding of Polymers

Master's Thesis



Experimental study and numerical
simulation on rheological properties of
PA66GF30 and ABS under pressure

Fangxuan Gao

February 2021



EIDESSTÄTLICHE ERKLÄRUNG

I declare on oath that I wrote this thesis independently, did not use other than the specified sources and aids, and did not otherwise use any unauthorized aids.

I declare that I have read, understood, and complied with the guidelines of the senate of the Montanuniversität Leoben for "Good Scientific Practice".

Furthermore, I declare that the electronic and printed version of the submitted thesis are identical, both, formally and with regard to content.

Datum 13.01.2021

Fangxuan Gao

Signature Author
Fangxuan Gao

Abstract

The flow and deformation of the polymeric melt are necessary for the molding process of polymer materials. Theoretical analysis and experimental research help to understand the rheological behavior and characterizing the properties of the melts. It is the foundation for the rational selection of molding processes, optimization of processing equipment, and simulation of processing processes.

Mold filling during injection molding takes place via pressure flow. However, the influence of pressure on the rheological properties of the polymer melt is often ignored when simulating polymer flow. On the other hand, the study of the pressure dependence of the rheological properties is limited by the complexity of the characterization process and has therefore often been omitted. Moreover, the current researches on pressure-dependent rheological properties mainly focus on unfilled polymers, and the highly filled polymer compounds are hardly studied. In order to investigate the rheological properties of polymer melts and their highly filled compounds in the pressure range, the following studies were carried out in this work:

Through theoretical considerations and experimental studies, the shear viscosity of the polymer melt was analyzed in terms of its pressure dependence for the two polymer types acrylonitrile-butadiene-styrene copolymer (ABS) and polyamide 66 with 30 wt.% glass fibers (PA66GF30). Studies have shown that the rheological properties of polymer melts are significantly affected by the pressure in the pressure field. Therefore, the pressure dependence of viscosity is an important part of the analysis of the rheological behavior of the polymer melt.

The experiment was based on the modified high-pressure capillary rheometer, with a back-pressure chamber at the end of the die. By stepwise increase of the average pressure in the capillary, the pressure dependence of the shear viscosity of the polymer melt was achieved as a function of the shear rate. Two different calculation methods were used to calculate the viscosity pressure sensitivity coefficient of the material.

Experiments on two different materials found that under the same shear rate and pressure, as the stiffness of the polymer main chain increased, the pressure dependence decreased accordingly, and the addition of reinforcing materials also reduced the pressure dependence. At the same time, the study found that the viscosity pressure sensitivity coefficient of PA66GF30 first decreased and then increased with the increase of temperature. This was attributed to the fact that the polarity of strongly polar materials dominates at lower temperatures, while the effect is lower at high temperatures.

Finally, the flow in the capillary rheometer was simulated in Sigmasoft[®], and the actual pressure curve was compared with the simulation result to verify the calculation method. The verification result was shown that the pressure obtained from the simulation was 1%-7% lower than the actual measured pressure, explaining that the calculation method could be used to simulate the melt flow in the pressure field.

Keywords: ABS / polyamide 66 / viscosity / pressure dependence / flow simulation

KURZFASSUNG

Das Fließen und die Verformung der Polymerschmelze sind für den Formgebungsprozess von Polymeren notwendig. Theoretische Analyse und experimentelle Forschung helfen, das rheologische Verhalten zu verstehen und die Eigenschaften der Schmelzen zu charakterisieren. Es ist die Grundlage für die rationelle Auswahl von Formprozessen, die Optimierung von Verarbeitungsgeräten und die Simulation von Verarbeitungsprozessen.

Die Formfüllung beim Spritzgießen erfolgt über eine Druckströmung. Der Einfluss des Drucks auf die rheologischen Eigenschaften der Polymerschmelze wird bei der Simulation der Polymerströmung jedoch häufig ignoriert. Andererseits ist die Untersuchung der Druckabhängigkeit der rheologischen Eigenschaften durch die Komplexität des Charakterisierungsverfahrens begrenzt und wurde deshalb häufig unterlassen. Darüber hinaus konzentrieren sich die aktuellen Forschungen zu druckabhängigen rheologischen Eigenschaften hauptsächlich auf ungefüllte Polymere, und die hochgefüllten Polymer-Compounds sind kaum untersucht. Um die rheologischen Eigenschaften von Polymerschmelzen und ihrer hochgefüllten Compounds im Druckbereich zu untersuchen, wurden in dieser Arbeit folgende Untersuchungen durchgeführt:

Durch theoretische Überlegungen und experimentelle Untersuchungen wurde die Scherviskosität der Polymerschmelze im Hinblick auf deren Druckabhängigkeit für die zwei Polymertypen Acrylnitril-Butadien-Styrol-Copolymer (ABS) und Polyamid 66 mit 30 Gew.% Glasfasern (PA66GF30) analysiert. Studien haben gezeigt, dass die rheologischen Eigenschaften von Polymerschmelzen durch den Druck im Druckfeld signifikant beeinflusst werden. Daher ist die Druckabhängigkeit der Viskosität ein wichtiger Bestandteil der Analyse des rheologischen Verhaltens der Polymerschmelze.

Die Versuche wurden mit dem modifizierten Hochdruckkapillarrheometer mit einer Gegendruckkammer am Ende der Düse durchgeführt. Durch stufenweise Erhöhung des mittleren Drucks in der Rheometer-Kapillare wurde der Druckkoeffizient der Scherviskosität in Abhängigkeit von der Schergeschwindigkeit gemessen. Zwei verschiedene Berechnungsmethoden wurden verwendet, um den Druckkoeffizienten der Scherviskosität der beiden Polymere zu ermitteln.

Experimente an zwei verschiedenen Materialien ergaben, dass bei gleicher Schergeschwindigkeit und gleichem Druck mit zunehmender Steifheit der Polymerhauptkette die Druckabhängigkeit entsprechend abnahm und die Zugabe von Verstärkungsmaterialien auch die Druckabhängigkeit verringerte. Gleichzeitig ergab die Studie, dass der Druckkoeffizient der Scherviskosität von PA66GF30 mit steigender Temperatur zuerst abnahm und dann wieder zunahm. Dies wurde auf die Tatsache zurückgeführt, dass die Polarität stark polarer Materialien bei niedrigeren Temperaturen dominiert, während der Effekt bei hohen Temperaturen geringer ist.

Schließlich wurde die Hochdruckkapillarrheometer-Strömung in Sigmasoft® simuliert und die tatsächliche Druckkurve mit dem Simulationsergebnis verglichen, um die Berechnungsmethode zu verifizieren. Das Verifizierungsergebnis zeigt, dass der aus der Simulation erhaltene Druck 1% -7% niedriger als der tatsächlich gemessene Druck ist. Daraus kann gefolgert werden, dass die Berechnungsmethode geeignet ist, die Rheometerströmung in der Kapillare zu simulieren.

Schlüsselwörter: ABS / Polyamid 66 / Viskosität / Druckabhängigkeit / Fließsimulation

Table of Contents

1	INTRODUCTION	1
2	THEORETICAL BACKGROUND	3
2.1	INTRODUCTION OF ABS AND PA66GF30	3
2.1.1	ABS Resin	3
2.1.2	Polyamide 66.....	4
2.2	RHEOLOGICAL PROPERTIES AND CONSTITUTIVE EQUATION MODELS OF POLYMERS.....	8
2.2.1	Pressure dependence of viscosity.....	11
2.3	EXPERIMENTAL PRINCIPLE	12
2.3.1	High pressure capillary rheometer (HPCR).....	13
2.3.2	Rotational rheometer	14
2.3.3	Pressure-specific volume-temperature (pvT) relationship.....	15
2.3.4	Differential scanning calorimetry (DSC)	18
2.3.5	Transient line source (TLS)	19
2.3.6	Modified high pressure capillary rheometer	20
2.4	COMPUTER SIMULATION	22
2.4.1	Introduction to SIGMASOFT ® VIRTUAL MOLDING.....	23
2.5	CURRENT STATUS OF RESEARCH ON PRESSURE DEPENDENT RHEOLOGY	24
3	EXPERIMENTAL DETAILS	27
3.1	MATERIAL AND EQUIPMENT.....	27
3.1.1	Material	27
3.1.2	Equipment	27
3.2	METHODS.....	28
3.2.1	Dryer	28
3.2.2	High pressure capillary rheometer	28
3.2.3	Rotational rheometer	29
3.2.4	pvT relationship.....	29
3.2.5	DSC.....	29
3.2.6	Thermal conductivity.....	30
3.2.7	Modified high pressure capillary rheometer	30
3.3	RESULTS AND DISCUSSION	31
3.3.1	Thermal data.....	31
3.3.2	pvT data	33
3.3.3	The effect of residence time on PA66GF30	35
3.3.4	Low shear rate viscosity of ABS and PA66GF30.....	35
3.3.5	High shear rate viscosity of ABS and PA66GF30 materials	37
3.3.6	The influence of pressure on the shear viscosity of ABS and PA66GF30.....	38
4	NUMERICAL FITTING BASED ON SIGMASOFT ® VIRTUAL MOLDING	49
4.1	HIGH PRESSURE CAPILLARY RHEOMETER SIMULATION	49
4.1.1	3D model	49
4.1.2	Meshing	50
4.1.3	Setting process data	52
4.2	NUMERICAL RESULTS	57
4.2.1	Influence of mesh size	60
4.2.2	Influence of data processing	61

Table of Contents

4.2.3	Comparison of simulation results and experimental results	62
5	SUMMARY.....	66
6	REFERENCES	68
7	ABBREVIATIONS AND SYMBOLS.....	72
8	LIST OF TABLES.....	73
9	LIST OF FIGURES	74
10	APPENDIX	77

1 Introduction

Since the birth of the first synthetic plastic in the early 20th century, the polymer industry has gradually developed. Compared with traditional materials such as metal and wood, polymer materials have the advantages of low cost, small density, corrosion resistance, and good plasticity. Polymer products have been widely used in automobiles, electromechanics, instrumentation, aerospace, and other fields. By volume, it has exceeded the total annual output of steel and non-ferrous metals and has become the most widely used material in daily life.

The polymer is a synthetic or natural polymer compound as the basic component, which can be molded into shape during processing, and the product can be a material that retains its shape in the end. Most polymers are based on synthetic polymer compounds, namely synthetic resins, and contain auxiliary materials such as fillers, plasticizers, and stabilizers.

There are many different production methods for polymer material products according to different material properties and use conditions, mainly including extrusion, injection molding, hot press molding, gas-assisted molding, etc. In recent years, due to the rapid development of technology and the economy, more and more products are pursuing consumer customization and diversified production. Therefore, additive manufacturing has gradually become the core of the polymer industrial-technological revolution. As early as 1988, the 3D system company successfully launched the first commercial 3D printer, opening a milestone in additive manufacturing. According to EU research, the market size of additive manufacturing is expected to reach 11 billion U.S. dollars in 2021 [1].

To shorten the development time of injection molded parts, even for more and more special compounds, process simulations, and rapid and accurate measurement of rheological data are required in different development steps. Conventional molding analysis software often considers polymer fluids to be incompressible fluids, so they usually have fixed parameters in general material fluidity databases. For thin-wall molding, the injection pressure will exceed $2 \cdot 10^8 \text{Pa}$ (2000 bar). Therefore, the influence of pressure on fluidity is extremely important, so additional measurements are required [2].

In polymer molding, material flow properties, pressure-volume-temperature relationship (PVT relationship), and thermodynamic physical parameters are an important basis for mold design, process control, and control of the final product performance. At the same time, with CAD/CAM/CAE with the wide application of technology in the plastics processing industry, the study of polymer material properties is particularly important. At present, the computer molding simulation analysis software on the market, such as Autodesk Moldflow Insight, Cadmould 3D-F, Moldex3D, SIGMASOFT, etc., all have only the material parameters of polymer materials produced by some manufacturers, so that the final analysis is only an approximate result. Therefore, it is necessary to carry out corresponding material performance research on the commonly used polymer materials of different manufacturers to establish a material database of the corresponding materials, which is of great significance for the future development of simulation molding analysis software. At the same time, with the continuous improvement of product performance requirements, more and more composite polymers have begun to be applied, which has also increased the urgency of establishing a database for related materials.

The aim of the present thesis is to improve the knowledge of the rheology of the polymer and the influence of the pressure on the rheology by studying the rheological parameters of acrylonitrile-butadiene-styrene copolymer (ABS) and polyamide 66 containing 30% volume content of glass fiber (PA66GF30). Furthermore, the correlation between the pressure and the

rheological parameters was investigated. The polymer was tested following a design of experiments (DOE). The DOE included a variation in temperature, shear rate, and pressure. Viscosity versus shear rate curve, pressure-volume-temperature (pVT) relation, specific heat capacity (C_p), and thermal conductivity (λ) were measured as most important material parameters. The influence of the pressure was measured by a modified high pressure capillary rheometer, which added a back-pressure chamber at the end of the die. From the results, a relationship between pressure and the shear viscosity was built.

Since simulation plays an important role in today's processing industry, simulations of the rheometer flow in the high pressure capillary rheometer (HPCR) using Sigmasoft® were carried out as well. The parameters, which were used in the simulations, were determined by the experiments. The focus of the simulation lay on comparing the pressure difference between the experimental results and the simulation results, and the results assessed the accuracy of the influence of pressure.

Figure 1.1 shows the scientific approach of this thesis for better understanding.

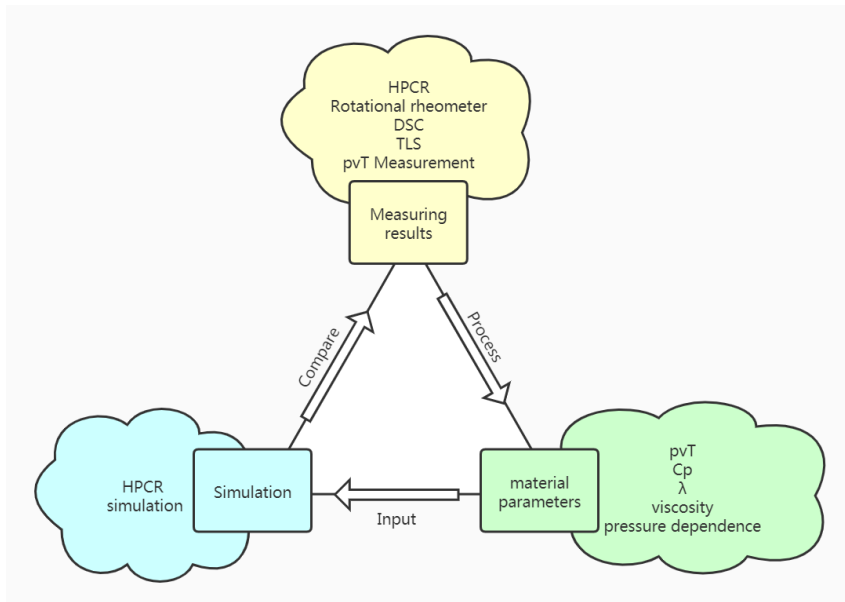


Figure 1.1: Scientific approach of this thesis

2 Theoretical Background

2.1 Introduction of ABS and PA66GF30

The polymer is a high molecular material formed out of synthetic or natural source materials. Polymer can be molded into shapes after processing, and the final product can maintain the same shape. The choice of polymer mainly considers its mechanical properties (strength, impact performance, toughness, etc.), chemical properties (corrosion resistance, flame retardancy, etc.), physical properties (use temperature, etc.), and its processing properties (fluidity, heat sensitivity, etc.). According to the crystalline state, it can be divided into semi-crystalline polymers and amorphous polymers. The material Acrylonitrile-Butadiene-Styrene (ABS) and Polyamide 66 (PA66) were used in this thesis. ABS is an amorphous polymer, and PA66 is a semi-crystalline polymer.

2.1.1 ABS Resin

ABS has been commercialized since the 1940s, and its sales have increased year by year. It has become the world's largest-selling engineering thermoplastic [3]. Among commodity plastics and high-performance engineering thermoplastics, ABS occupy a unique "transition" polymer position.

ABS resin refers to a terpolymer composed of acrylonitrile (A), butadiene (B), and styrene (S) and its modified resin. It has the advantages of wide sources of raw materials, low price, easy molding and processing, and excellent impact performance [4]. Its structural formula is as Figure 2.1:

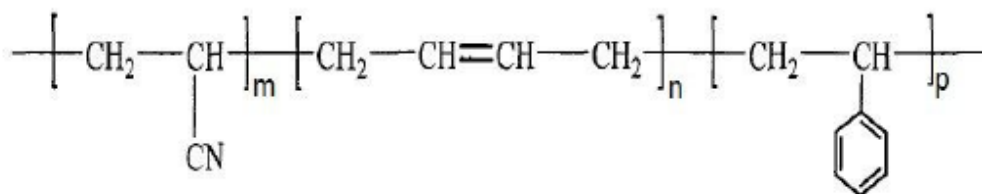


Figure 2.1 Structure of ABS [5]

There are many methods for producing ABS resin. At present, the industry methods include emulsion graft polymerization, emulsion graft blending, emulsion-bulk polymerization, and continuous bulk polymerization.

2.1.1.1 ABS resin properties

ABS is a light-yellow powder or granular opaque resin, non-toxic and tasteless. It has excellent impact resistance, good low-temperature performance and chemical resistance, good dimensional stability, good surface gloss, and easy coating and coloring. The disadvantage is that it is combustible, the heat distortion temperature is relatively low, and the weather resistance is poor.

The versatility of ABS comes from its three monomer structural units acrylonitrile, butadiene, and styrene [6]. Each component provides a different set of useful properties for the final polymer. Acrylonitrile mainly provides chemical resistance and thermal stability; butadiene provides impact strength; the styrene component provides hardness and workability for ABS. ABS resin is a two-phase system. Styrene-acrylonitrile copolymer (SAN) is the continuous

phase. Butadiene-derived rubber is the elastomer dispersed phase. ABS is an amorphous thermoplastic, which softens within a certain temperature range instead of suddenly melting. ABS is slightly hygroscopic and should be dried before melting. ABS materials easily accept common post-processing such as machining, bonding, fastening, electroplating, painting, etc. ABS material has a wide range of processing operating conditions and has good shear thinning flow characteristics.

The density of ABS resin is about 1.07 g/cm^3 , and it has excellent impact strength. The Charpy notched impact strength at room temperature is 11.8 KJ/m^2 . Even at a low temperature of -40°C , its value can reach 8.4 KJ/m^2 . The tensile strength of ABS resin has a wide range, and the available range is $2.6\sim 73.1 \text{ MPa}$ [7]. ABS resin has good creep resistance, good wear resistance, and good dimensional stability, making it suitable for making gears and bearings.

The heat distortion temperature of ABS resin is about 90°C under a load of 1.8 MPa , and some heat-resistant varieties can reach 114°C [7]. The amorphous structure of ABS resin leads to a stable stress-temperature effect, so the reduction of the load makes the heat distortion temperature increase limited. However, ABS resin is easy to ignite spontaneously and has no self-extinguishing properties, making its use subject to many restrictions.

ABS resin has a better chemical resistance compared to Polycarbonate (PC), Polystyrene (PS) and Polyamide 66 (PA66) [8]. Due to the presence of nitrile groups in its molecular structure, it is hardly affected by dilute acids, dilute alkalis, and salts, but it can be dissolved in ketones, aldehydes, esters, and chlorinated hydrocarbons [4]. It is insoluble in most alcohols such as ethanol, but it will soften after a few hours in methanol; although it is insoluble in hydrocarbon solvents, it will swell in long-term contact with hydrocarbon solvents. Under stress, the surface of ABS resin is corroded by chemical agents such as acetic acid and vegetable oil, which will cause stress cracking.

2.1.1.2 ABS resin processing performance

ABS is an amorphous polymer with no obvious melting point. It begins to decompose when heated above 267°C . Usually, the molding temperature of ABS is controlled below 250°C . The melt viscosity of ABS resin is moderate, its fluidity is slightly worse than polyamide but better than polycarbonate, and the melt has a faster cooling and solidification speed. Increasing the barrel temperature and increasing the injection speed can improve the melt fluidity of the ABS resin. Because ABS resin contains strong polar groups such as cyano groups, it has high water absorption, and the saturated water absorption rate can reach 0.495% at room temperature. It should be pre-dried before processing to reduce its moisture content to below 0.1% . The commonly used drying method is circulating blast drying, the temperature is controlled at 70°C to 80°C , and the time is more than 4 hours [7].

2.1.2 Polyamide 66

Polyamide, with a common name Nylon, is a general term for thermoplastic resins containing repeating amide groups on the molecular backbone and is considered to be the second most important human-made polymer textile since polyester [9]. Since Wallace H. Carothers of DuPont Company invented PA in the 1930s, the output of PA has ranked first in engineering plastics [10].

Polyamide is a semi-crystalline polymer material. There are strong hydrogen bonds between molecular chains, which make it have good crystallinity, excellent toughness, self-lubricating, abrasion resistance, chemical resistance, gas permeability, The advantages of oil resistance, non-toxicity, and easy coloring. When the temperature exceeds its melting point, its melt viscosity is small and its fluidity is excellent, but because the melt condenses fast, its melt

viscosity is more sensitive to temperature and shear changes, especially more sensitive to temperature. At the same time, the high water absorption of PA materials and the reaction between water molecules and amide groups at high temperatures limit the range of PA materials used. PA fiber products cover a variety of textiles, clothing, and industrial products.

Polyamide has many varieties, large output and wide application. It can be used as plastic and fiber. PA can be made by polycondensation of diamine and diacid, or it can be made by self-condensation of amino acid. The name of the PA produced by the former is determined by the number of carbon atoms in diamine and diacid; the latter is determined by the number of carbon atoms in amino acids.

The main characteristics of polyamide are excellent mechanical properties, such as high strength, good rigidity, good wear resistance, and self-lubricating [11]; the use temperature range is wide, generally $-40^{\circ}\text{C}\sim 100^{\circ}\text{C}$; the electrical insulation performance is good; good flame retardancy, self-extinguishing; good oil resistance and chemical stability; easy to process are further characteristics. The main varieties of PA are PA 6 and PA66, whose output accounts for about 90% of the total PA output.

Polyamide 66 is the first PA variety to be successfully developed. It was invented and industrialized by DuPont in 1935. PA66 is formed by polycondensation of adipic acid and hexamethylenediamine [12]. Its production process mainly includes three processes: monomer synthesis, PA66 salt preparation, and polycondensation. Its structural formula is as Figure 2.2:



Figure 2.2: Structure of PA66 [13]

2.1.2.1 PA66 properties

PA66 is a translucent or opaque milky white crystalline resin. It has high strength, rigidity and toughness in a wide temperature range, excellent wear resistance, creep resistance and self-lubricity. It has good heat resistance, low temperature resistance, excellent oil resistance and is a self-extinguishing material. However, the water absorption is large, and the dimensional stability of the product is poor. The mechanical properties of PA66 mainly depend on the chemical bonds of its molecular chain and intermolecular forces. The breaking of chemical bonds on the molecular chain and the interference of intermolecular forces will directly lead to changes in the properties of PA polymers.

PA66 has a density of about 1.17 g/cm^3 and has excellent impact strength. The Charpy notched impact strength at room temperature is 13.5 KJ/m^2 , even at a low temperature of -40°C , its value can reach 7.81 KJ/m^2 . The tensile strength of PA66 resin has a wide range, and the available range is $7.52\sim 260 \text{ MPa}$ [14]. However, too many polar groups will hinder the mobility of the main chain, thereby reducing the toughness of PA and increasing its brittleness. Flexural strain at break is only 7.41 %.

PA66 has excellent heat resistance, with a melting point of 278°C [14]. The heat distortion temperature of PA66 is closely related to the load it bears. For example, when the load is 0.46 MPa , its heat distortion temperature is as high as 216°C , and when the load increases to 1.8

MPa, its heat distortion temperature rapidly drops to 94.9°C [14]. When the load is constant, the heat distortion temperature of PA66 decreases with the increase of water absorption.

At the same time, PA66 has a hydrogen-containing amino group in its molecular structure, and its concentration is high, so it has good flame retardancy and self-extinguishing. In the Flammability UL94 test, the sample will be extinguished within 10 seconds [14].

2.1.2.2 PA66 processing performance

PA66 is a semi-crystalline polymer with a melting point of about 258°C, and the molding temperature of ABS is usually controlled at about 280°C [14].

The amide groups on the main chain of PA molecules can form hydrogen bonds with the amide groups of neighboring molecules and easily form hydrogen bonds with water molecules. Therefore, PA has a strong hygroscopy. Moreover, this will bring the following problems to PA66 processing:

- a) In the molten state, PA is easily hydrolyzed, especially PA66. The hydrolysis reaction degrades the polymer, resulting in a decrease in the strength of PA products [15].
- b) Due to the hydrolysis reaction of PA during the melting process, the low molecules produced by the degradation will form gases at high temperatures. Without exhaust devices, these gases and water vapor will be stored in part, which will form markings on the surface. Silver streaks, bubbles, and micro-pores affect the surface quality of parts.
- c) High moisture absorption affects the dimensional stability of PA parts. The size of PA products changes after absorbing water, especially when thin-walled products absorb moisture and cause the products to warp and deform.
- d) PA has poor dimensional stability and good water absorption, so pay attention to the drying of PA.

It should be pre-dried before processing to reduce its moisture content to below 0.15 %. The commonly used drying method is vacuum drying. The temperature is controlled at 70°C~80°C, and the vacuum degree is controlled below 500 mbar. At this time, the dew point temperature is controlled below -20°C, and the time is more than 4 hours [14].

2.1.2.3 Fiber reinforced PA66

Plastic products have been widely used in various fields due to their low price, good formability, high specific strength, and good insulation. However, ordinary plastic products in high-end fields such as automobiles, mechanical equipment, aerospace, and electronic appliances have become increasingly difficult to meet performance requirements, such as the high-strength requirements of automobile dashboards. To solve this problem, reinforcing fibers are often added to plastics to form fiber-reinforced composite materials. Compared with ordinary plastics, fiber-reinforced plastics have the advantages of higher specific strength, higher specific modulus and good fatigue resistance. The material composition and performance can be designed according to performance requirements [11].

Compared with pure PA66, glass fiber reinforced PA66 has the following advantages: High mechanical strength, good rigidity (modulus of elasticity is more than 1 times larger than PC); heat distortion temperature is 50-60°C higher than PA [16]; resistance to dynamic fatigue performance is well, so the glass fiber reinforced PA66 is used as a structural material; in addition, the internal stress is small so that will not cause cracking. The disadvantage of glass fiber reinforced PA66 is that its impact toughness is worse than that of pure PA; due to the penetration of glass fibers, the appearance of the part is poor, and the glass fiber will be exposed if it is processed carelessly. Therefore, the black color is often used to reduce the effect, which also limits the conditions of usage; especially its anisotropy of molding shrinkage,

resulting in parts prone to warpage and deformation, which lead to the difficulties of the molding process, parts, and mold design.

In the glass fiber composite material, glass fiber is the main load-bearing component. Because the wave fiber is composed of a mixture of alkali metal oxides with strong water absorption dispersed in a SiO₂ network structure, it is exposed to the atmosphere. The surface will adsorb a layer of water molecules. When the composite material is formed, the water existing on the glass fiber-matrix interface will affect the adhesion of the glass fiber and the resin matrix and damage the fiber and degrade the resin, thereby reducing the performance of the composite material. Therefore, its surface treatment has also become a key technology and important process for composite material manufacturing. The surface treatment can form a firm bond between the glass fiber and the synthetic resin so that its various properties can be improved. The general surface treatment means that the surface of the glass fiber is treated with a coupling agent to be well combined with the matrix [16].

It is generally believed that the mechanical properties of glass fiber reinforced PA66 increase with the increase of glass fiber content within the allowable range, but when the content exceeds 50%, the performance increase is hindered; at the same time, the increase in glass fiber content will reduce the processing fluidity [16]. The molding process becomes worse. With the increase of glass fiber content, there are more glass fibers on any cross-section of the composite material. The extraction or break of these glass fibers requires a greater load, thus increasing the tensile strength and bending strength of the composite material. At the same time, due to the increase in the volume content of the glass fiber, that is, the thinning of the resin layer between the glass fibers, the stress acting on the composite material is easily transmitted in the glass fiber through the resin layer, and the deformation of the resin is also affected by the glass fibers. Constraint, so the flexural modulus of elasticity also increases with the increase of glass fiber content. Considering the performance and processing technology, the glass fiber content in the production of glass fiber reinforced PA66 is generally controlled at 30% to 50% [17].

Table 2.1 lists the Properties of ABS, pure PA66, and PA66-GF30

Table 2.1: ABS /PA66 /PA66-GF30 properties [7; 14; 18]

Properties	Unit	ABS	PA66	PA66-GF30
Density ρ	g/cm ³	1.07	1.17	1.38
Tensile Yield Strength, at 23°C	MPa	45	72.3	154
Yield Elongation at 23°C	%	3.2	14.9	3.88
Modulus of Elasticity	GPa	2.32	2.72	8.45
Break Elongation	%	28.8	47.3	4.06
Flexural Yield Strength	MPa	73.6	105	228
Flexural Modulus	GPa	2.35	3.18	7.82
Charpy Notched Impact, at 23°C	J/cm ²	1.88	1.35	1.23
Ball Indentation Hardness	MPa	101	138	207
Processing Temperature	°C	207	252	248
Thermal Conductivity	W/m·K	0.158	0.882	0.359

Properties	Unit	ABS	PA66	PA66-GF30
Melting Point	°C	238	278	284

2.2 Rheological properties and constitutive equation models of polymers

The rheological properties of polymer melts are completely different from those of Newtonian fluids such as water and air, and they have some special rheological behaviors. In Figure 2.3 the shear stress versus shear rate diagram for general types of fluids is shown.

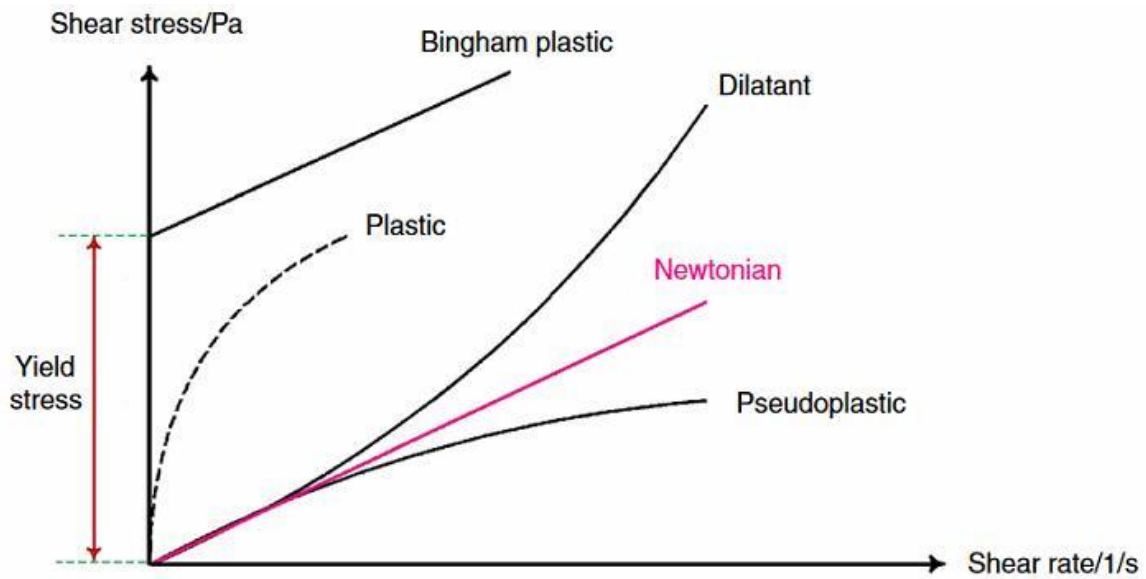


Figure 2.3: Comparison of shear stress versus shear rate diagram for Newtonian and non-Newtonian fluids [19]

Polymer melts compared with a Newtonian fluid has the following unique phenomena:

- 1) Weissenberg effect: the polymer will be oriented and stretched along the circumferential direction due to rotation, causing the polymer fluid to generate centripetal pressure under the action of elasticity, causing the polymer fluid to climb along the axis of rotation, shown in Figure 2.4.

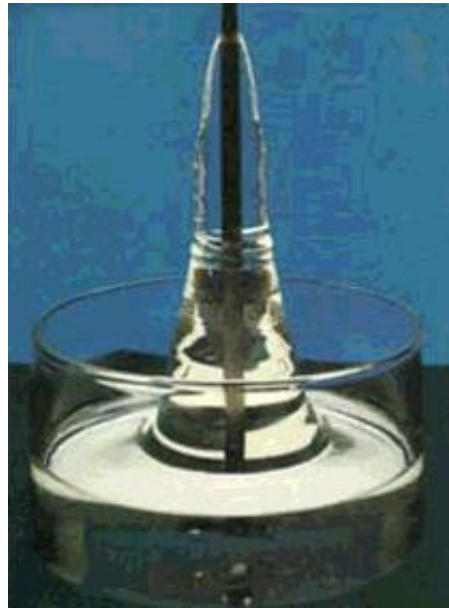


Figure 2.4: Weissenberg Effect [20]

2) Die swell phenomenon: Because the polymer melt undergoes high elastic deformation under the action of external force when passing through the capillary orifice, the external force is eliminated when it leaves the orifice and returns to its original shape. Therefore, the polymer swells when it leaves the capillary orifice. The body diameter is significantly larger than the pipe mouth, while the Newtonian fluid is almost the same as the pipe diameter, shown in Figure 2.5.

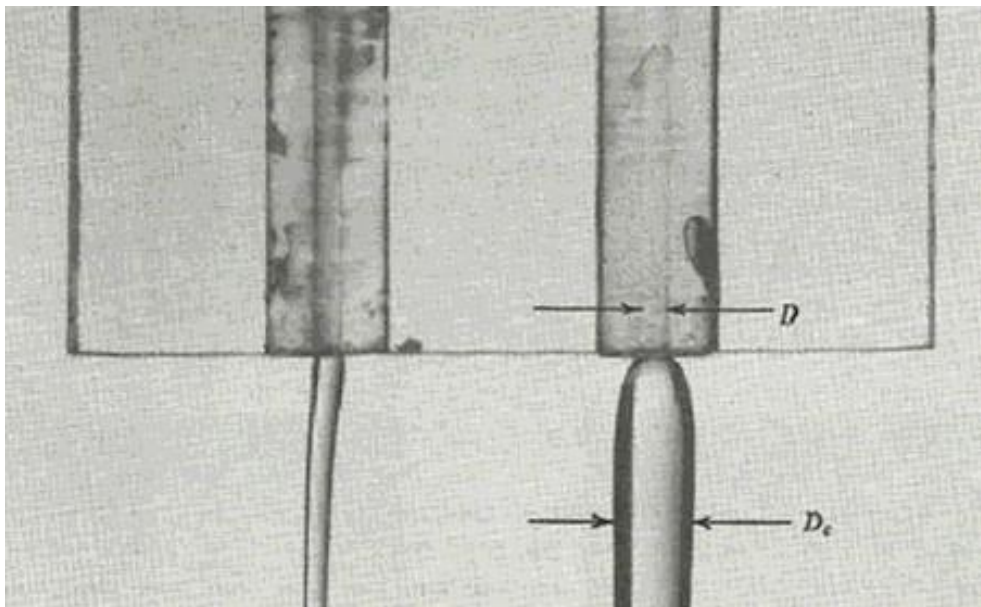


Figure 2.5: Die swell of a Newtonian (left) versus a polymeric (right) liquid [20]

In 1839, Hagen [21] developed the world's first capillary rheometer to measure the viscosity of water. After that, Rabinowitsch and Weissenberg [22] provided a formula for calculating the shear rate of a non-Newtonian fluid in a capillary. The measured rate of change of flow versus shear stress gives the shear rate. At the same time, Bagley [23] also proposed a capillary pressure correction. The pressure drop in the entrance area is equivalent to the pressure drop

over the virtual extension length, eliminating the influence of the entrance pressure drop on the calculation of shear stress. After this, Wales, Den Otter, and Janeschitz-Kriegl [24] used a slit die to eliminate the influence of entrance pressure drop on the calculation of shear stress and solved the problem of installing a pressure sensor in the die.

The viscosity of a Newtonian fluid is a fixed value, which conforms to the following equation(2.1):

$$\tau = \mu \cdot \dot{\gamma} \quad (2.1)$$

Where τ is the shear stress, $\dot{\gamma}$ is the shear rate, μ is the viscosity parameter.

Generally, for polymer melts, the shear viscosity decreases as the shear rate increases, which is called a pseudoplastic or shear-thinning fluid. At the same time, the conditions (such as temperature, pressure), molecular weight, additives, and other factors will affect the shear viscosity of the polymer melt, so it is a complicated system as shown in Figure 2.6.

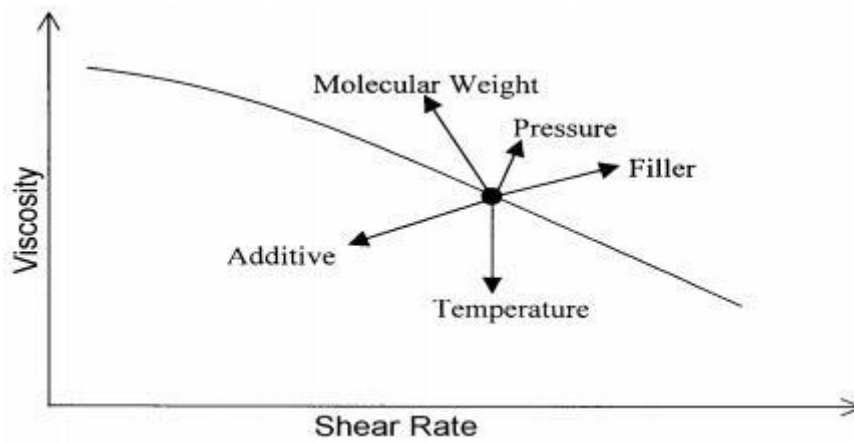


Figure 2.6: Factors influencing the viscosity of polymer melts [25]

The viscosity coefficient of the polymer melt is usually not a constant to distinguish it from Newtonian fluids. The shear viscosity is usually used as the viscosity coefficient, shown in equation(2.2).

$$\tau = \eta(\dot{\gamma}, T, p, \bar{M}) \cdot \dot{\gamma} \quad (2.2)$$

To describe the relationship between the shear rate and viscosity of non-Newtonian fluids, rheologists have proposed many constitutive equation models, including power law model, Bingham model, cross model, Carreau model, and their modified models.

Ostwald-DeWaele model (power law model) [26] is the most commonly used model, and its form is as follows:

$$\eta = K \cdot \dot{\gamma}^{n-1} \quad (2.3)$$

Where K is a constant, n is the power rate index, when $n=0$, it is a Newtonian fluid, and when $n>1$, it is shear thickening or called dilatant fluid, when $n<1$, it is shear thinning or called pseudoplastic fluid.

The characteristic of the Bingham model is that it can flow only when the shear stress is greater than a certain value, and its form [26] is as follows:

$$\eta = \frac{\tau - \tau_0}{\dot{\gamma}} \quad (2.4)$$

Where τ_0 is the yield shear stress.

The Cross model [27] form is as follows:

$$\frac{\eta - \eta_\infty}{\eta_0 - \eta_\infty} = \frac{1}{1 + (K \cdot \dot{\gamma})^{1-n}} \quad (2.5)$$

Where η_0 is the zero shear rate viscosity, η_∞ is an infinite shear viscosity, K is a fitting constant, n is the power rate index. When the viscosity is much smaller than zero shear viscosity and much larger than infinite shear rate, ($\eta_0 \gg \eta \gg \eta_\infty$) this model is equivalent to a power law model.

The Carreau model [28] has the following form:

$$\eta = \frac{\eta_0}{(1 + \lambda \cdot \dot{\gamma})^{1-n}} \quad (2.6)$$

Where λ is a time fitting parameter. It represents the shear rate required from quasi-Newtonian flow behavior to pseudoplastic fluid.

Modified Carreau model [28]:

$$\eta = \frac{\eta_0}{(1 + (\lambda \cdot \dot{\gamma})^\alpha)^{(1-n)/\alpha}} \quad (2.7)$$

Where α is a fitting parameter. The radius of curvature between the area of the quasi-Newtonian flow behavior and the power law area can be better adapted, shown in Figure 2.7.

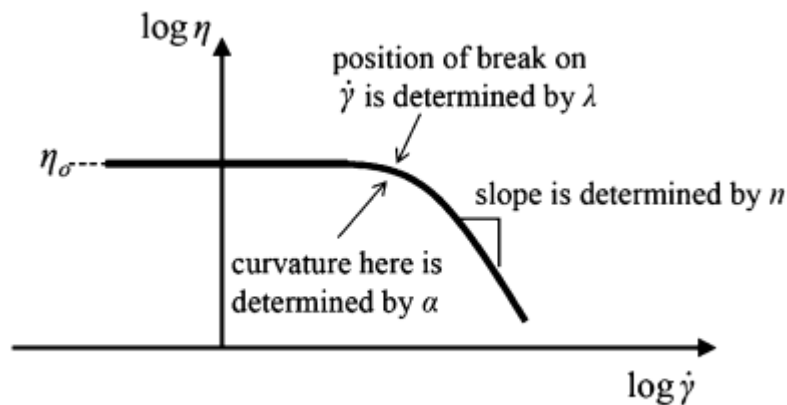


Figure 2.7: Meaning of Carreau model parameters [28]

2.2.1 Pressure dependence of viscosity

Stress, time, temperature, and pressure are the most important parameters that affect rheological properties [29]. While the stress, time, and temperature dependence of viscosity are well established, the pressure dependence of rheological properties is still usually ignored, although the pressure in processing operations such as extrusion and injection molding is high enough to significantly affect the rheological behavior of the material. At the present time, the experimental challenge is mainly to design a rheometer that can operate at pressures

comparable to those in polymer processing and with accurate measurement of the high pressures that occurs [29]. Another difficulty is the comparison from the various methods and materials due to the different molecular structures and weights. Despite these difficulties, a number of articles related to pressure have been published in the past 20 years.

At present, there are mainly three theoretical studies on the dependence of viscosity on pressure, 1) free volume and Doolittle equation theory, 2) WLF equation and pressure dependence of the glass temperature theory, 3) Somcynsky and Simha (SS) hole theory [29].

- 1) Free volume and Doolittle equation theory: This theory was proposed by Ferry [30] and is considered the standard theory. The theory considers that the volume of the polymer V is composed of the occupied volume of polymer chains V_0 and free volume V_f as shown in equation(2.8). As the pressure increases, the free volume is compressed, and the distance between the molecular chains becomes smaller, which makes chains difficult to move, so the viscosity increases, which is described in the Doolittle equation (2.9) [31].

$$V = V_0 + V_f \quad (2.8)$$

$$\eta = K \cdot e^{\left(\frac{N V_0}{V_f}\right)} \quad (2.9)$$

Where K , N are constants.

- 2) WLF equation and pressure dependence of the glass temperature theory [32]: The WLF equation describes the temperature shift factor $\alpha_T(T, T_0)$ for the Newtonian viscosity. With glass temperature T_g as reference temperature, the WLF equation can be written as equation (2.10)

$$\log \alpha_T(T, T_g) = \log \frac{\eta_0(T)}{\eta_0(T_g)} = -\frac{C_1(T - T_g)}{C_2 + (T - T_g)} \quad (2.10)$$

Where η_0 is the zero shear viscosity. Using this equation and assuming a linear pressure dependence of the glass transition temperature, a relation for the pressure dependence of the viscosity was developed [33].

- 3) SS hole theory[34]: This theory considers a mixture of occupied and empty volumes, which are called holes. The hole fraction h can be determined by the pVT diagram. Considering the hole fraction, the viscosity can be written as

$$\ln \eta_0 = \ln b_0 + b_1 h' / h \quad (2.11)$$

Where b_0 and b_1 are constants, h' is a factor correcting h . According the equation (2.11), master curves of viscosity at various pressures and temperatures should be expected.

2.3 Experimental Principle

Normally different experiments are used to obtain material parameters. In this thesis, high pressure capillary rheometer (HPCR), rotational rheometer, pressure-specific volume-temperature (pvT) relationship, differential scanning calorimetry (DSC), transient line source (TLS) and modified HPCR were used.

2.3.1 High pressure capillary rheometer (HPCR)

Most thermoplastic injection molding is done in a high shear rate rheological process in the molten state. In this process, the pressure field and temperature field during processing not only determine the appearance, shape, and quality of the material product but also have a very important influence on the formation of the material chain structure, polymer structure, and state. Therefore, it is of practical significance to study the high shear rate rheology of materials in the processing process, rationally design and correctly operate the polymer processing process and polymer processing technology, obtain products with excellent performance, and achieve the goal of high quality and high efficiency.

High pressure capillary rheometer is currently a widely used rheometer. Its main advantages are the simple device, easy operation, wide range of measured shear rate, and material flow similar to the real processing of polymer materials. Therefore, it has a wider practical value.

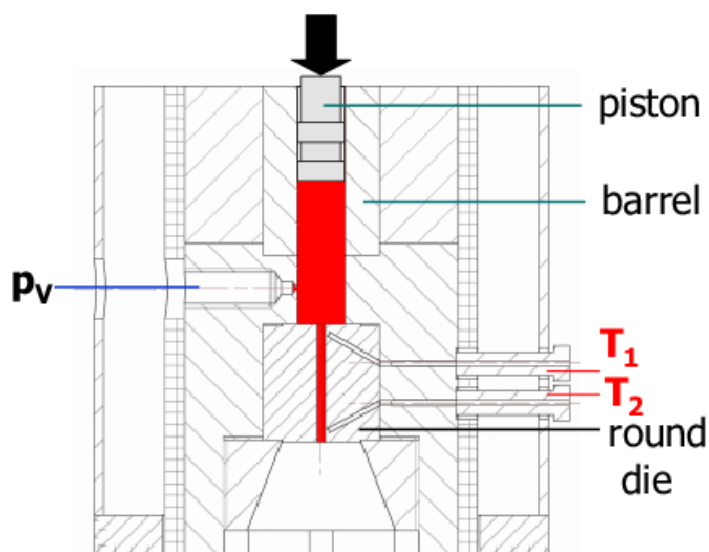


Figure 2.8: Schematic diagrams of high pressure capillary rheometer [35]

As shown in figure 2.8, the polymer material is placed in a cylinder, heated to the melting temperature, and then a piston is used to impart a certain pressure to the material to pass through the capillary. A pressure sensor is placed near the capillary, the pressure during the flow of the material through the capillary can be obtained and the steel temperature of the capillary is measured by the thermocouples in the capillary.

The volumetric flow rate \dot{V} is calculated by the piston velocity v_p according the following equation:

$$\dot{V} = \pi \cdot R_p^2 \cdot v_p \quad (2.12)$$

Where R_p is the radius of the cylinder/piston.

For Newtonian fluids, the shear rate at the capillary wall is

$$\dot{\gamma} = \frac{4\dot{V}}{\pi R^3} = \frac{1}{\eta} \tau_R \quad (2.13)$$

Where R is the capillary radius.

The wall shear stress τ_w is calculated by the measured pressure p , Bagley ends correction p_E [23] and the length over diameter ratio L/D .

$$\tau_w = \frac{p - p_E}{4 \cdot (L/D)} \quad (2.14)$$

For non-Newtonian fluids, since the viscosity is not constant, using Weissenberg-Rabinowitsch correction equation [36] is necessary to calculate the true wall shear rate $\dot{\gamma}_w$. The equation is:

$$\dot{\gamma}_w = \frac{3}{4} \dot{\gamma}_s + \frac{1}{4} \tau_R \frac{d\dot{\gamma}_s}{d\tau_R} \quad (2.15)$$

$$\dot{\gamma}_w = \frac{\dot{\gamma}_s}{4} \left(3 + \frac{\tau_R}{\dot{\gamma}_s} \frac{d\dot{\gamma}_s}{d\tau_R} \right) = \frac{\dot{\gamma}_s}{4} (3 + S) \quad (2.16)$$

$$S = \frac{\tau_R}{\dot{\gamma}_s} \frac{d(\lg \dot{\gamma}_s)}{d(\lg \tau_R)} \quad (2.17)$$

Where $\dot{\gamma}_s$ is apparently shear rate, S is the slope of the curve. Finally, the true viscosity η_w is obtained by the following equation.

$$\eta_w = \frac{\tau_w}{\dot{\gamma}_w} \quad (2.18)$$

2.3.2 Rotational rheometer

The rotational rheometer is used to research rheology at low shear rates. The main core components of the rotating rheometer are an optical encoder, a torque sensing device, an engine and a tool that can apply external forces; its greatest advantage is the air bearing of the rheometer, which enables the torque sensing device and the engine to float to minimize friction. A rotational rheometer has two modes of operation: Continuous rotation and oscillation. The small-angle oscillation measurement plays an important role in the polymer processing technology, so that the oscillation at a narrow angle is most often used for polymers. This oscillation measurement can provide important viscoelastic information for polymer material processing, such as a correlation to molecular weight, molecular weight distribution and melt viscosity, etc. There are three different geometries: cone-plate, plate-plate and concentric cylinder. In this thesis, the parallel plates geometry was used, shown in Figure 2.9.

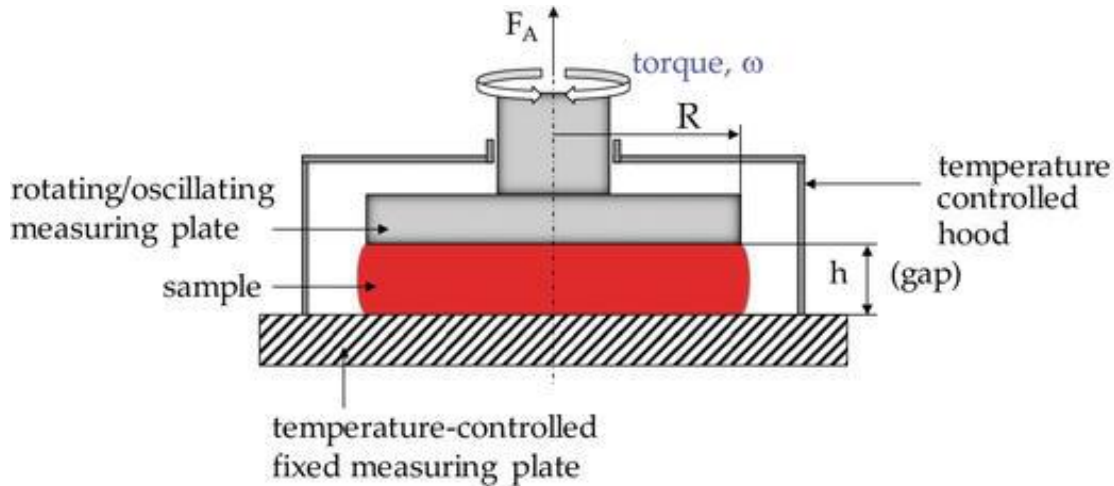


Figure 2.9: Schematic diagrams of parallel plates rotational rheometer [37]

The advantage of parallel plates is that the measuring gap can be adjusted [37]. It can test high viscosity samples (including polymer melts, non-crosslinked silicon), dispersions with larger particles and soft solids such as cheese and elastomers. And the plate-plate geometry is easy to clean. Because the shear rate is dependent on the specific radius r of the plates, the shear rate at the edge of the plate is higher than at the center of the plate, leading to no constant shear conditions in the gap. At the edge of the plate, effects such as sample migration out of the gap or drying of the sample (skin formation) might occur. Large gap width might result in non-uniform sample temperature if the temperature is controlled from one side only or if the temperature-equilibration time is too short.

When the plate is oscillated by the motor, the torque M and the angular velocity ω are measured by the sensor. Then the shear rate $\dot{\gamma}$ and the shear stress τ can be obtained.

$$\dot{\gamma} = \frac{R}{h} \cdot \omega \quad (2.19)$$

$$\tau = M \cdot \frac{2}{\pi \cdot R^3} \quad (2.20)$$

Where R is outer plate radius, h is gap size between plates.

For fluids that show a non-Newtonian flow behavior, the shear stress must be corrected by the Weissenberg-Rabinowitsch correction.

$$\tau = M \cdot \frac{2}{\pi \cdot R^3} \cdot \left(\frac{3+n}{4}\right) \quad (2.21)$$

Where n is power-law-exponent.

2.3.3 Pressure-specific volume-temperature (pvT) relationship

Polymer processing technology subjects the material to different temperatures T (mainly heating and then cooling), large fluctuations in pressure p (maybe more than 2000 bar), and a phase change from solid to molten and then back to solid during processing [38].

The pvT relation is an abbreviation for the relationship between the acting pressure (p), the specific volume (v) and the ambient temperature (T) in the equilibrium state of matter. Quantitative research on the pvT relationship of various substances, especially fluids

(collectively called gases and liquids). Its purpose is to use the p-v-T data to calculate the mass and volume of the fluid with known temperature and pressure and then to calculate the flow rate of the fluid, the geometric dimensions of the runner, and the reactor. The p-v-T relationship is sufficient to characterize polymers and is usually plotted in the p-v-T diagram in which the specific volume is mainly plotted against the temperature and the pressure is used as a parameter.

The crystalline polymer and the amorphous polymer have distinct physical properties. The crystalline polymer has a distinct melting point, and the molecules are regularly arranged in a solid state. The strength is strong, and the tensile force is also strong. During the melting, the specific volume changes greatly and the shrinkage is higher than after solidification. The internal stress is not easily released, and the finished product is opaque. The heat dissipation during forming is slow. The shrinkage after cold mold production is large, while the shrinkage after hot mold production is small.

Compared with crystalline plastics, there is another non-crystalline polymer, which has no obvious melting point. The molecules are irregularly arranged in a solid state, and the specific volume changes little during melting. It is not easy to shrink after solidification, and the transparency of the finished product is good. The higher the color, the faster is the heat dissipation during forming. It can be seen that these two types of materials have different physical properties, so the curves obtained from the measurements of the two types of polymers are significantly different [38], as shown in Figure 2.10 and Figure 2.11.

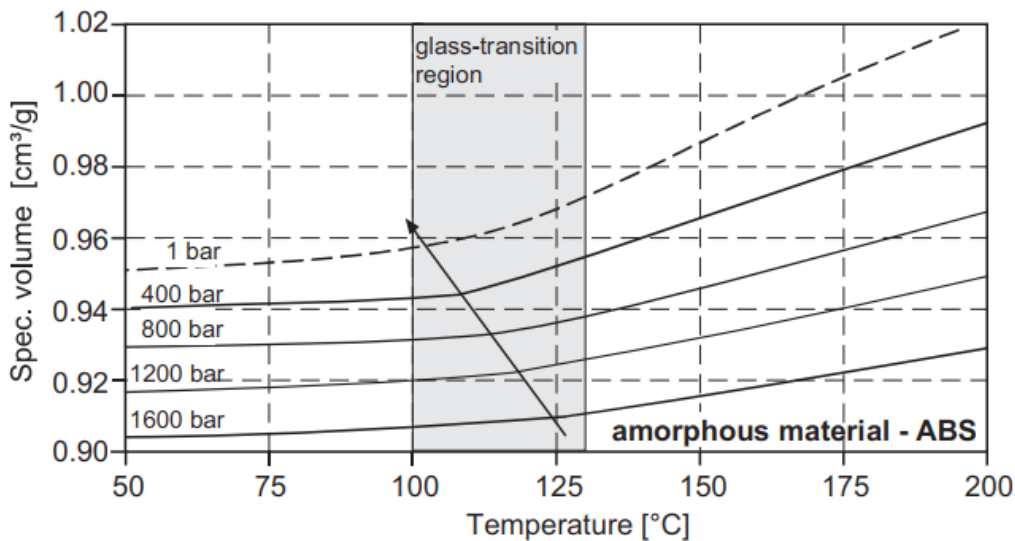


Figure 2.10: p-v-T measurement of an amorphous ABS as a function of temperature and pressure, isobaric cooling [38]

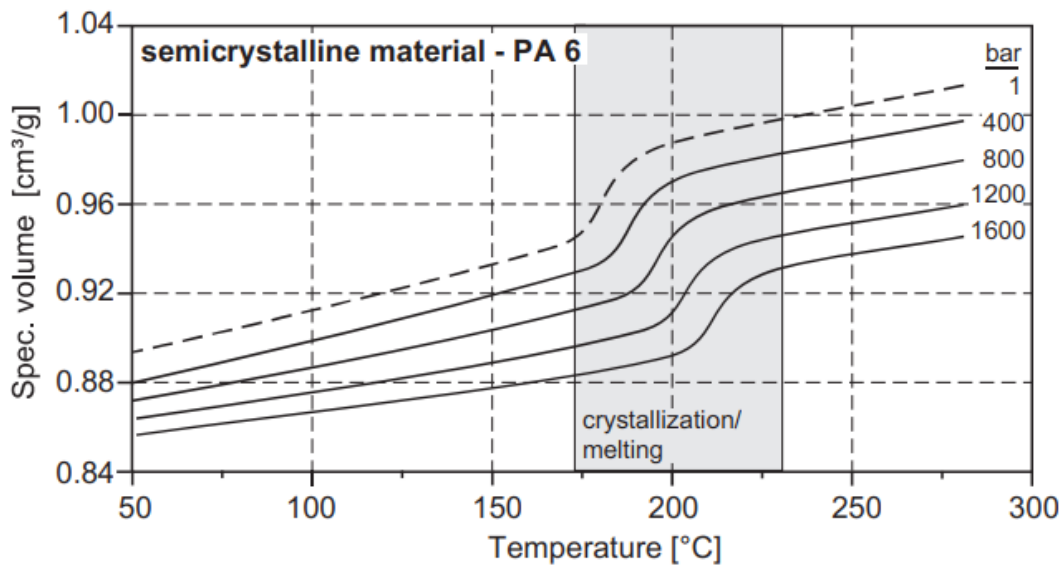


Figure 2.11: pVT measurement of a semicrystalline PA 6 as a function of temperature and pressure, isobaric cooling [38]

The direct pressurization measuring equipment is mainly composed of a sample chamber, a pressurized power system, a heating and cooling system, sensors, and a data acquisition control system. The instrument setting is shown in the Figure 2.12.

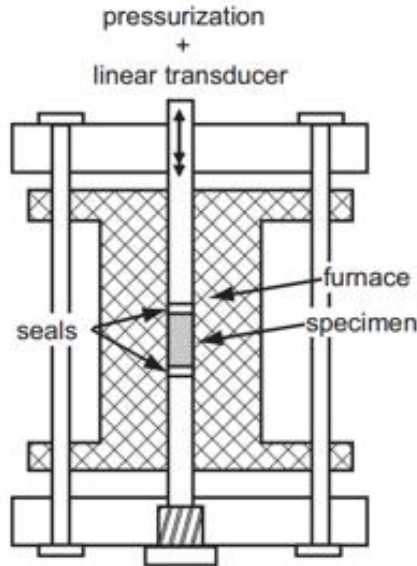


Figure 2.12: Schematic diagrams of direct method pVT measurement [38]

During the test, the polymer sample is placed into the heatable cylinder which the bottom was well sealed. After the sample is melted by heat, the melt containing the bubble is removed by the piston, and then the test sample is sealed. The sample is directly processed by the piston. During pressurization the corresponding temperature and pressure values are directly measured through a temperature and pressure sensor connected to the computer. Because the cross-sectional area of the barrel is constant, the volume of the sample can be calculated

indirectly by the computer based on changes in the position of the piston. Then the change of the specific volume is calculated as following equation (2.22):

$$\Delta v(p, T) = \frac{\Delta l(p, T) \cdot \pi \cdot r^2}{m} \quad (2.22)$$

Where m is the weight of simple, p is the pressure, T is the temperature, r is the radius of the cavity, Δl is the change of the piston position.

The density ρ of the material at melt temperature is calculated by the Schmidt equation(2.24) [39]:

$$\frac{1}{\rho(T, p)} = v(T, p) = \frac{K_1}{p + K_4} + \frac{K_2}{p + K_3} \cdot T \quad (2.23)$$

Where K_1 - K_4 are fitting coefficients

2.3.4 Differential scanning calorimetry (DSC)

DSC is a thermal analysis technique that uses a compensator to measure the relationship between the heating rate and temperature required to bring the sample and the reference to the same temperature. It is widely used in various fields such as plastics, rubber, fibers, metal materials and composite materials. It can study the melting and crystallization process of materials, glass transition, phase transition, liquid crystal transition, solidification, oxidation stability, reaction temperature and reaction enthalpy [40]. The schematic structure is shown in Figure 2.13.

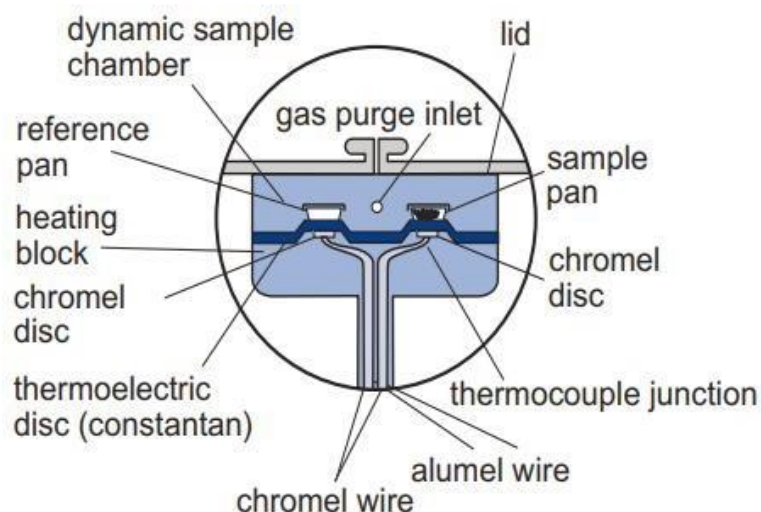


Figure 2.13: Structure of a DSC measuring cell (heat-flow principle) disk tester system [40]

The sample pan is loaded with a sample and placed on the thermoelectric disc together with a reference pan (usually empty). Given thermal symmetry of the arrangement in a uniform oven according to a certain temperature program (linear heating, cooling, constant temperature, and combinations) and a pair of thermocouples (reference thermocouple, sample thermocouple) was used to continuously measure the temperature difference between the pans. If the specific heat capacity of the sample changes when temperature changes, there

will be a temperature difference, which is theoretically proportional to the specific heat capacity [40] and the time/ temperature (heat flow) is continuously mapped to obtain a DSC curve.

The Figure 2.14 shows an example of a DSC profile. The sample, reference sample (sample with known specific heat capacity), and empty pot are measured under the same conditions. Then calculate the specific heat capacity of the sample by the following equation (2.24) [41]:

$$C_{PS} = \frac{H}{h} \cdot \frac{m_r}{m_s} \cdot C_{pr} \quad (2.24)$$

Where C_{ps} is C_p of the sample, C_{pr} is C_p of the reference, m_s is the weight of sample, m_r is the weight of the reference, H is the difference of sample and empty pan, h is the difference of reference and empty pan.

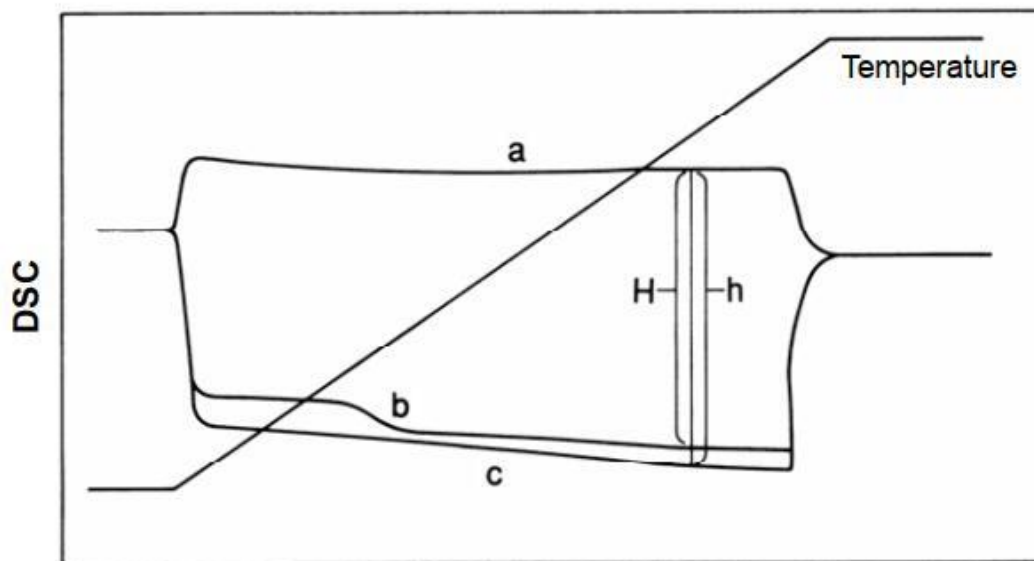


Figure 2.14: DSC measurement of specific heat capacity, a) empty pan, b) sample, c) reference [41]

2.3.5 Transient line source (TLS)

The transient line source method is an ideal and standardized method for measurement of the thermal conductivity [42]. The thermocouple and the line source heating element are sheathed in a needle-shaped measuring element. The schematic structure is shown in Figure 2.15.

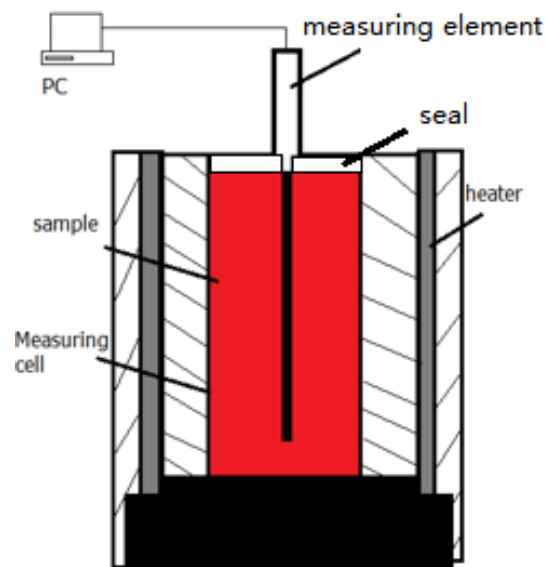


Figure 2.15: Schematic diagrams of transient line source method [39]

First, the material is filled and sealed by the measuring element with a seal. Second, the material is heated to a certain temperature. When the sample is at temperature equilibrium, a stepwise heat flux per unit length is applied by the heating element in the needle, and the temperature increase is recorded. Then the relationship between temperature and time is obtained. Finally, The thermal conductivity λ can be calculated by the following equation(2.25) [42].

$$\lambda = \frac{K \cdot q \cdot \ln\left(\frac{t_2}{t_1}\right)}{4 \cdot \pi \cdot (T_2 - T_1)} \quad (2.25)$$

Where q is the the heat flow per unit length and K is the sensor calibration factor.

The advantages of TLS are easy to use, fast thermal conductivity measurements and direct results without additional calculations.

For the polymer compound system, since there are no free electrons inside, the heat conduction is mainly through the vibration of the ordered lattice and disordered chain segments.

2.3.6 Modified high pressure capillary rheometer

To measure the viscosity under high pressure, the high pressure capillary rheometer is modified by adding a downstream chamber. The chamber is equipped with an adjustable cone valve to generate and change the back pressure for the melt flowing through the capillary die. Two pressure sensors are installed: The first pressure sensor is upstream of the die, and the second pressure sensor is downstream of the die. The pressure chamber is maintained at the desired temperature by a band heater, which is controlled by an independent thermostat [43]. The setup diagram is shown in Figure 2.16.

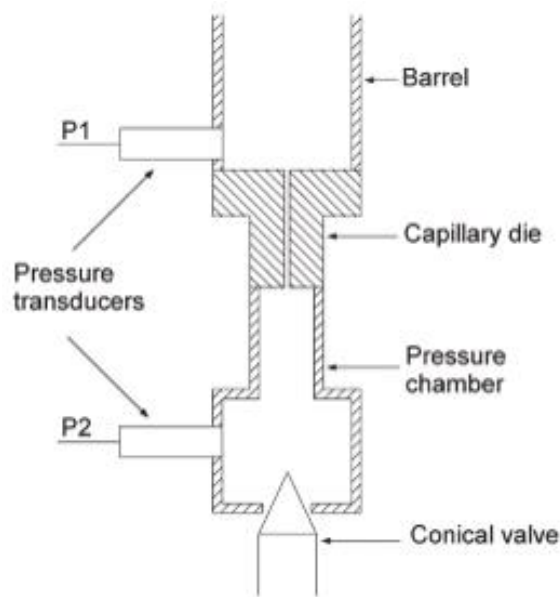


Figure 2.16: Schematic of the modified HPCR experimental set-up [43]

The total pressure drops across the capillary Δp and the mean pressure in the capillary p_m can be calculated by the following equations (2.26) and (2.27):

$$\Delta p = p_1 - p_2 \quad (2.26)$$

$$p_m = \frac{(p_1 + p_2)}{2} \quad (2.27)$$

Where p_1 and p_2 are the recorded upstream and downstream pressures.

The true entrance pressure drop Δp_E was calculated by means of Bagley correction. The true wall shear rate $\dot{\gamma}_w$ was calculated by means of Weißenberg-Rabinowitsch correction:

$$\dot{\gamma}_a = \frac{32 \cdot Q}{\pi \cdot D^3} \quad (2.28)$$

$$\tau_w = \frac{\Delta p - \Delta p_E}{4 \cdot (L/D)} \quad (2.29)$$

$$\dot{\gamma}_w = \frac{\dot{\gamma}_a \cdot \left[3 + \frac{d \log(\dot{\gamma}_a)}{d \log(\tau_w)} \right]}{4} \quad (2.30)$$

Where $\dot{\gamma}_a$ is the apparent shear rate, Q is the flow rate, D is the capillary diameter, L is the capillary length, τ_w is the true shear stress at the die wall.

The true viscosity η_w for a given true wall shear rate $\dot{\gamma}_w$ can now be written as

$$\eta_w = \frac{\Delta p - \Delta p_E}{4 \cdot \dot{\gamma}_w \cdot (L/D)} \quad (2.31)$$

The relationship between viscosity and pressure can be approximated as given in [36]

$$\eta_p = \eta_{p_0} e^{\beta(p_m - p_0)} \quad (2.32)$$

Where η_p and η_{p_0} are the melt viscosities of the polymers at pressures p_m and p_0 , and β is the temperature-dependent pressure coefficient of the shear viscosity. Studies have shown that for the same polymer melt, the effects of pressure increase and temperature reduction on viscosity are equivalent.

For the pressure coefficient β , there are the following forms [43]:

$$\beta_0 \equiv \left(\frac{\partial \ln \eta_0}{\partial p} \right)_T \quad (2.33)$$

$$\beta' \equiv \left(\frac{\partial \ln \eta}{\partial p} \right)_{\dot{\gamma}, T} \quad (2.34)$$

$$\beta'' \equiv \left(\frac{\partial \ln \eta}{\partial p} \right)_{\tau, T} \quad (2.35)$$

Form 2.33 is β for zero-shear-rate viscosity, form 2.34 is β at constant shear rate, and form 2.35 is β at constant shear stress.

2.4 Computer simulation

For a long time, manufacturers of polymer material products have relied on the experience and skills of skilled engineers to improve the production process and to optimize the process during the running production. Due to the viscoelastic properties and temperature and pressure dependence of polymer materials, long development time and debugging costs are often required to achieve a stable production of qualified products, which greatly restricts the development efficiency and competitiveness of new products of enterprises.

With the rapid development of high-speed supercomputers, computer simulation technology plays an important role in industrial production. In recent 30 years, due to a large number of applications of polymer materials and composite materials as well as a new academic field (such as biodynamics/ biomechanics), most of them are viscoelastic materials, which make people interest in rheology theory. Since the 21st-century computational fluid dynamics (CFD) technology continues to progress and is widely used in industrial production, making the flow of complex fluids become an important research field. Using numerical simulation technology replaces manual testing, which can shorten the product design cycle, optimize process conditions, reduce raw material waste, and thus reduce production costs.

Computer simulation technology usually uses the finite element method (FEM), finite difference method (FDM), finite volume method (FVM), boundary element method (BEM), and other numerical calculation methods to simulate the flow, the packing of plastic materials in the cavity and the cooling process for predicting the warpage and deformation of the molded product and analyzing the influence of materials, process parameters and mold structure on product quality. This approach allows to optimize the product and mold structure as well as the molding process parameters. Furthermore, all of this is based on a large and accurate material database.

De, Kuipers and Peters [44] investigated the creeping flow of a viscoelastic fluid through a three-dimensional random porous medium using computational fluid dynamics. The simulations reveal a transition of flow structure from a laminar Newtonian regime to a nonstationary non-Newtonian regime with increasing viscoelasticity. Makke et al. [45] analyzed the influence of tie and loop molecules on the mechanical properties of lamellar block copolymers. Based on a coarse-grained model two kinds of alternating layered structure polymer systems with different glass transition temperatures were constructed. The different chain structures play a role in the mechanical response of the system. The results show that the bridge chain and the ring chain play a leading role in stress transmission. The reduction of the bridge chain will reduce the entanglement density of the system and affect the stress yield and strain hardening behavior of the system.

2.4.1 Introduction to SIGMASOFT® VIRTUAL MOLDING

SIGMASOFT® VIRTUAL MOLDING [46] software is a molding analysis software under SIGMA engineering GmbH, which can optimize plastics parts and injection molds as well as production conditions of thermoplastic-, elastomer-, thermoset- or MIM/CIM applications. The software is divided into CAD interface and meshing, flow analysis, thermal analysis, shrinkage and warpage analysis, ejection simulation, and post molding analysis.

(1) CAD interface and meshing

Sigmasoft® starts with some sort of CAD model. User imports the entire mold base with part and runner geometries, as well as some related auxiliary functions to help engineers for completing their work more conveniently. It can easily read 3D models in S80, STEP, STL, and other formats, as well as original 3D models of CAD software such as UG, Pro/E, I-DEAS, CATIA, Solidworks, etc., and can be checked and copied directly in the software and can simplify and adjust the solid model. Sigmasoft® adopts physical 3D finite volume models with an automatic mesh process. No mesh rework need to reduce resource waste of repeated mesh repairs so that the users have more time to design molds and solve actual process problems.

(2) Flow analysis

In this part, the software analyzes filling and packing of injection molding. It is using advanced rheology models so that the software has the ability to consider crystallization, melt history analysis and looking at marks of voids, venting and other defects.

(3) thermal analysis

In this part, the software analyzes how the polymer cools over time. The software allows users to customize the cooling scale and also for multiple cycles. It considers contour cooling, mold heat balance, heat transfer between all mold components, and coupled 3D simulation by using CFD simulation for calculating the flow of the cooling fluid and its heat exchange with the mold.

(4) Shrinkage and warpage analysis

The software shows the final part of shrinkage and warpage and how the part looks like once it is ejected from the machine. It is calculated during and after the cycle and including the warpage of inserts. The stress prediction for all mold components and parts is considered when it is actually in its application. The software can calculate a single or multi-shot molding process.

(5) Ejection simulation

Sigmasoft® has the ability to simulate the actual ejection portion of the phase to see if the rejection design is impacting the part in any negative way. The part deformation due to ejection forces, ejector pin contact pressure, stress, and strain are calculated by the dynamic simulation.

(6) Post molding analysis

The post molding analysis is to calculate further cooling, crystallization, stress relaxation after the part is ejected out of the mold. The displacement and stresses are calculated to ambient temperature. It is also an option to add a secondary heating or cooling cycle to nail or quench the part after ejection and simulating the impact stresses in the final part.

Compared with the existing simulation analysis software, Sigmasoft® has additional technical advantages, specifically covering the following aspects:

1) MIM technology and its simulation: At present, only Sigmasoft® on the market has related MIM flow equations and MIM phase separation analysis technology. And it has its own MIM material database based on BASF, Alliance, Taurus, IFAM, and other manufacturers. With the support of MIM/CIM modules, it is possible to perform numerical and result simulations on MIM/PIM/CIM related products.

2) Mold analysis: Compared with other commercial injection molding simulation software, mold exhaust analysis, multiple cycle analysis, overall mold analysis, mold ejection analysis, secondary heat treatment analysis, heat and cooling cycle analysis, fluid-solid coupling analysis can be performed on the mold.

3) Support for new technologies: In addition to the exclusive MIM/CIM simulation analysis, Sigmasoft® also supports multi-component injection molding simulation analysis and hot runner simulation analysis to meet the needs of users for new process technology simulation.

4) Integration of multiple resources: Besides, the Sigmasoft® team can also integrate structural design, flow field design, electric field design, and magnetic field design providing a wider use environment.

2.5 Current status of research on pressure dependent rheology

The pressure-dependent rheology of materials has been studied since 1891. Barus [47] had put forward the Barus law in the study of marine glue: The viscosity increased exponentially with the increase of pressure. The rheological research on pressure dependence of viscosity of polymers was first conducted in 1957. Maxwell [48] studied the apparent viscosity of high-molecular-weight polyethylene (PE) and polystyrene (PS) under the influence of hydrostatic pressure and found that the apparent viscosity of polyethylene increased by 14 times when increasing from atmospheric pressure to 168 MPa, PS increased by 135 times when the pressure increased to 126 MPa. In 1968, Choi [49] studied polystyrene with hydrostatic pressure in an extrusion rheometer and found that at 195°C and the shear rate at 7.12 s^{-1} , when the pressure increased from 0 to 170 MPa, the viscosity increased nearly 4 times, but this research method was limited to low shear rates ($<10 \text{ s}^{-1}$). Then in 1971 Penwell and Porter [50] first studied the nonlinear pressure drop of low molecular weight polystyrene at 140 and 160°C versus different capillaries. Cogswell and McGowan [51] studied both effects of pressure and temperature on the viscosities of polymeric liquids. They found that for the apparent viscosity of polymer melts an increase in pressure is equivalent to a decrease in temperature. In 1974, Christmann and Knappe [52] realized the test in low-density polyethylene (LDPE) and poly(methyl methacrylate) (PMMA) by using the master curve, describing the effects of

pressure and temperature. They found that the effect of pressure can be described by exponential relation, and the effect of temperature can be described by Arrhenius expression. Later, in 1983, Laun [53] successfully used flush mounted pressure transducers to directly measure the pressure loss of high molecular weight LDPE melt in the slit-die rheometer. By analyzing the non-linear pressure profile, in the case of ignoring the compressibility of the melt and heat conduction inside the melt, they calculated the pressure coefficient β . In 1990, Driscoll and Bogue [54] added an additional downstream chamber to the capillary rheometer to increase the average pressure in the capillary die. This chamber can control the internal pressure through a valve, and through analysis of nonlinearities in Bagley plots, they successfully measured the melt viscosity of polystyrene at 124 MPa. Kadijk and Van Den Brule [55] measured PS, polyacrylonitrile-butadiene-styrene (ABS) and polypropylene (PP). They found that for PS and ABS, the pressure coefficient is not affected by pressure, but the pressure coefficient of PP decreased when pressure increased. Friesenbichler et al. [2] developed an easy-to-handle rheological measurement system which was like a standard injection mold with interchangeable dies. The system enables operators to measure viscosity at practically relevant shear rates from 100S^{-1} to $2 \cdot 10^6\text{S}^{-1}$.

With the development of computer injection simulation technology in recent years, the rheological properties of materials under high pressure conditions have attracted more and more attention. Pantani and Sorrentino [56] used atactic (aPS) and syndiotactic (sPS) Polystyrene and found that the pressure coefficient of sPS was slightly higher than aPS and guessed that it might be due to differences in free volumes. Sedlacek [57] measured the pressure coefficients of several common polymers such as high-density polyethylene (HDPE), linear low-density polyethylene (LLDPE), LDPE, PP, PS, PMMA through a second chamber of rheometer with restricting needle valve. They found that the temperature-sensitive materials are the same time are pressure-sensitive materials, and except for PS and PP, the pressure coefficient does not depend on temperature and pressure. Merabia and Long [58] researched on the comparison of 1,1'-di(4-methoxy-5-methylphenyl)-cyclohexane (BMPC), 1,1'-bis(p-methoxyphenyl)cyclohexane (BMMPC) two non-polar materials and polyvinyl acetate (PVAc) a weakly polar material, and found that for non-polar materials density fluctuations play a greater role than the average density on temperature and pressure dependence. Son [59] measured the pressure coefficient of PS at 180°C by improving the double piston rheometer with a slit die using only 3g sample. Aho [43] used a capillary rheometer equipped with a pressurizable downstream chamber and got the pressure shift factor through data fitted as master curves, and calculated the pressure coefficient of ABS, polycarbonate (PC), PS, PP, LDPE. Sorrentino and Pantani [60] found in their study that for aPS and sPS, as the temperature increases, the pressure coefficient decreases. Only very few investigations on polar polymer melts are published. Piyamanocha, Sedlacek, and Saha [61] used a standard capillary rheometer with a back-pressure device to study 3 various poly(lactic)acid (PLA) and found that the molecular structure notably affects the values of the pressure coefficient. Li et al. [62] used a capillary rheometer with an attached counter pressure chamber to study the pressure coefficient of Polyamide 6 (PA6), PP, LDPE and PET. They found that PA 6 had the lowest pressure dependence. Ceccia [63] studied the temperature and pressure coefficients of PA66, a strongly polar material, and found that it was significantly different from non-polar materials or weakly polar materials. The pressure coefficient was unchanged below 300°C , and increased when temperature increased over 300°C . Friesenbichler, Neunhäuserer, and Duretek [64] used processing machines with slit-die systems to characterize rheological complicated polymeric materials under process-relevant conditions with viscosity values fully temperature corrected.

In recent years, some scholars have begun to use CAE simulation to verify results. Stieger et al. [65] used high pressure capillary rheology to study the rheological behavior of a carbon

black filled hydrogenated acrylonitrile–butadiene rubber (HNBR) and simulated the rheometer flow in CFD software. They found that the simulation results provided only a valid workaround solution for the short die. Friesenbichler and Neunhäuserer [66] researched polypropylene-filled nanocomposite, ABS, PS, isotactic PS and two rubber compound (Styrene-Butadiene Rubber SBR and Nitrile Butadiene Rubber NBR). They compared measured data for the pressure demand in capillary rheometry as well as in injection molding with calculated values based on simulations. They found only the viscoelastic can reproduce the measured pressure drop well. For pressures higher than 100MPa, the pressure dependence of viscosity should be considered. Raha and Sharma [67] used oscillatory and capillary rheometer to determine the pressure dependence of viscosity of three different grades of polycarbonate. Then the validation of the rheological parameters was performed by carrying out injection molding experiments and compared the actual pressure profile by simulation. They found the difference between the simulated (with pressure coefficient) and actual peak pressure was found to be less than 10% and the difference in molecular weight can affect the results.

3 Experimental Details

3.1 Material and Equipment

3.1.1 Material

In this study the ABS copolymer Novodur® HH-106 (hereinafter called ABS) provided by INEOS Styrolution (INEOS Styrolution Group GmbH, Frankfurt am Main, Germany). The density of the material is 1.05 g/cm^3 and the melt volume flow rate (MVR) is $7 \text{ cm}^3/10\text{min}$ [68]. The fiber reinforced semi-crystalline polymer PA66 Torzen® G3000HR BK 34 (hereinafter called PA66GF30) provided by Radici group (Radici group, Gandino, Italy). The density of the material is 1.37 g/cm^3 and the shrinkage rate (ISO 1110) is $0.95 - 1.05\%$ [69]. Some of the material properties are given in Table 3.1.

Table 3.1: Material properties of ABS and PA66GF30 [68; 69]

Properties	Unit	ABS	PA66-GF30
Modulus of Elasticity	GPa	2.4	9.8
Elongation at Break	%	8	3.1
Melting temperature	°C	230-270	262

3.1.2 Equipment

The equipment used for the measurements includes rotational rheometer, differential scanning calorimetry, high pressure capillary rheometer, pvT apparatus and thermal conductivity meter. Device types and manufacturers are shown in Table 3.2.

Table 3.2: Experimental instruments and information

Instrument	Device type	Manufacturer
Rotational Rheometer	MCR 501	Anton Paar GmbH, Austria
Differential Scanning Calorimetry	DSC 1	Mettler -Toledo (Schweiz) GmbH, Greifensee, Switzerland
High pressure capillary rheometer	Rheograph 2002	Göttfert Werkstoff-Prüfmachinen GmbH, Buchen, Germany,
pvT apparatus	PVT100	SWO Polymertechnik GmbH, Krefeld, Germany
Thermal conductivity meter	K-System II	Advanced CAE Technology Inc., Ithaca, USA

3.2 Methods

3.2.1 Dryer

Since the materials used in the experiments have different hygroscopy and sensitivity to moisture, e.g. strong hygroscopy of PA66 while ABS shows low hygroscopy, different drying methods were used for the materials shown in Table 3.3 in order to reduce the influence of air bubbles on the experimental results.

Table 3.3: Drying type, temperature and drying time for the used materials

Material	Method	Temperature	Pressure	time
ABS	Blast dryer	80°C	atmosphere	4 hours
PA66	Vacuum dryer	80°C	300 mbar	8 hours

3.2.2 High pressure capillary rheometer

The rheological measurements were carried out using a high pressure capillary rheometer with a maximum force of 20kN enabling pressures up to 1200bar.

In order to analyze the influence of the temperature and shear rate, the measuring conditions of the high pressure capillary rheometer were following a design of experiments (DoE), in which the temperature (T) and shear rate ($\dot{\gamma}$) and length to diameter ratios (L/D) were varied (shown in Table 3.4 and

Table 3.5). The variation of L/D (D=1mm, 180° entry angle) was used to allow the Bagley correction to be performed. All other parameters were kept as constant as possible, and for each parameter set the measurement was repeated three times.

The pre-heating time was set as 2 min. After pre-heating time, the piston was moving at a low constant velocity to get a constant shear rate according to DoE. The pressure was recorded when the pressure was stable. Then the velocity of the piston was changed to the next level and these steps were repeated until the barrel was emptied.

Table 3.4: DoE for the HPCR measurement of ABS

Measuring Condition	L/D (-)	T (°C)	Shear rate (s ⁻¹)
A1	10	230	50-3000
A2	10	250	50-3000
A3	10	270	50-3000
A4	30	230	50-3000
A5	30	250	50-3000
A6	30	270	50-3000

Table 3.5: DOE for HPCR measurement of PA66GF30

Measuring Condition	L/D (-)	T (°C)	Shear rate (s ⁻¹)
B1	10	280	50-3000
B2	10	290	50-3000
B3	10	300	50-3000
B4	30	280	50-3000
B5	30	290	50-3000
B6	30	300	50-3000

3.2.3 Rotational rheometer

The materials were compression molded into samples with a diameter of 25mm and a thickness of approximately 1.5 mm.

To get viscosity at a low shear rate, the rotational rheometer was used. The parallel plate gap was 1 mm and the measured temperatures were the same as listed in Tables 3.4 and 3.5. First, measurements with constant angular frequency (1rad/s) were done to gain information on an acceptable strain level, and the strain range was 0.1-100%. Then the tests with fixed amplitude were performed. ABS was measured at the frequency from 0.1 to 500rad/s, and the strain was set at 5.6%. PA66GF30 was measured at the frequency from 500 to 0.1rad/s, and the strain was set at 2%. Each material was measured three times.

To determine the heat stability of PA66GF30, the frequency was set at 1 rad/s, the strain was set at 2%, and the measuring time was 30 minutes.

3.2.4 pvT relationship

The specific volume dependent on pressure and temperature (pvT relationship) was measured by means of the isobaric cooling mode with a cooling rate of 6K/min, the pressure was set from 200 to 1200 bar with a constant interval of 200 bar. The granules were placed in a cylinder, sealed by the lower and upper piston with sealing material. The weight of the samples was controlled in the range of 0.5-1g. The measured temperature range for PA66GF30 was between 40 and 320°C, and for ABS between 40 and 290°C. The value of the piston displacement was recorded every 2°C. Each material was measured three times.

3.2.5 DSC

The material granules were cut into suitable size with a knife (10mg ± 1mg). Sapphire was used as the reference sample. Next, the sample was laid flat on the bottom of an aluminum crucible and closed by an aluminum cover perforated with needle pricks, which enabled pressure equalization. The measurements were performed in nitrogen atmosphere. The temperature cycle is shown in Figure 3.1. The end temperature of ABS was 300°C, and for PA66GF30 340°C was chosen. The heating/cooling rate was set as 20K/s. Each material was measured two times, and the mean value was used for discussion and simulation.

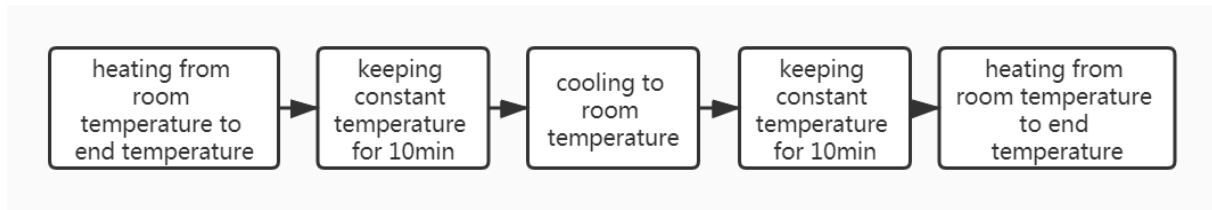


Figure 3.1: Temperature cycle for DSC measurements

3.2.6 Thermal conductivity

The determination of thermal conductivity was performed using the Line-Source method. First, the material was filled and compacted by a piston. Second, the measuring element was inserted into the filled cylinder and TEFLON was used as the sealing material. Then the material was heated to the selected temperature. Two temperatures under glass transition temperature (T_g) or softening temperature (T_s) were chosen and another two were chosen above those. ABS was measured at 35/80/160/250°C, PA66GF30 at 35/95/215/300°C. When arriving thermal equilibrium, the temperature profile was recorded. Finally, the thermal conductivity λ was calculated. Each material was measured two times.

3.2.7 Modified high pressure capillary rheometer

Comparing to the standard high pressure capillary rheometer, to analyze the influence of the pressure on viscosity, the materials were measured in the modified HPCR with a downstream chamber. Theoretically, it is possible to adjust the back pressure valve so that all capillaries and shear rates can be measured at the same average pressure level. However, in practice, this is a very time-consuming process. Therefore, the method by Aho [70] was used. The pressure drops and mean pressure of each material at different pressures were obtained by equation(2.26) and equation(2.27), and entrance pressure drop were obtained by Bagley corrections.

In each round of testing, the valve position was adjusted to make the back-pressure constant. At the beginning of the test, the piston speed was kept at low level. Once the flow reached a steady state, the readings of the two sensors were recorded at the same time. Then I adjusted the piston speed to reach a higher level and continued to adjust the valve position to keep the back pressure consistent with the previous round. After establishing and recording a stable pressure corresponding to the piston speed, the piston speed was increased again, and this process was continued until the barrel was emptied or the limit of any pressure sensor was reached. The back-pressures in this thesis were chosen by 100 and 300 bar according to the maximum pressure of the instrument (1200 bar). All other parameters were kept similar to the standard high pressure capillary rheometer as listed in Tables 3.4 and 3.5. The DoE is shown in Table 3.6 and Table 3.7. For each parameter set the measurement was repeated five times to verify the repeatability of the results.

Table 3.6: DoE for the measurements of ABS using the Modified HPCR

Measuring Condition	Back Pressure (bar)	Measuring Condition	Back Pressure (bar)
A1.1	100	A1.2	300
A2.1	100	A2.2	300
A3.1	100	A3.2	300
A4.1	100	A4.2	300
A5.1	100	A5.2	300
A6.1	100	A6.2	300

Table 3.7: DoE for the measurements of PA66GF30 using the Modified HPCR

Measuring Condition	Back Pressure (bar)	Measuring Condition	Back Pressure (bar)
B1.1	100	B1.2	300
B2.1	100	B2.2	300
B3.1	100	B3.2	300
B4.1	100	B4.2	300
B5.1	100	B5.2	300
B6.1	100	B6.2	300

3.3 Results and discussion

3.3.1 Thermal data

According to the above method, using DSC, the specific heat capacity (c_p) of ABS and PA6GF30 materials was obtained. The heating curve is shown in Figure 3.2. As an amorphous polymer, the c_p of ABS does not change much with temperature. Its curve is like an elongated S shape. PA66GF30 as a semi-crystalline polymer has a peak due to the release of the latent heat of the crystalline part. At the same time, it can be seen from the figure that the glass transition temperature T_g of ABS is about 130°C, and the peak melting point of PA66GF30 is 262°C.

Using K-system II to measure the thermal conductivity (λ) of the material, the results are shown in the Figure 3.3.

It can be seen from Figure 3.3 that as the temperature increases, the thermal conductivity of ABS shows an upward trend. This is due to the high modulus of the material, which easily forms gaps between particles, and the air is a poor conductor of heat. The greater the porosity the lower the conductivity becomes. As the temperature increased the mechanical modulus decreased leading to a decreasing gap size, so the thermal conductivity increases with the temperature increase.

3. Experimental Details

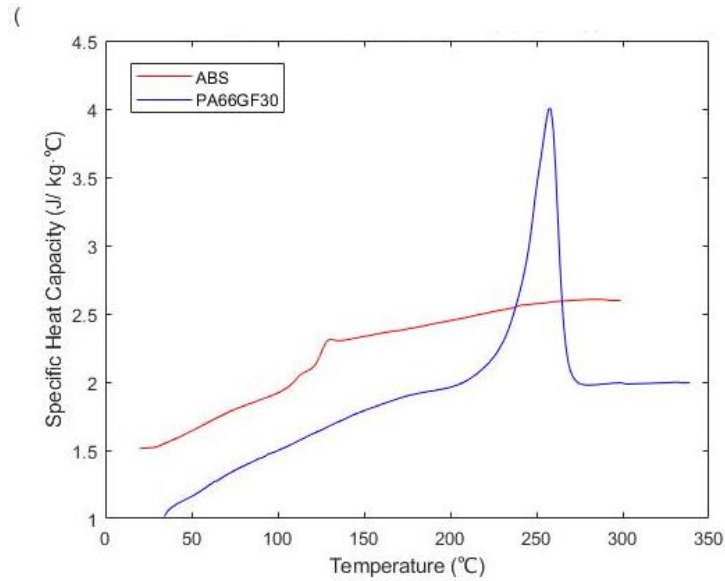


Figure 3.2: Specific heat capacity (c_p) versus Temperature (T) curves of ABS (red) and PA66GF30 (blue)

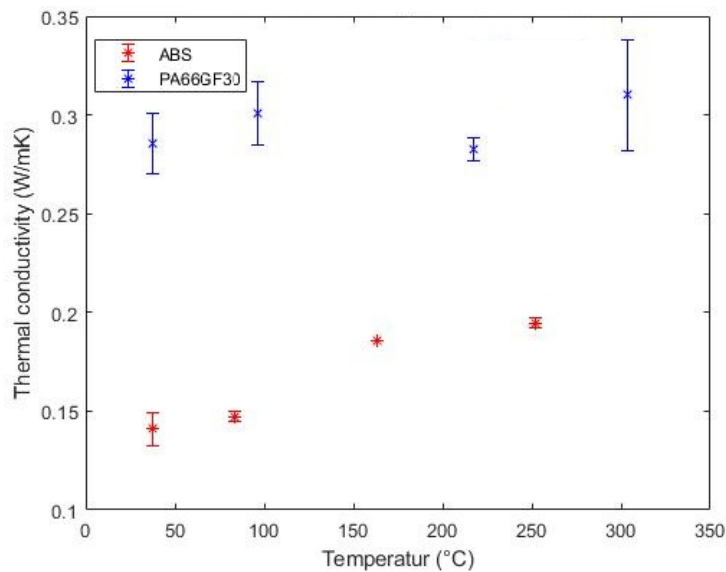


Figure 3.3: Thermal conductivity (λ) at different temperatures of ABS (blue) and PA66GF30 (red)

This also explains that when the temperature was higher than the glass transition temperature T_g , as the material became viscoelastic and the gap was further reduced, the thermal conductivity is greatly improved. As for PA66 as a semi-crystalline material, it has many hydrogen bonds and forms an ordered crystal lattice, so the thermal conductivity is much higher than that of ABS material. At the temperature around melting temperature T_m , when the material's temperature rises, the crystal lattice begins to crack, and the thermal conductivity decreases. As the temperature rises further, the chain segment's mobility increases, and the thermal conductivity increases accordingly.

3.3.2 pVT data

The pVT measurement for the polymer types was performed with the isobaric cooling mode. The measurement results of ABS and PA66GF30 are shown in Figure 3.4 and Figure 3.5.

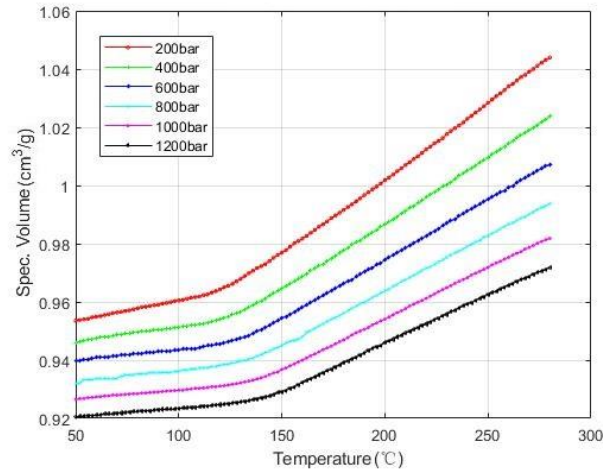


Figure 3.4: Isobaric pVT curves of ABS

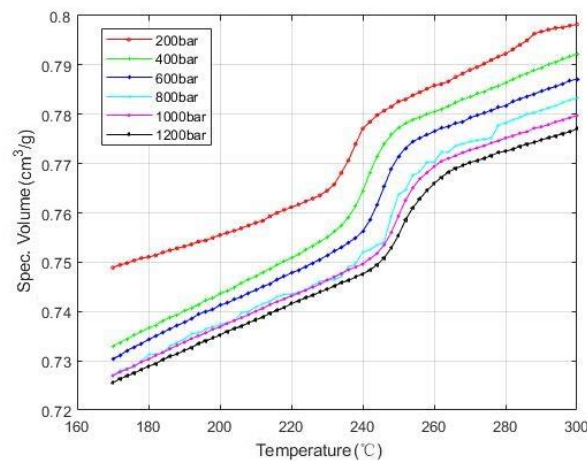


Figure 3.5: Isobaric pVT curves of PA66GF30

The coefficients in the melt range were fitted from the Schmidt model (equation(2.23)) and the results are given in the Table 3.8 and Table 3.9.

Table 3.8: pVT coefficients for ABS in the melting temperature range

K_1	45158	$\text{cm}^3 \text{ bar/g}$
K_2	0.8228	$\text{cm}^3 \text{ bar/g}^\circ\text{C}$
K_3	1426	bar
K_4	49841	bar

3. Experimental Details

Table 3.9: pvT coefficients for PA66GF30 in the melting temperature range

K_1	$1.087 \cdot 10^7$	$\text{cm}^3 \text{ bar/g}$
K_2	0.9997	$\text{cm}^3 \text{ bar/g}^\circ\text{C}$
K_3	3079	bar
K_4	$1.5299 \cdot 10^7$	bar

The experimental data points as well as the predictions of the Schmidt model are shown in Figure 3.6 and Figure 3.7.

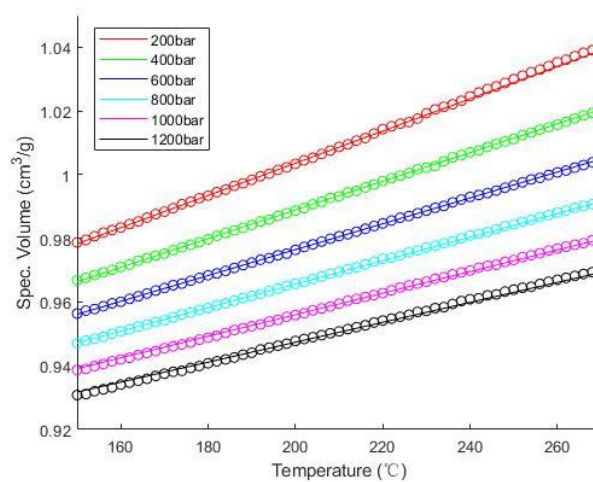


Figure 3.6: pvT curves approximated at melting range by Schmidt equation(2.23) for ABS. The fitting parameter values are given in Table 3.8

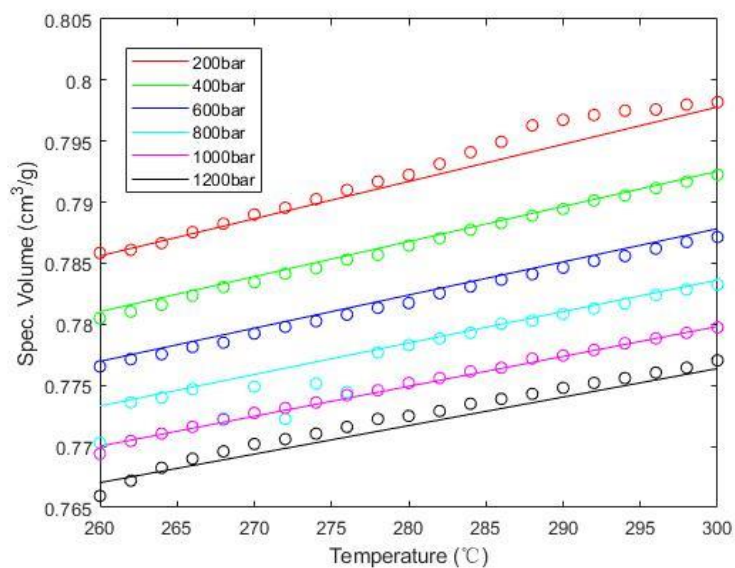


Figure 3.7: pvT curves approximated at melting range by Schmidt equation(2.23) for PA66GF30. The fitting parameter values are given in Table 3.9

According to Jachowicz's research [71], the Schmidt model may turn out to be insufficient with respect to filled polymers. This may be the reason for the deviation.

3.3.3 The effect of residence time on PA66GF30

The results for testing the influence of residence time on shear viscosity for PA66GF30 using the rotational rheometer is shown in Figure 3.8.

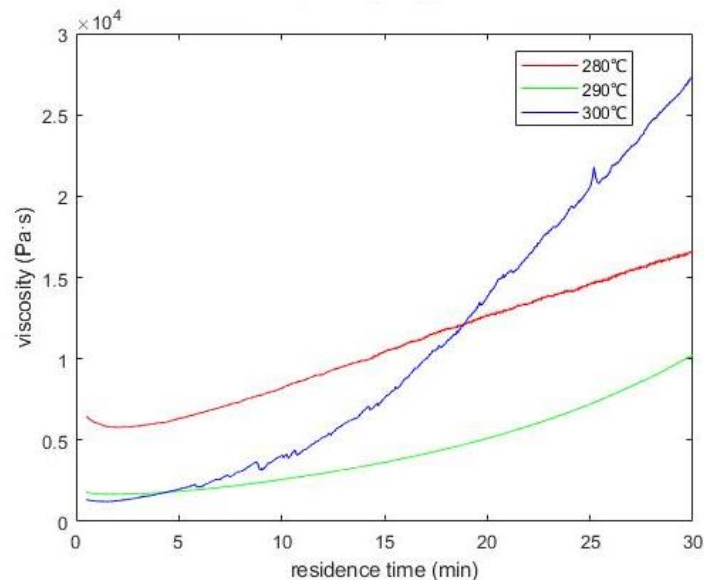


Figure 3.8: Influence of residence time on viscosity for PA66GF30

It can be clearly seen that as the residence time increases, the viscosity of PA66GF30 increases significantly, and as the temperature increases, the viscosity increases faster. According to the research of Yoshizawa [72] and Hill [73], PA66 may be accompanied by a cross-linking reaction in the process of thermal degradation, resulting in a network structure, which greatly increases the viscosity of the material. It shows that the thermal stability of PA66GF30 is extremely poor, and the thermal stability time is about 2.5 min in the temperature range of 280-300°C.

3.3.4 Low shear rate viscosity of ABS and PA66GF30

The low shear rate viscosity of ABS and PA66GF30 was measured using the parallel plates rotational rheometer, and the results are shown in Figure 3.9 and Figure 3.10. When the shear rate was less than 1 s^{-1} , the test time was already greater than 5min. At that time PA66GF30 has begun to degrade and cross-link, so for PA66GF30, only the $5\text{-}500 \text{ s}^{-1}$ shear rate range result is selected.

3. Experimental Details

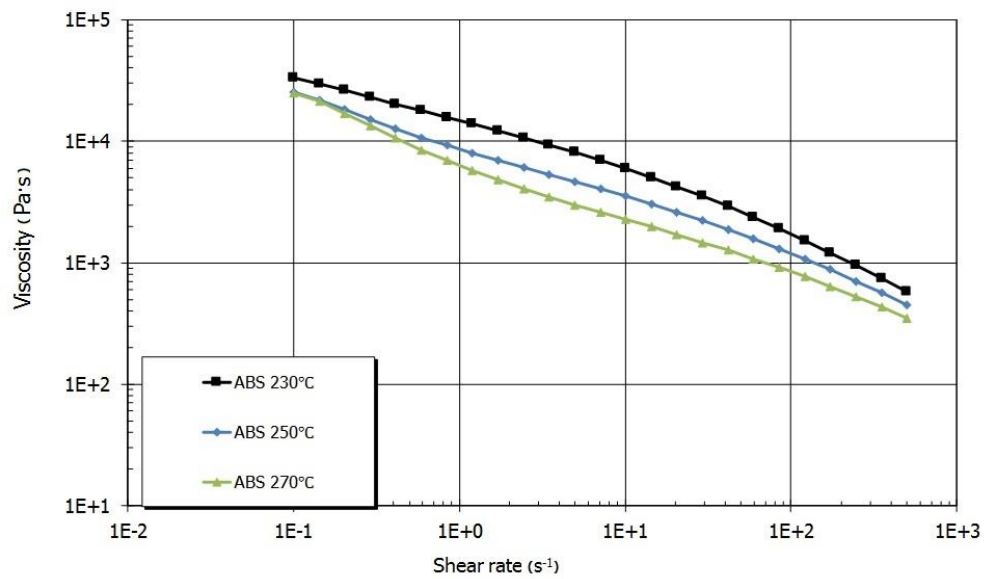


Figure 3.9: Low shear rate viscosity curves of ABS in the range of 0.1 to 500 s⁻¹

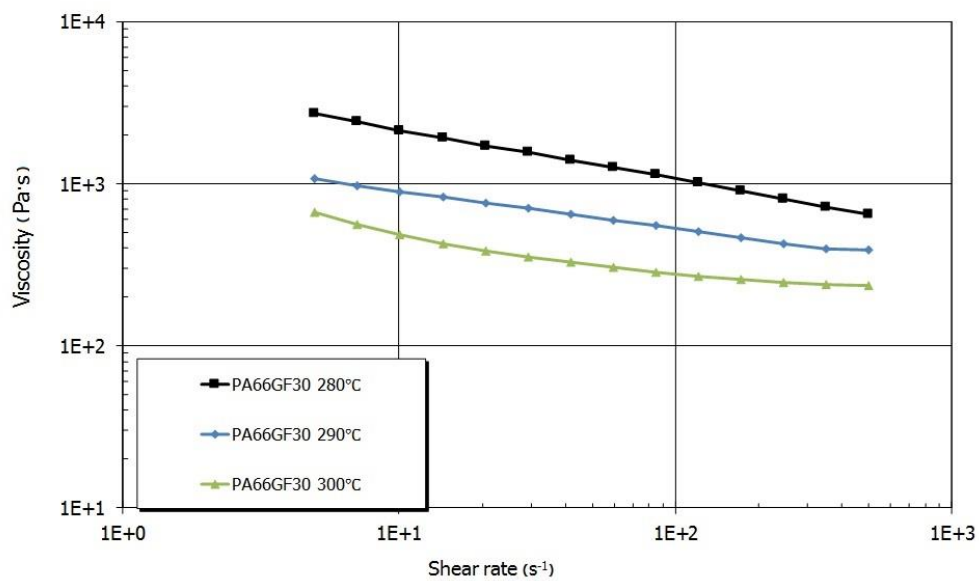


Figure 3.10: Low shear rate viscosity curves of PA66GF30 in the range of 5 to 500 s⁻¹

It clearly shows that for PA66GF30, even using a rotational rheometer, the transition area between quasi-Newtonian flow behavior and the shear thinning region (power-law region) cannot be reached. Therefore, for PA66GF30 the power law expression is used as rheological material law instead of the Carreau-Yasuda model.

3.3.5 High shear rate viscosity of ABS and PA66GF30 materials

According to the above-mentioned capillary rheometer method for measuring and analysis, the viscosity of each material at different temperatures was measured. The results are shown in the following Figure 3.11 and Figure 3.12.

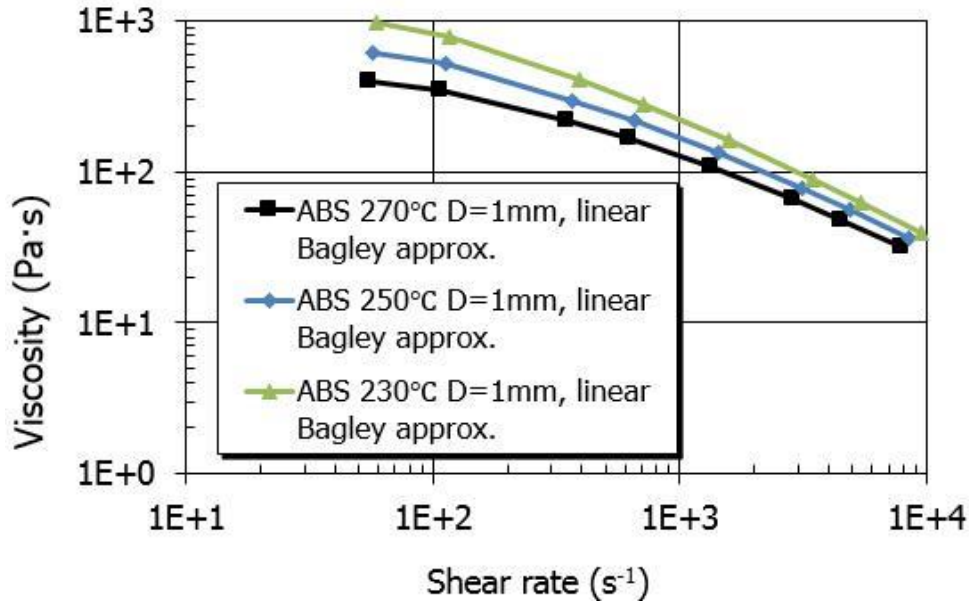


Figure 3.11: High shear rate viscosity curves of ABS at different temperatures

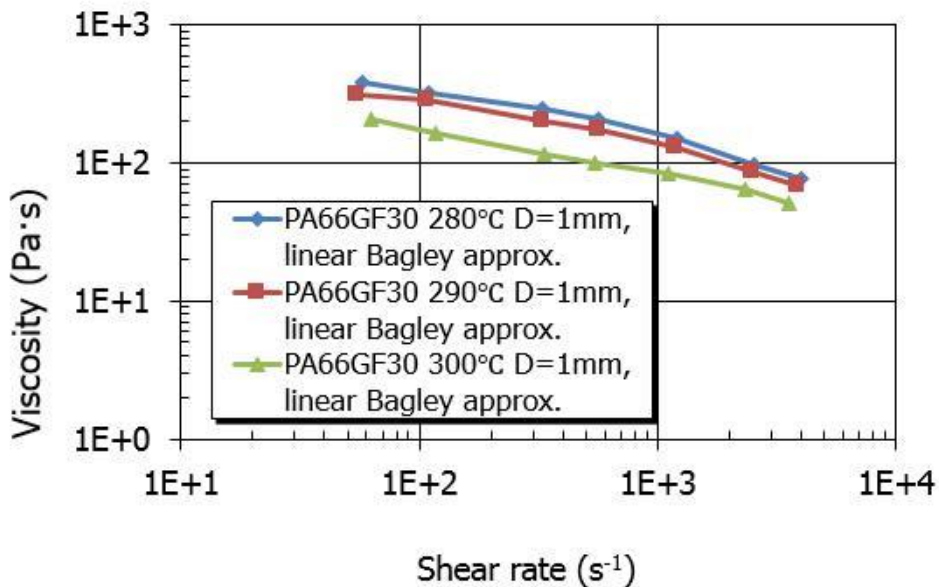


Figure 3.12: High shear rate viscosity curves of PA66GF30 at different temperatures

It can be seen from the figures, at a certain temperature, both ABS and PA66GF30 are pseudoplastic fluids. As the shear rate increases, the shear viscosity decreases. At the same time, it can be seen that ABS is more sensitive to shear rate. When the shear rate was increased from 50 S⁻¹ to 5000 S⁻¹ at 230°C, the shear viscosity decreased from 988 Pa·s to 61 Pa·s. As the PA66GF30 material containing glass fiber as a filling material, the polymer chain easily entangled, so the shear viscosity of the material decreased to a relatively small extent

3. Experimental Details

with the increase of the shear rate. At 280°C, when the shear rate increased from 50 S⁻¹ to 5000 S⁻¹, the shear viscosity decreased from 380Pa·s to 77Pa·s.

The experimental data of ABS and PA66GF30 were fitted to Modified Carreau viscosity model equation (2.7) and power law expression model equation (2.3). The best-fit parameter values are summarized in Table 3.10.

Table 3.10: Best-fit parameters of equation (2.3) and (2.7)

	ABS/ 230°C	ABS/ 250°C	ABS/ 270°C	PA66GF30/ 280°C	PA66GF30/ 290°C	PA66GF30/ 300°C
η_0 in Pas	1296	688	442	-	-	-
n in (/)	0.2708	0.3793	0.3837	0.5617	0.5685	0.6713
α in (/)	1.2364	1.8263	1.3781	-	-	-
λ in (s)	0.011009	0.009846	0.007245	-	-	-
K in (Pa.s ⁿ)	-	-	-	3176.34	2328.14	799

3.3.6 The influence of pressure on the shear viscosity of ABS and PA66GF30

The modified high-pressure capillary rheometer was used to measure the two materials under different back pressures. The results compared with 1 bar are shown in the following Figure 3.13 and Figure 3.14.

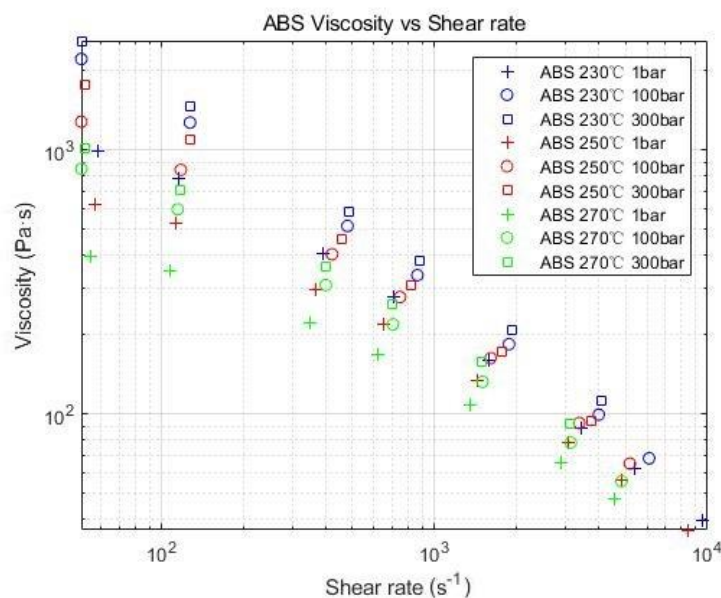


Figure 3.13: Viscosity versus shear rate for ABS with 1bar/100bar/300bar back pressure at different temperatures

3. Experimental Details

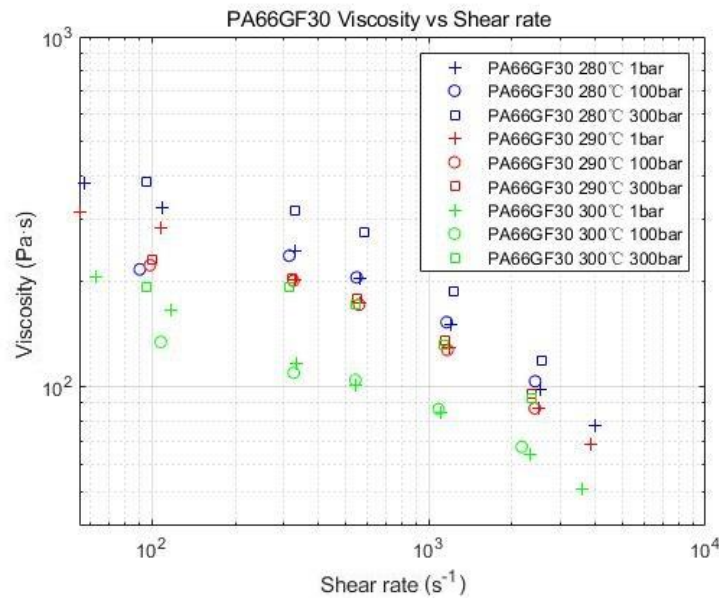


Figure 3.14: Viscosity curves for PA66 with 1bar/100bar/300bar back pressure at different temperatures

It can be seen from the figures that at the same temperature, with the back pressure increase the viscosity of ABS and PA66GF30 also increases. This can be explained by the free volume principle. The increase in pressure causes the polymer molecular chains to be compressed, so the gap between the polymer molecules becomes smaller, that means the free volume decreases. According to Doolittle equation (2.9), the decrease of free volume will lead to the increase of polymer shear viscosity η .

Since the zero-shear-rate viscosity cannot be measured, only equation (2.34) can be used to obtain the pressure coefficient β . Therefore, by plotting the viscosity and mean pressure at the same shear rate and temperature, the slope is the pressure coefficient β .

The $\ln(\eta)$ versus mean pressure of ABS is shown in Figure 3.15, Figure 3.16 and Figure 3.17. The $\ln(\eta)$ versus mean pressure of PA66GF30 is shown in Figure 3.18, Figure 3.19 and Figure 3.20.

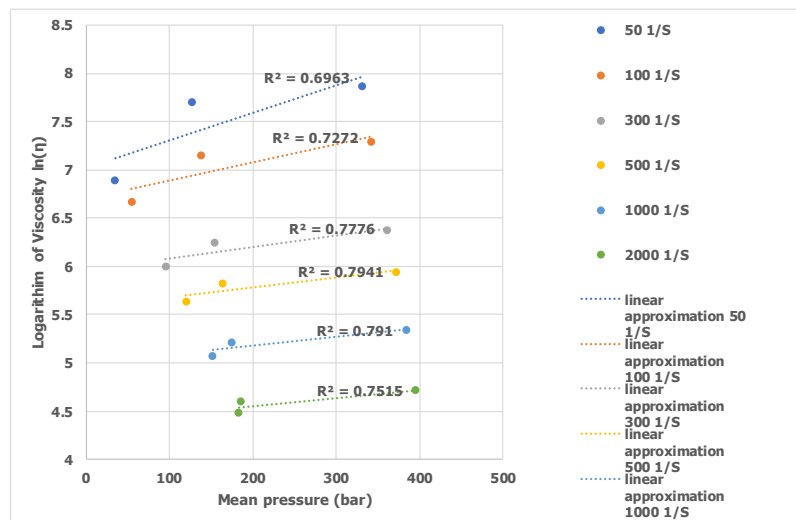


Figure 3.15: Logarithm of viscosity $\ln(\eta)$ versus mean pressure (p_m) curves of ABS at 230°C

3. Experimental Details

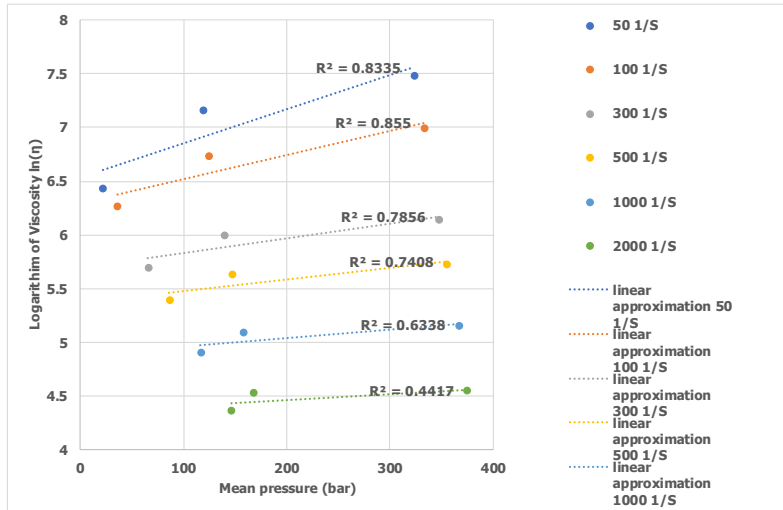


Figure 3.16: Logarithm of viscosity $\ln(\eta)$ versus mean pressure (p_m) curves of ABS at 250°C

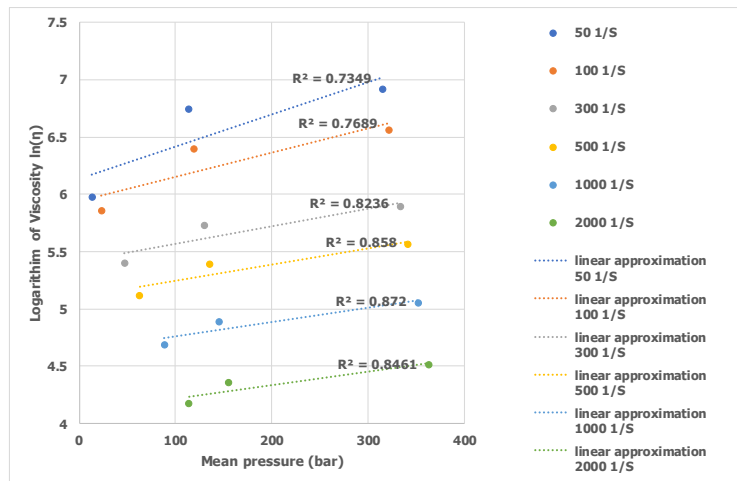


Figure 3.17: Logarithm of viscosity $\ln(\eta)$ versus mean pressure (p_m) curves of ABS at 270°C

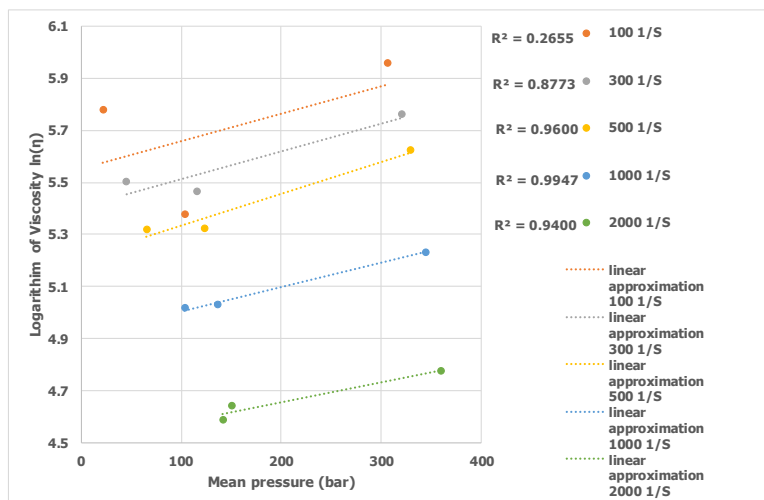


Figure 3.18: Logarithm of viscosity $\ln(\eta)$ versus mean pressure (p_m) curves of PA66GF30 at 280°C

3. Experimental Details

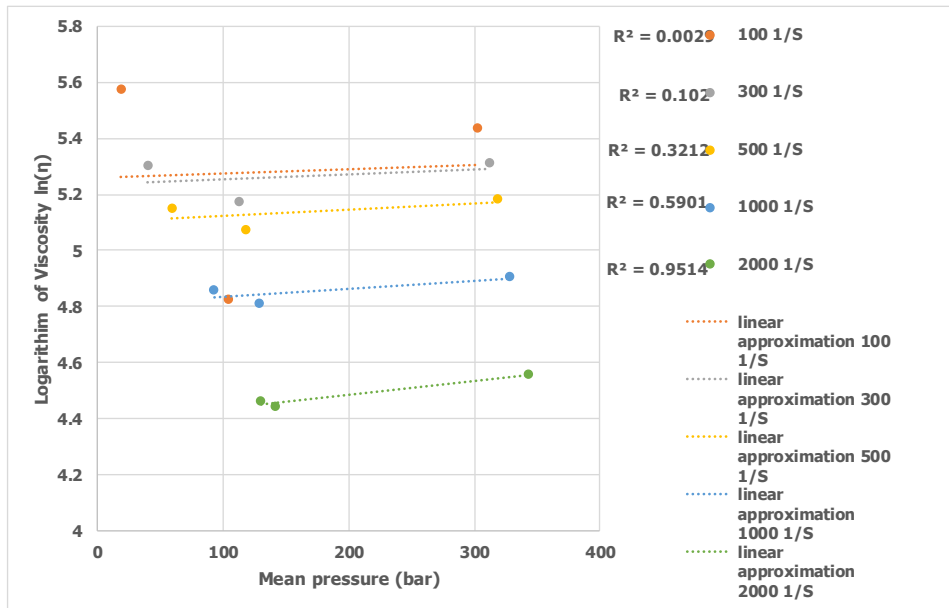


Figure 3.19: Logarithm of viscosity $\ln(\eta)$ versus mean pressure (p_m) curves of PA66GF30 at 290°C

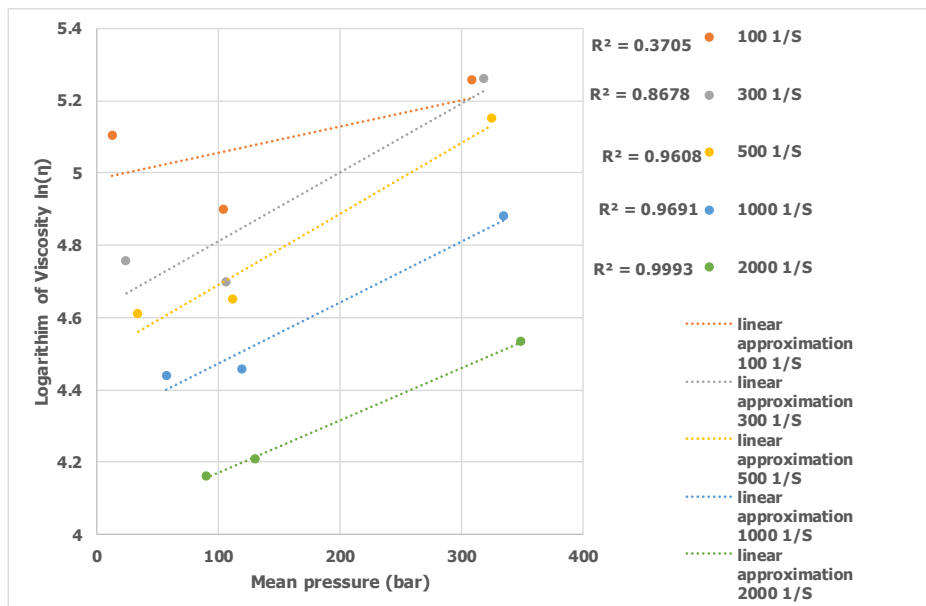


Figure 3.20: Logarithm of viscosity $\ln(\eta)$ versus mean pressure (p_m) curves of PA66GF30 at 300°C

It can be seen that $\ln(\eta)$ increases with increasing pressure. The R^2 values are shown in the captions as well. Since there were only 3 different back pressures, the linear approximation results are poor, especially for PA66GF30 at low shear rates. According equation (2.34), the β values of both materials were calculated and the results are shown in Table 3.11 and Table 3.12.

Table 3.11: Pressure coefficient β for ABS

Shear rate (s^{-1})	Pressure coefficient β in (bar^{-1})		
	230°C	250°C	270°C
50	0.002857	0.003195	0.002793
100	0.001888	0.002244	0.00212
300	0.001186	0.001375	0.001545
500	0.001022	0.001063	0.001431
1000	0.000912	0.00078	0.001244
2000	0.000838	0.000549	0.001169

Table 3.12: Pressure coefficient β for PA66GF30

Shear rate (s^{-1})	Pressure coefficient β in (bar^{-1})		
	280°C	290°C	300°C
100	0.00105	0.00015	0.00072
300	0.00106	0.00018	0.0019
500	0.00123	0.00023	0.00196
1000	0.00093	0.00029	0.00169
2000	0.00077	0.0005	0.00145

Comparing the data of ABS and PA66GF30 at the same shear rate, it can be seen that ABS has a larger β value, indicating that ABS is more sensitive to pressure than PA66GF30. This can be attributed to the hydrogen-bonded grid structure of PA66GF30 which can better prevent the compression of molecular chains. On the other hand, the addition of glass fibers reduces the free volume in PA66GF30 and the compressible space between molecules.

The pressure coefficient β versus shear rate was plotted and the results are shown in Figure 3.21 and Figure 3.22.

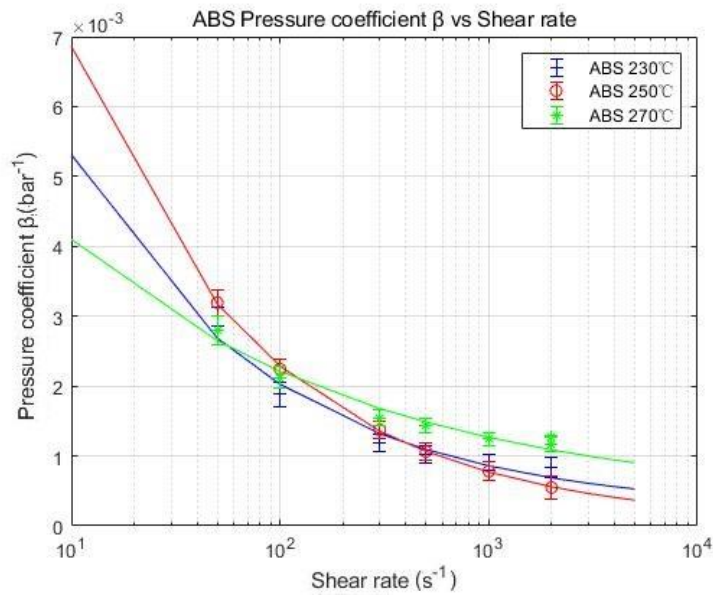


Figure 3.21: Pressure coefficient β as a function of shear rate for ABS in accordance with equation (2.34)

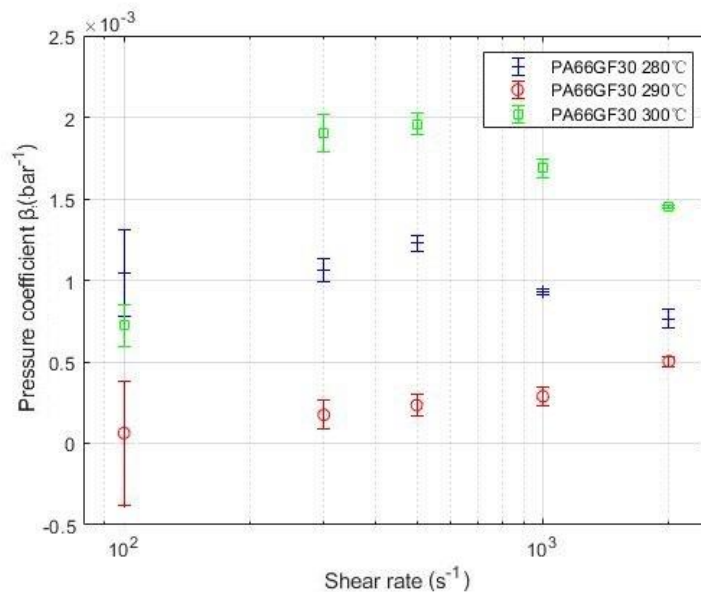


Figure 3.22: Pressure coefficient β as a function of shear rate for A66GF30 in accordance with equation (2.34)

It can be seen that for ABS at the same temperature, the pressure coefficient β will decrease as the shear rate increases and will tend to reach a fixed value at high shear rates. This can be explained by the free volume theory. As the shear rate increases, the polymer chains will disentangle and align along the direction of flow and the free volume is reduced. At the high shear rate range, all polymer chains have been straightened, closely aligned with each other which leads to a minimum free volume. The material no longer exhibits a significant compressibility. So, the β value shows a fixed value close to zero. For PA66GF30, the β value of PA66 decreases with temperature increase before 300°C and then increases with

temperature increase. And no effect of shear rate can be evinced from the data since the effect is within the error bars.

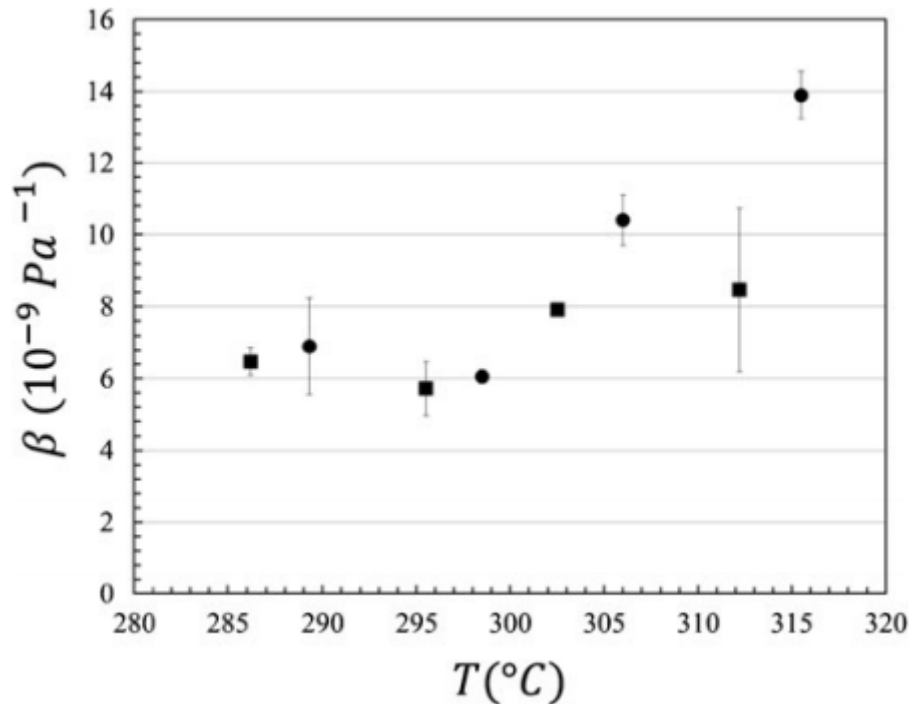


Figure 3.23: Evolution of the pressure coefficient β with temperature for PA66 at 224 s^{-1} (circle) and 447 s^{-1} (square). Data are drawn from Ceccia [63]

The experimental result of Ceccia [63] shows that the β value of PA66 decreased with increasing temperature below 300°C , and then increased with increasing temperature showing a large deviation at low shear rates. The trends and deviations are consistent with the results in this thesis.

Another way to calculate the pressure coefficient β is to adopt the superposition method [43]. The time-pressure superposition principle was applied to produce a master curve of reduced viscosity versus reduced shear rate at reference pressure $p_0=1\text{bar}$. The pressure shift factor, α_p , was related to the pressure coefficient β by the exponential relation

$$\alpha_p = e^{\beta(p_m - p_0)} \quad (3.1)$$

3. Experimental Details

Figure 3.25 and Figure 3.26 show the master curves for both materials with different temperatures.

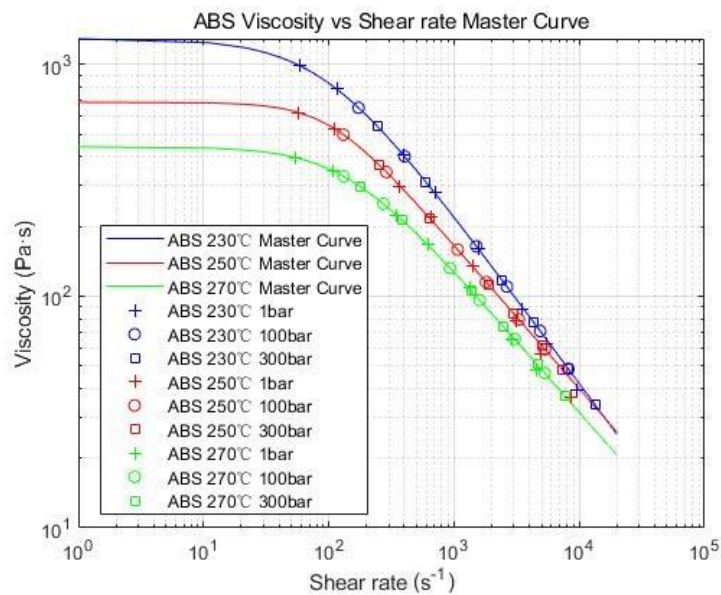


Figure 3.24: Viscosity master curves independent of pressure for ABS (reference at atmospheric pressure), shift factors α_p estimated from capillary rheometer data

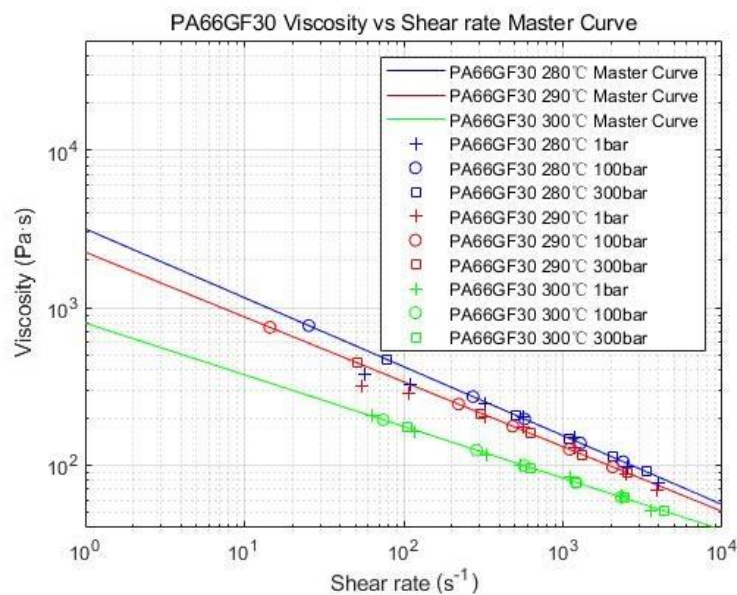


Figure 3.25: Viscosity master curves independent of pressure for PA66GF30 (reference at atmospheric pressure), shift factors α_p estimated from capillary rheometer data

It can be seen from the figures that this method results in good fitting for ABS, but for PA66GF30, due to the use of the power law model, there is a significant deviation when the shear rate is less than 100s^{-1} . The results for the pressure coefficient β obtained by this method are shown in Table 3.13 and Table 3.14.

3. Experimental Details

Table 3.13: Pressure coefficient β for ABS calculated by master curve method

		Pressure coefficient β in (bar^{-1})					
Temp.		50 s^{-1}	100 s^{-1}	300 s^{-1}	500 s^{-1}	1000 s^{-1}	2000 s^{-1}
100 bar	230°C	0.009689	0.008439	0.007462	0.006853	0.005515	0.003896
	250°C	0.008055	0.007259	0.006739	0.006048	0.004593	0.002703
	270°C	0.008441	0.007374	0.006566	0.006094	0.004923	0.003355
300 bar	230°C	0.00476	0.004542	0.004479	0.004309	0.003795	0.003032
	250°C	0.004869	0.004869	0.004112	0.00365	0.002853	0.001801
	270°C	0.003899	0.003728	0.003721	0.00371	0.003226	0.002507

Table 3.14: Pressure coefficient β of PA66GF30 by master curve method

		Pressure coefficient β in (bar^{-1})				
Temp.		100 s^{-1}	300 s^{-1}	500 s^{-1}	1000 s^{-1}	2000 s^{-1}
100 bar	280°C	-0.01231	-0.00131	0.000436	0.000913	0.000307
	290°C	-0.01713	-0.00174	0.000481	0.001227	0.00047
	300°C	-0.00358	-0.00121	0.00047	0.00089	0.00057
300 bar	280°C	-0.00062	0.00134	0.00191	0.00149	0.00074
	290°C	-0.00218	-0.00016	0.00036	0.00046	0.00019
	300°C	0.00034	0.0022	0.00247	0.00227	0.00172

Comparing the β value of ABS at the same temperature and shear rate, it can be found that the β decreases as the pressure increases. This can be explained by the SS hole theory. Under this theory, the compression of the polymer is due to a large enough hole to accommodate the chain segment, and the energy barrier to overcome for the rotation of molecular segments is less affected by pressure than the free volume. Therefore, the volume and number of holes are decreased with the pressure increase and lead to a reduction of the β value [29].

The β values evaluated by the pressure coefficient definition (Barus equation) and by the superposition method were compared, as shown in Figure 3.26 and Figure 3.27.

It can be seen that for ABS both methods show the same trend. The pressure coefficient β decreases with increasing temperature or shear rate. The difference in the decrease of the pressure coefficient β for ABS according to the temperature rise within the measuring range was 10^{-3} bar^{-1} , and the difference according to the increase in shear rate was $3 \cdot 10^{-3} \text{ bar}^{-1}$.

Both methods show that the pressure coefficient of PA66GF30 decreases first by about $2 \cdot 10^{-3} \text{ bar}^{-1}$ and then rises again for increasing temperature while the shear rate shows little effect on pressure coefficient, and the difference was within $0.5 \cdot 10^{-3} \text{ bar}^{-1}$. Sometimes the evaluation procedure produces also negative results. The results show that the pressure coefficient β of ABS is more sensitive to shear rate and PA66GF30 is more sensitive to temperature in the testing range. This may be due to the proportion of acrylonitrile in ABS which is relatively low (15%-30%), so the content of cyanide (-CN) groups is lower, which makes ABS closer to non-polar materials, while PA66 has amide (-NHCO-CH₃-) groups as a strong polar group and contains a large number of hydrogen bonds. Probably, the internal hydrogen bonds break and the crosslinking reaction is greatly affected by temperature.

3. Experimental Details

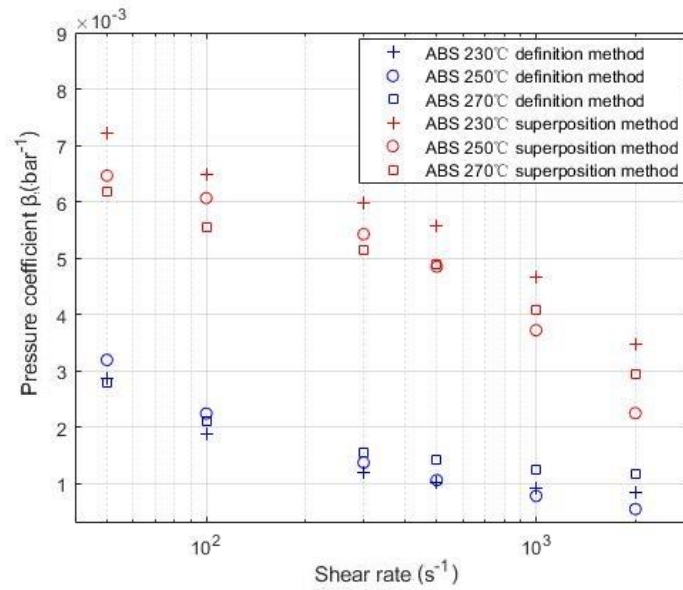


Figure 3.26: Pressure coefficient β for ABS estimated by the definition and the superposition method

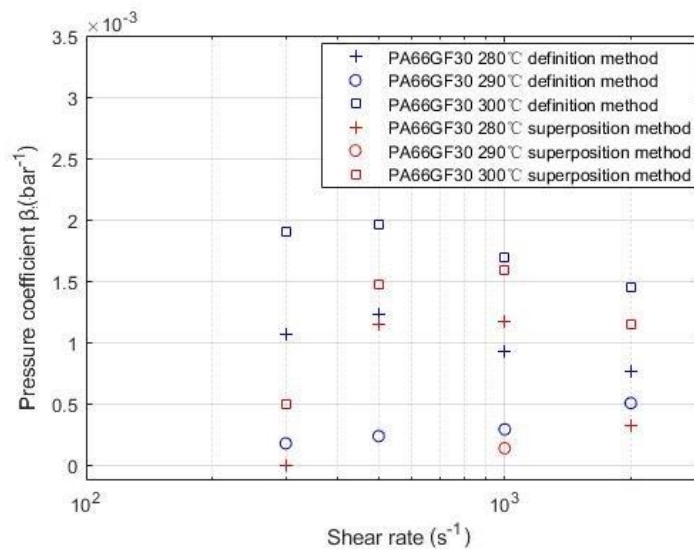


Figure 3.27: Pressure coefficient β for PA66GF30 estimated by the definition (Barus equation) and the superposition method

Another reason may be due to experimental errors. Since to the poor thermal stability of PA66GF30, although measurements at the HPCR are following the first-in-first-out (FIFO) rule, the residence time of samples in the equipment was still too long. At the same time, for PA66GF30, its low shear viscosity leads to low pressures and low shear stresses, as shown in Table 3.7, so larger measurement errors will occur within the sensor sensitivity range. It may eventually lead to an error in the level of 10^{-3} bar^{-1} .

3. Experimental Details

Table 3.7: Measured pressure for PA66GF30 at 290°C using a capillary with 10 mm die-length

Shear rate	Measured pressure in (bar)				
	50 s ⁻¹	100 s ⁻¹	300 s ⁻¹	500 s ⁻¹	1000 s ⁻¹
Back pressure 100 bar	1.7	5.0	19.9	33.2	52.4
Back pressure 300 bar	5.0	9.2	26.1	39.5	61.9

Table 3.8 shows some currently published pressure coefficient values in comparison with values obtained from the experiment. It can be seen that because of the different composition of the ABS types analyzed (e.g. the AN-content of each component), each result is different but in the order of magnitude they are the same. Because of the high glass fiber content in PA66GF30 the pressure coefficient β which shows the pressure sensitivity, is by a factor of three lower than for pure PA66.

Table 3.8: Comparison of measured pressure coefficient β with values from literature

	Pressure coefficient β in (bar ⁻¹)			
	Measured in the present study	Aho [43]	Kadijk and van den Brule [55]	Ceccia[63]
ABS at 230°C	0.00286	0.00337	0.00245	-
PA66 at 290°C	-	-	-	0.00065
PA66GF30 at 290°C	0.00023	-	-	-

4 Numerical fitting based on SIGMASOFT ® VIRTUAL MOLDING

4.1 High pressure capillary rheometer simulation

HPCR simulations were carried out to better understand the rheological behavior in the pressure field and were used to verify the processing method for the experimental results. The simulation tool used was Sigmasoft® Virtual Molding (referred to as Sigmasoft®) from SIGMA Engineering GmbH. 3D simulations were used to simulate the melt flowing process through the capillary.

The quality of the mesh division directly affects the most important analysis results of the product. In theory, the smaller the grid division, the more accurate the calculation result is. However, in actual analysis, the size of the grid should be determined according to the actual application's accuracy requirements, computer capacity, and calculation time. Too small a grid will reduce accuracy. According to the research of Gong [74] for the irregular shape model, as the element size decreases, the simulation results gradually converge to the theoretical value, but start to deviate from the theoretical value after reaching a certain value. This is because the shape is irregular, and the continued shrinking of the unit leads to an increase in the number of irregular units, causing an increase in errors. At the same time, when the element size is reduced to a certain extent, the relative error of the simulation results tends to decrease, while the running time and the required memory increase exponentially, so it is necessary to conduct multiple tests on the meshing.

Since the simulation analysis software cannot apply the back pressure at the entrance, the simulated pressure is actually the pressure drop measured before the entrance minus the exit pressure.

In order to analyze the reliability of the pressure dependent viscosity by the mean pressure processing method, the pressure dependent viscosity data processed by entry pressures were input in Sigmasoft® as a comparison.

In this thesis, a sensitivity analysis of the mesh quality was performed first. Then the simulation results in which the viscosities were obtained by the mean pressure method and by the entry pressure method were compared to the experimental results. Finally, all measuring conditions A1.1-A6.2 and B1.1-B6.2 were simulated.

4.1.1 3D model

The model of the high pressure capillary rheometer with the standard round die (capillary length 10/30mm, diameter 1mm) was set up, the cavity at the entrance space and the pressure sensor, and directly the entrance was set on the upper surface of the cavity and the outlet was set on the lower surface of the capillary, as shown in the Figure 4.1.

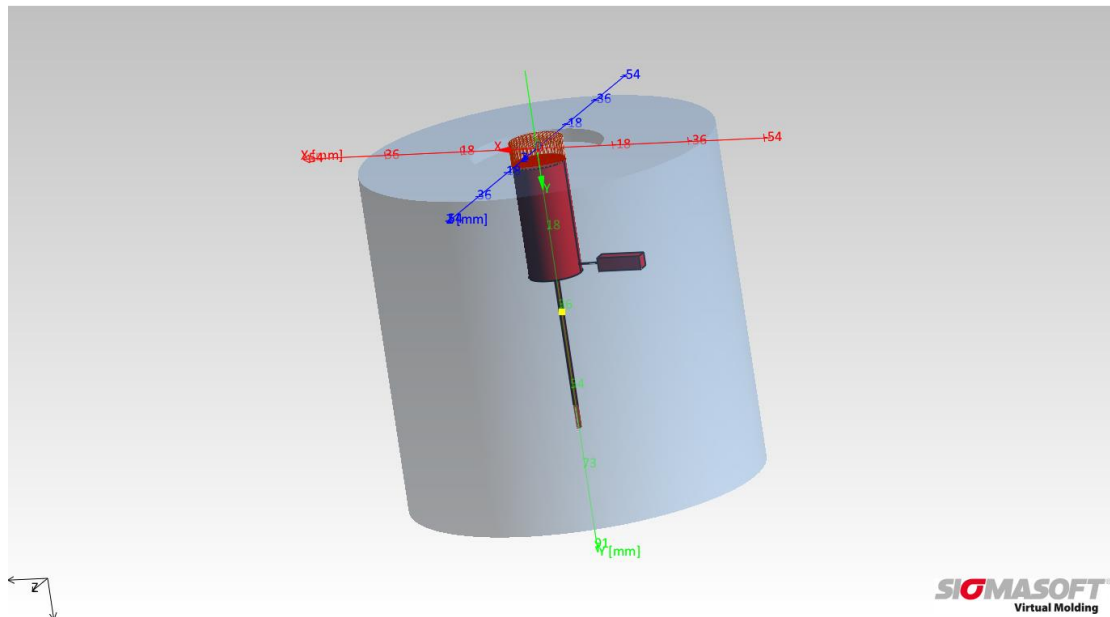


Figure 4.1: the 3D solid modeling of the rheometer die and the pressure hole with the pressure sensor

4.1.2 Meshing

Since the cylindrical filling chamber is not the main part of the simulation a rough mesh is used with a mesh length of 5mm.

The first mesh length for the capillary is 0.2mm and the number of cells is 261,520. The chosen mesh size is shown in Figure 4.2. The thin wall cells are located at the pressure hole of the pressure sensor (see Figure 4.3).

Mesh Size			
Number of cartesian cells	9,753,600	Number of cartesian cavity cells	261,520
Number of composed cells	415,954	Number of composed cavity cells	71,225
Mesh Quality			
Blocked cells	0	0.0	%
Edge-over-edge connected cells	0	0.0	%
Thin wall elements	40	0.0	%
Two wall cells	0	0.0	%
Air contact cells	0	0.0	%

Figure 4.2: Mesh size and quality for the capillary with 0.2mm mesh length

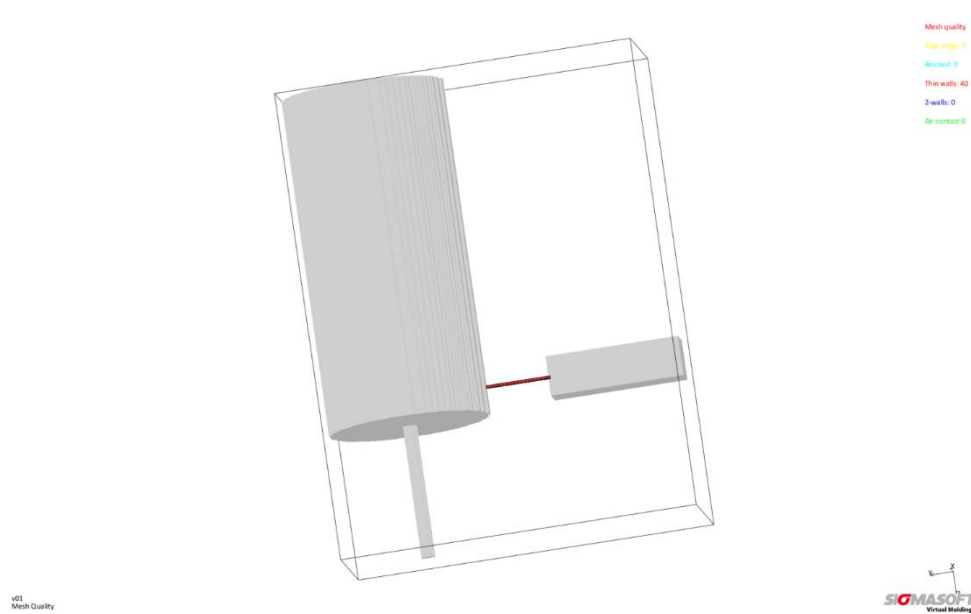


Figure 4.3: Pressure hole with thin wall cells of 0.2mm mesh length

A second mesh for the capillary was performed with a mesh length of 0.1mm and a number of 665,480 cells (see Figure 4.4).

Mesh Size			
Number of cartesian cells	19,270,656	Number of cartesian cavity cells	665,480
Number of composed cells	717,219	Number of composed cavity cells	157,140
Mesh Quality			
Blocked cells	0	0.0 %	
Edge-over-edge connected cells	0	0.0 %	
Thin wall elements	0	0.0 %	
Two wall cells	140	0.0 %	
Air contact cells	2,792	0.4 %	

Figure 4.4: Mesh size and quality for the capillary with 0.1mm mesh length

The air contact cells are located at the capillary elements after the die-exit, and two wall cells are located at the pressure sensor (see Figure 4.5).

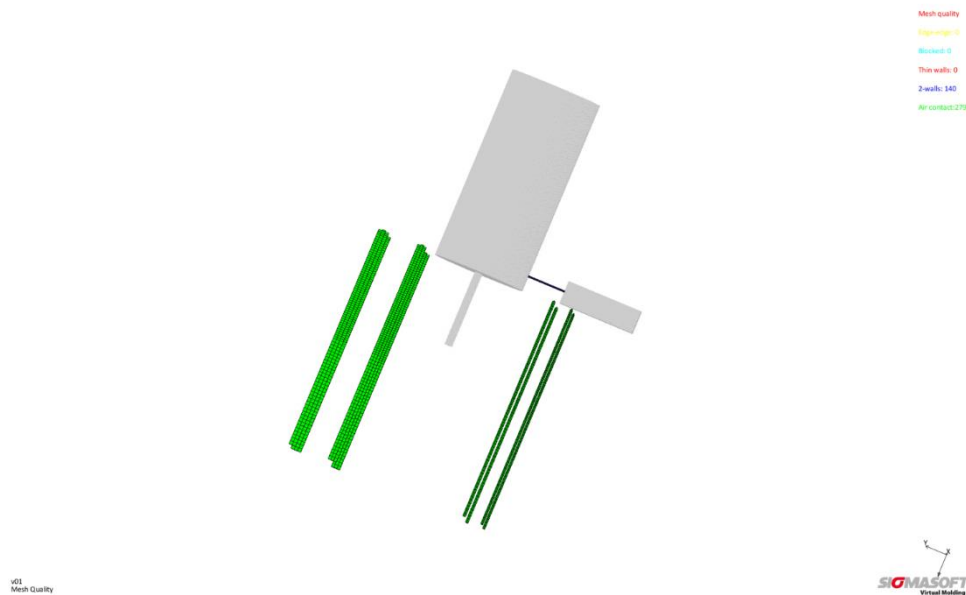


Figure 4.5: Location of the two wall cells and the contract cells of 0.1mm mesh length

Compared to 0.2mm mesh size, the air contact cells may be do not fit well to each other due to changing the mesh size of the capillary which leads to the mesh of the cylindrical filling chamber. Since the chamber is not a main part of simulation, it will not affect the final result. In this case, all meshing qualities meet the requirements.

4.1.3 Setting process data

As mold material a steel from the material database of Sigmasoft® software was used. Its Young's modulus is shown in Figure 4.6.

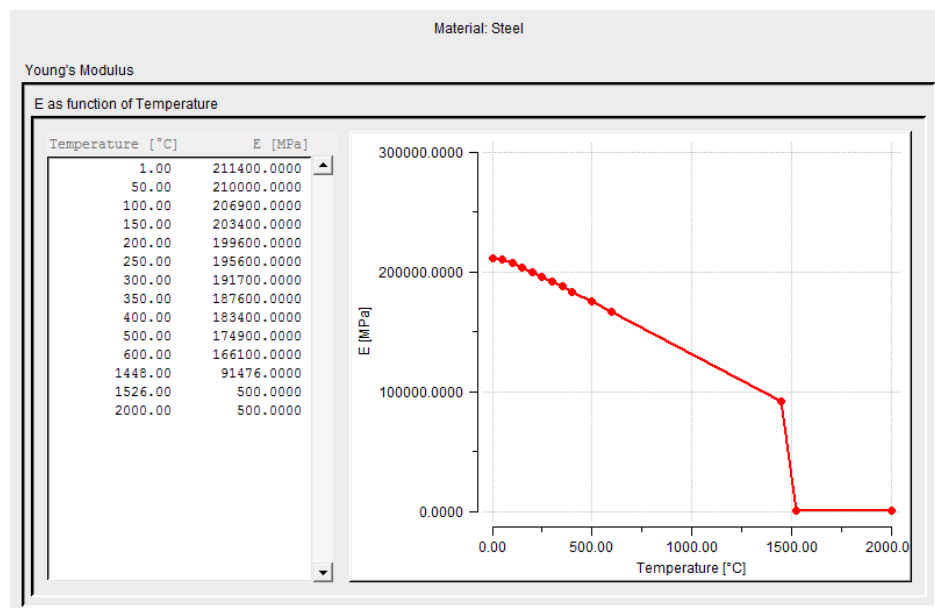


Figure 4.6: Young's modulus of the selected mold steel

As material data for the simulation the measured data for both materials (ABS, PA66GF30) were inputted into Sigmasoft's own material database (SIGMAdata) such as the pvT curve, specific heat capacity, thermal conductivity, and the viscosity curves at different temperatures. The fitting curves using cross-WLF model (Equations(4.1),(4.2)) for ABS and Carreau-WLF model (Equations 4.3, 4.4) for PA66GF30 as well as the model parameters were generated by means of SIGMAdata. They are shown in Table 4.1 and Table 4.2.

$$\eta(T, \dot{\gamma}, p) = \frac{\eta_0}{1 + \left(\frac{\eta_0 \cdot \dot{\gamma}}{D_4}\right)^{1-n}} \quad (4.1)$$

$$\eta_0(T, p) = D_1 \cdot \exp\left(-\left(\frac{A_1 \cdot (T - D_2 - D_3 \cdot p)}{A_2 + T - D_2}\right)\right) \quad (4.2)$$

Where η_0 is the zero shear rate viscosity, n is the Cross exponent, A_1 is the factor describing the temperature dependency, A_2 is the factor describing the temperature dependency, D_1 is the viscosity at reference temperature, D_2 is the reference temperature, D_3 is the factor describing the pressure dependency, D_4 is the transition shear stress.

$$\eta(T, \dot{\gamma}) = \frac{p_1 \cdot a_T}{(1 + p_2 \cdot a_T \cdot \dot{\gamma})^{p_3}} \quad (4.3)$$

$$\log a_T = \frac{8.86 \cdot (T_0 - T_s)}{101.6 + (T_0 - T_s)} - \frac{8.86 \cdot (T - T_s)}{101.6 + (T - T_s)} \quad (4.4)$$

Where p_1 is the zero shear rate viscosity, p_2 is the reciprocal transition shear rate, p_3 is the Carreau exponent, a_T is the Arrhenius temperature shift factor, T_0 is the reference temperature and T_s is the standard temperature.

Figure 4.7, Figure 4.8, Figure 4.9 and Figure 4.10 show the viscosity curves of ABS and PA66GF30 and its corresponding model parameters fitted by SIGMAdata.

Table 4.1: Viscosity data for ABS at three selected temperatures and two back pressure levels used in the Sigmasoft® simulation and determined for the "mean pressure" method taking into account the Bagley and Weissenberg-Rabinowitsch correction.

Viscosity under certain conditions			Data for the simulation						
230°C/100bar	shear rate	s ⁻¹	51	127	479	864	1873	3993	6109
	viscosity	Pa.s	2218	1273	516	336	184	100	68
250°C/100bar	shear rate	s ⁻¹	51	117	421	747	1603	3387	5193
	viscosity	Pa.s	1283	843	403	278	163	92	65
270°C/100bar	shear rate	s ⁻¹	51	114	399	703	1498	3157	4838
	viscosity	Pa.s	851	597	308	219	133	78	56
230°C/300bar	shear rate	s ⁻¹	51	127	485	877	1910	4069	6168
	viscosity	Pa.s	2601	1461	586	380	208	112	75

4. Numerical fitting based on SIGMASOFT ® VIRTUAL MOLDING

Viscosity under certain conditions			Data for the simulation						
250°C/300bar	shear rate	s ⁻¹	52	127	457	817	1766	3730	5763
	viscosity	Pa.s	1776	1095	463	308	173	95	66
270°C/300bar	shear rate	s ⁻¹	52	116	399	703	1488	3113	
	viscosity	Pa.s	1013	705	362	261	157	92	

Table 4.2: Viscosity data for PA66GF30 at s three selected temperatures and two back pressure levels used in the Sigmasoft® simulation and determined for the “mean pressure” method taking into accout the Bagley and Weissenberg-Rabinowitsch correction

Viscosity under certain conditions			Data for the simulation						
280°C/100bar	shear rate	s ⁻¹	39	90	313	549	1160	2423	
	viscosity	Pa.s	85	216	237	205	153	104	
290°C/100bar	shear rate	s ⁻¹	47	98	324	560	1168	2415	
	viscosity	Pa.s	251	222	201	171	127	87	
300°C/100bar	shear rate	s ⁻¹	53	108	325	543	1085	2166	
	viscosity	Pa.s	191	134	110	104	86	67	
280°C/300bar	shear rate	s ⁻¹	43	96	330	584	1227	2553	
	viscosity	Pa.s	346	387	318	277	187	118	
290°C/300bar	shear rate	s ⁻¹	48	100	322	553	1146	2361	
	viscosity	Pa.s	262	230	203	179	135	95	
300°C/300bar	shear rate	s ⁻¹	45	95	314	544	1136	2355	
	viscosity	Pa.s	176	192	193	172	132	93	

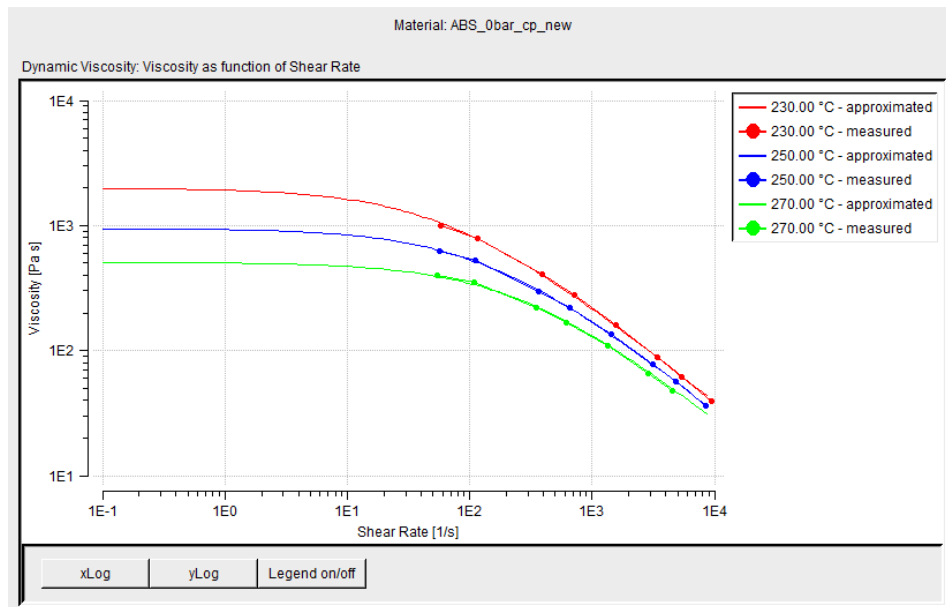


Figure 4.7: Viscosity versus shear rate at 230/250/270°C for ABS; curves fitted with SIGMAdata

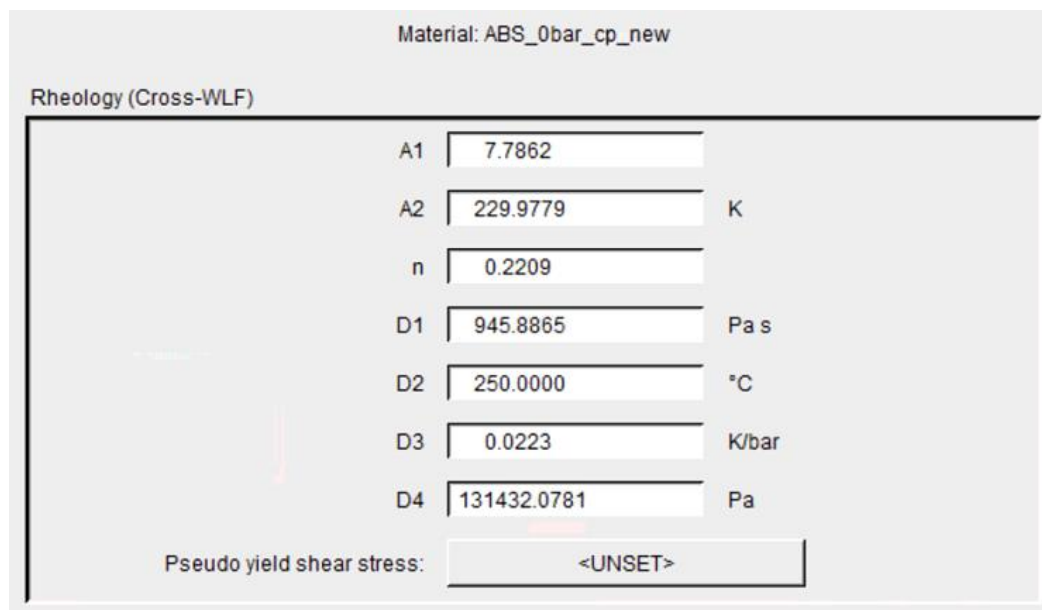


Figure 4.8: Cross-WLF model parameters for ABS, fitted with SIGMAdata

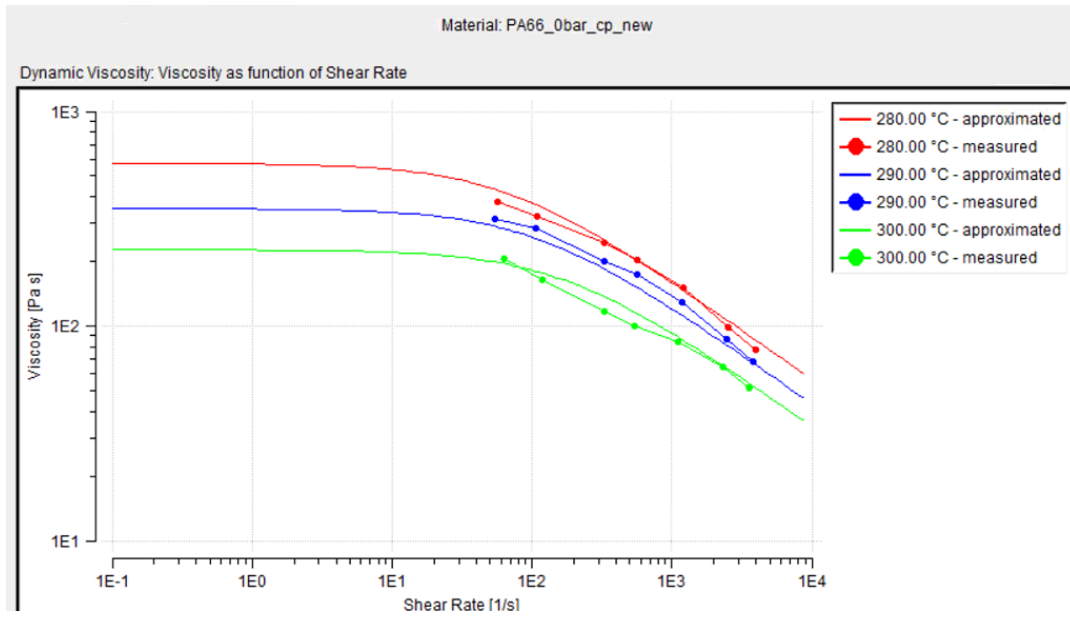


Figure 4.9: Viscosity versus shear rate at 280/290/300°C for PA66GF30; curves fitted with SIGMAdata

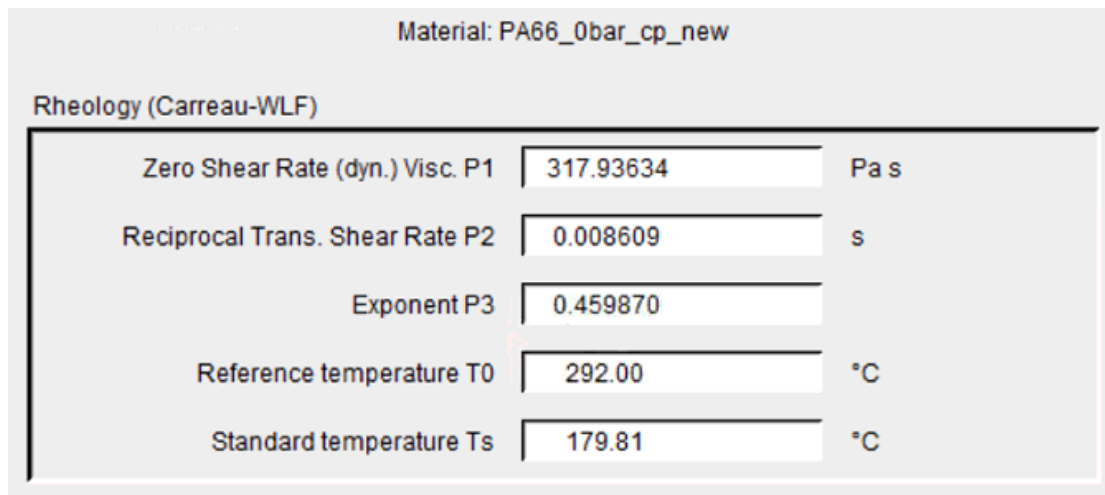


Figure 4.10: Carreau-WLF model parameters for PA66GF30, fitted with SIGMAdata

To verify the reliability of the data processing of the shear viscosity for ABS and for comparison with Table 4.1, Table 4.3 shows the values determined with the "entrance pressure" method.

Table 4.3: Viscosity data for ABS at three selected temperatures and two back pressure levels used in the Sigmasoft® simulation and determined for the "entrance pressure" method taking into account the Bagley and Weissenberg-Rabinowitsch correction

Viscosity under certain conditions			Data for the simulation						
230°C/100bar	shear rate	s ⁻¹	65	125	454	845	1937	4356	6785
	viscosity	Pa.s	1747	1286	546	343	178	91	61
250°C/100bar	shear rate	s ⁻¹	60	118	403	732	1642	3623	5652
	viscosity	Pa.s	1086	847	421	284	159	87	60
270°C/100bar	shear rate	s ⁻¹	57	115	387	692	1516	3300	5139
	viscosity	Pa.s	764	598	317	222	131	75	52
230°C/300bar	shear rate	s ⁻¹	68	126	453	855	1999	4542	6931
	viscosity	Pa.s	1954	1480	627	390	199	101	67
250°C/300bar	shear rate	s ⁻¹	59	125	442	803	1784	3873	6079
	viscosity	Pa.s	1566	1095	478	313	172	91	63
270°C/300bar	shear rate	s ⁻¹	60	116	386	699	1541	3370	
	viscosity	Pa.s	893	700	375	263	151	84	

The constant heat transfer coefficient selected for the simulation was 1,000 W/m²K. Since the capillary rheometer did not need the process to open/close the mold, the temperature was directly set as the experimental temperature (ABS: 230/250/270°C, PA66GF30 280/290/300°C), and there was no need to set a heating-up and cooling time.

For definition of the filling phase the flow rate over the whole rheological experiment had to be defined. As the simulation software does not need to manually control the back pressure, the volume flow rate was first set to 4 cm³/s for 1 second to completely fill the capillary with polymer melt. After that, the flow rate was increased every 10s according to the rheological experiment corresponding to the values 0.00491/0.00982/0.0295/0.0491/0.0982 /0.196/0.02945 cm³/s. These values correspond to the apparent shear rate of 50/100/300/500/1000/3000 s⁻¹. Finally, the flow rate was set to zero. The "mold open" definition was set after the last flow rate was completed.

4.2 Numerical Results

The material parameters fitted by SIGMAdata, and the results obtained from the rheological experiments are compared as viscosity versus shear rate curves. The results are shown in Figure 4.11 and Figure 4.12.

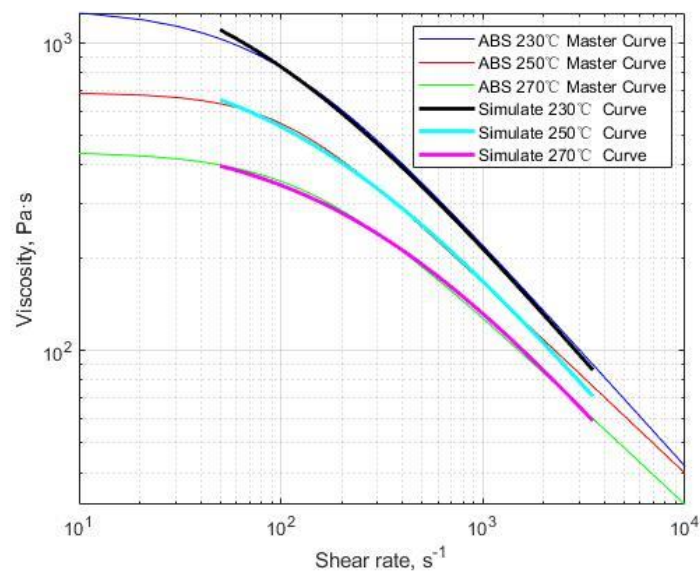


Figure 4.11: Viscosity versus shear rate curves for ABS, experimental results and calculated curves using Sigmasoft® simulations

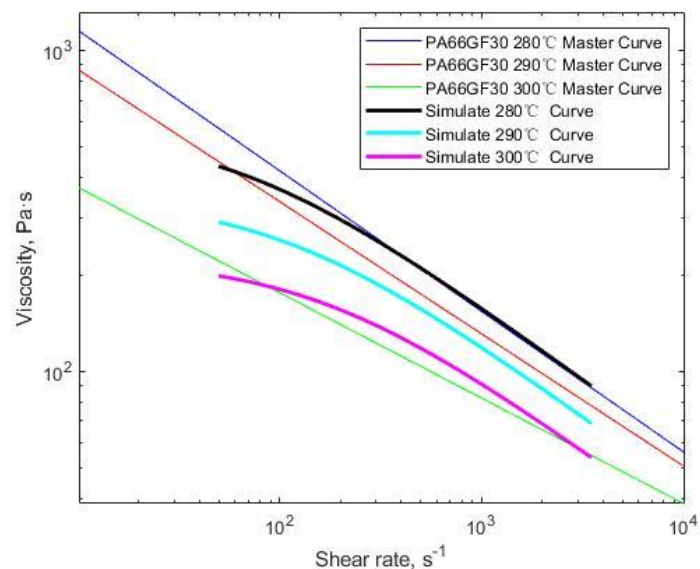


Figure 4.12: Viscosity versus shear rate curves for PA66GF30, experimental results and calculated curves using Sigmasoft® simulations

It can be easily seen from both figures that the Sigmasoft® fitted curves for ABS are in good agreement with the experimentally determined master curves, while for PA66GF30 a poor agreement in the transition area is obvious. The reasons for the deviation could be the use of the power law model for calculating the master curve.

Since in flow simulation there is no material shrinkage for different filling times the pressure in the cylindrical filling chamber remains constant (see Figure 4.13).

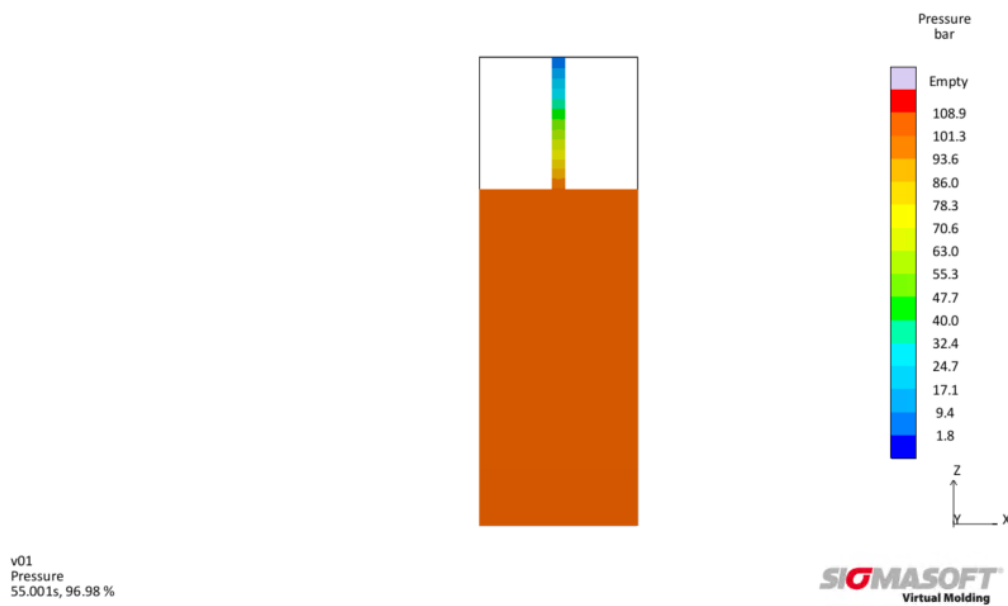


Figure 4.13: Simulated pressure in the cylindrical filling chamber and the capillary

The analysis of the results is only to compare the difference between the pressure obtained by the experiment and the pressure obtained by the simulation.

The pressure versus time curve is obtained through Sigmasoft® simulation. Figure 4.14 and Figure 4.15 show the curve of ABS (at 230°C) and PA66GF30 (at 290°C) when the capillary die length is 10mm with back pressure at 100 bar and the mesh length is 0.1 mm.

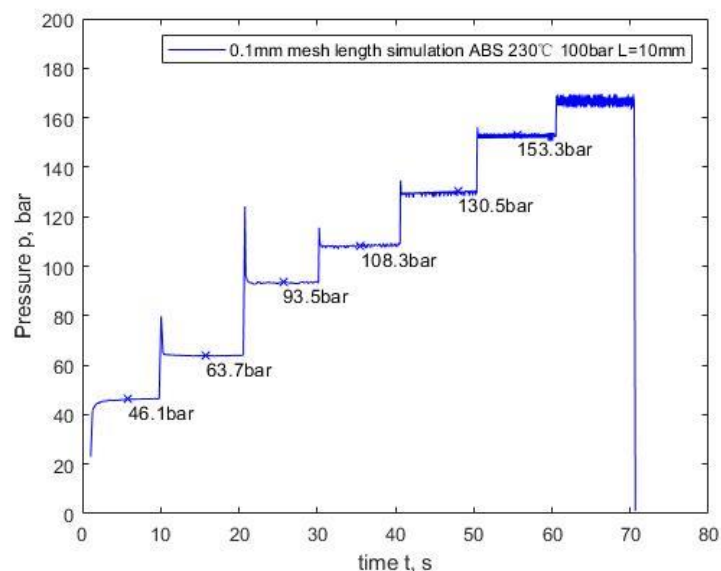


Figure 4.14: Simulated pressure versus time for ABS

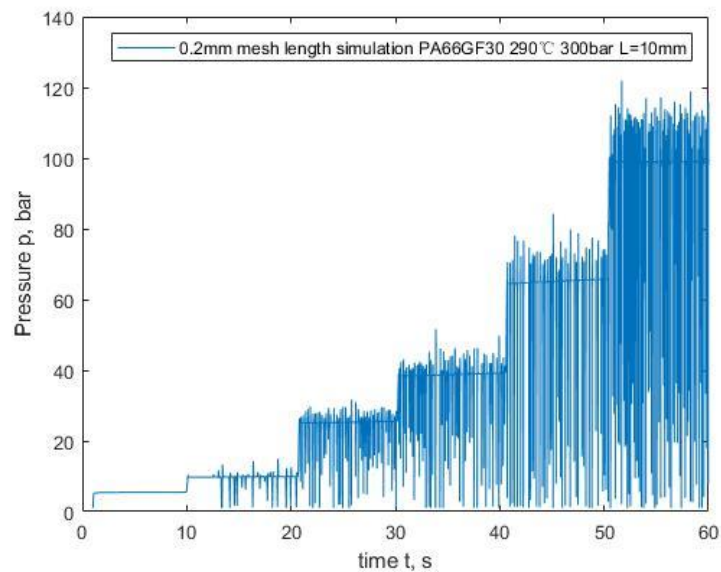


Figure 4.15: Simulated pressure versus time for PA66GF30

It can be clearly seen that at the speed change point, because the speed of the simulation software is abrupt, there will be a pressure peak, and then the curve will be flat again, but it has no effect on the simulation result. At the same time, it can be seen from the extruded strands that as the shear rate increases, the shear stress exceeds the critical shear stress, so the well-known stick-slip effect between the mold walls and melt appeared, which caused the pressure to fluctuate. This effect was especially obvious for PA66GF30, and it was also in actual experiments where the melt fracture phenomenon was found, as shown in Figure 4.16.



Figure 4.16: Melt fracture phenomenon in lab experiment for PA66GF30

4.2.1 Influence of mesh size

To determine the influence of mesh size, the rheometer flow of selected experiments were simulated with the side length of 0.2mm and 0.1mm, and the parameter settings were kept

consistent. Figure 4.17 shows the comparison between the simulation results with different mesh sizes and lab results of ABS at 270°C, a back pressure of 300 bar, and the capillary length of 10mm.

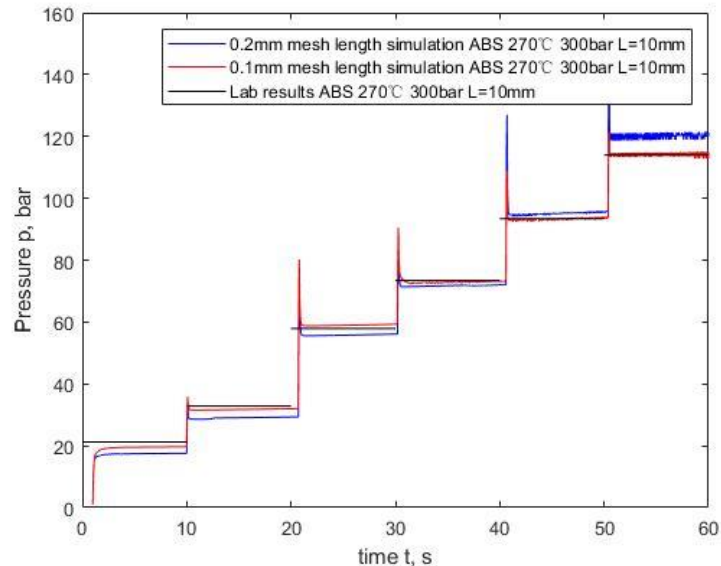


Figure 4.17: Sigmasoft® simulation and pressure curves from the pressure sensor versus time of the experiments for ABS ($T=270^{\circ}\text{C}$, 300 bar back pressure); 0.2 mm mesh length (blue), 0.1 mm mesh length (red), lab results (black)

It can be clearly seen that as the fineness of the grid increases, the simulation results are closer to the actual experimental results.

In the rest simulation, 0.1mm mesh length was used.

4.2.2 Influence of data processing

To determine the data processing influence, the simulations of the data processed by mean pressure and entrance pressure under the same conditions. Figure 4.18 compares the difference between the simulated pressures with different data processing and the experimental results at 0.1 mm mesh length, 230°C, and a 300 bar back pressure.

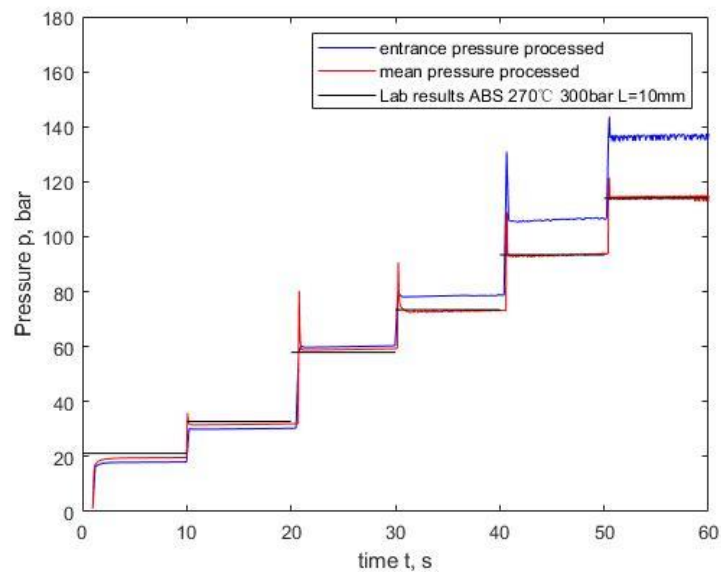


Figure 4.18: Sigmasoft® simulation and pressure curves from the pressure sensor versus time of the experiments for ABS ($T=270^{\circ}\text{C}$, 300 bar back pressure); entrance pressure processed (blue), mean pressure processed (red), lab results (black)

It can be easily seen that the mean pressure processing method used in this thesis has a much smaller deviation from the experimental results than the results of the entrance pressure processing. It shows that the method used in this thesis can be better used to simulate the pressure demand of the rheometer flow taking into account the pressure dependence of viscosity compared to the method entrance pressure processing.

4.2.3 Comparison of simulation results and experimental results

Based on Sigmasoft®, pressure values are calculated and compared with measured data for the pressures in modified high pressure capillary rheometer under conditions A1.1 to A6.2 and B1.1 to B6.2.

Table 4.4 to Table 4.7 show the comparison between the simulation results and the experimental results for ABS and PA66GF30.

Table 4.4: Comparison of simulation results and experimental data for ABS and the capillary with 10 mm length

ABS/10 mm capillary length	Temperature/ back pressure	Data from	Shear rate (s ⁻¹)					
			50	100	300	500	1000	2000
			Pressure (bar)					
280°C/100bar	Lab	45.0	64.6	99.0	116.2	137.9	158.9	
	Simulation	46.1	63.8	93.5	108.3	130.5	153.3	
280°C/300bar	Lab	52.9	74.2	113.6	133.5	158.8	182.0	
	Simulation	56.6	78.1	116.3	134.9	162.1	193.1	
290°C/100bar	Lab	26.0	39.6	67.9	83.0	104.4	125.3	
	Simulation	27.9	42.2	69.6	83.6	103.4	125.3	
290°C/300bar	Lab	37.0	55.4	84.7	100.5	122.5	141.4	
	Simulation	35.8	53.4	84.2	99.5	121.2	142.1	
300°C/100bar	Lab	17.3	27.3	49.2	61.5	79.4	98.5	
	Simulation	15.7	25.5	48.4	61.3	79.5	99.0	
300°C/300bar	Lab	21.2	32.8	57.9	73.4	93.4	114.0	
	Simulation	19.6	31.7	58.9	73.1	93.5	114.0	

Table 4.5: Comparison of simulation results and experimental data for ABS and the capillary with 30 mm length

ABS/ 30 mm capillary length	Temperature/ back pressure	Data from	Shear rate (s ⁻¹)					
			50	100	300	500	1000	2000
			Pressure (bar)					
280°C/100bar	Lab	135.0	193.8	296.9	348.6	413.6	476.8	
	Simulation	134.4	187.2	279.1	325.9	392.7	461.3	
280°C/300bar	Lab	158.8	222.5	340.7	400.5	476.4	545.9	
	Simulation	173.1	234.7	336.5	387.0	454.9	526.7	
290°C/100bar	Lab	93.8	136.3	228.1	280.7	363.2	462.2	
	Simulation	81.4	124.7	209.7	255.2	320.5	391.2	
290°C/300bar	Lab	111.0	166.3	254.0	301.5	367.5	424.3	
	Simulation	105.8	158.7	257.3	308.1	379.2	453.4	
300°C/100bar	Lab	51.8	82.0	147.6	184.6	238.3	295.6	
	Simulation	44.5	74.2	142.5	182.6	242.0	306.4	
300°C/300bar	Lab	63.6	98.3	173.6	220.2	280.3	341.9	
	Simulation	56.2	93.1	174.3	220.4	286.9	357.1	

Table 4.6: Comparison of simulation results and experimental data for PA66GF30 and the capillary with 10 mm length

PA66GF30/10 mm capillary length	Temperature/ back pressure	Data from	Shear rate (s ⁻¹)					
			50	100	300	500	1000	2000
			Pressure (bar)					
280°C/100bar	Lab	1.3	7.8	29.6	45.0	70.9	100.4	
	Simulation	5.9	10.6	27.4	41.3	67.8	101.2	
280°C/300bar	Lab	5.9	14.8	42.0	64.6	91.9	120.9	
	Simulation	7.5	13.7	34.8	52.0	83.8	121.1	
290°C/100bar	Lab	1.7	5.0	19.9	33.2	52.4	81.2	
	Simulation	4.3	7.5	19.3	29.9	51.2	80.6	
290°C/300bar	Lab	5.0	9.2	26.1	39.5	61.9	90.1	
	Simulation	5.5	9.9	25.3	39.1	65.2	95.5	
300°C/100bar	Lab	4.1	5.8	14.3	22.7	37.5	58.3	
	Simulation	2.9	4.8	11.6	18.6	33.5	56.3	
300°C/300bar	Lab	3.2	7.3	24.2	37.5	59.8	87.7	
	Simulation	4.3	7.6	19.5	31.4	52.7	84.5	

Table 4.7: Comparison of simulation results and experimental data for PA66GF30 and the capillary with 30 mm length

PA66GF30/30mm capillary length	Temperature/ back pressure	Data from	Shear rate (s ⁻¹)					
			50	100	300	500	1000	2000
			Pressure (bar)					
280°C/100bar	Lab	4.0	23.4	88.9	135.1	212.8	301.1	
	Simulation	14.7	28.0	73.3	111.7	183.2	269.3	
280°C/300bar	Lab	17.8	44.4	125.9	193.7	275.7	362.8	
	Simulation	18.9	36.1	94.2	141.9	227.0	325.0	
290°C/100bar	Lab	5.1	15.1	59.6	99.6	157.2	243.6	
	Simulation	10.2	19.2	51.7	80.6	138.5	215.3	
290°C/300bar	Lab	15.1	27.5	78.4	118.6	185.8	270.3	
	Simulation	13.8	26.2	69.3	108.3	180.9	271.5	
300°C/100bar	Lab	12.3	17.3	42.8	68.1	112.4	174.8	
	Simulation	7.4	13.9	37.6	59.9	106.8	174.6	
300°C/300bar	Lab	9.5	21.9	72.6	112.5	179.3	263.0	
	Simulation	10.4	19.7	53.7	85.1	146.9	235.3	

It can be seen from the table that the simulation results for ABS and the capillary length of 10 mm and 30 mm are well-fitting with the experimental results, indicating that the material

parameters obtained by this research method are suitable for simulating the rheometer flow under high shear rate and pressure conditions. It can also be seen from the table that as the length of the capillary increases, the difference between the simulation results and the experimental results becomes larger. For ABS, when the length of capillary from 10 mm changes to 30mm, the average difference from 1.77% increases up to 6.18%, for PA66GF30 from 2.46% up to 7.28%. The difference is similar to the research of Raha [67]. Since the measured pressure is clearly unsteady on the one hand the deviation can be attributed to the stick-slip effect (show in Figure 4.15, Figure 4.16). On the other hand, according to Stieger's research [65] who provided a valid workaround solution for the short orifice die, the effect of the boundary condition to the overall pressure prediction decreases with increasing length of the die.

Another reason for the larger deviation in case of PA66GF30 is its glass fiber content of 30 wt.%. Nevertheless, in the simulation the melt is considered to be a homogeneous material. In the experiment, the content of the reinforcing fibers can fluctuate and due to fiber breakage the fiber length distribution changes depending on the volumetric flow rate and so affects the flow of the melt. According to the following equation(4.5), the higher the volume fraction of the filler material, the higher the viscosity of the material is.

$$\eta_{filled}(\dot{\gamma}) = \frac{\tau_0}{\dot{\gamma}} + K\eta_{unfilled}(K\dot{\gamma}) \quad (4.5)$$

Where τ_0 is the yield stress due to the filler-filler network. However, it is negligibly small at the chosen shear rates [75]. The factor k is an almost linear function of the volume fraction of filler. Therefore, the simulation results of PA66GF30 fluctuate more than for ABS.

At the same time, for PA66GF30 at low shear rates the experimentally measured pressure is too low, probably resulting out of an error in pressure measurement (bad pressure propagation in the pressure hole due to the glass fiber content of 30Wt.%), so the simulation results are different from the experimental results.

Due to the study of Pang [76], the heat dissipation increases with increasing die length of the capillary in case of constant die diameter and Reynolds numbers Re lower than 200. Therefore, the actual melt temperature is probably less than the temperature chosen for the simulation, resulting in an actual viscosity being higher than the viscosity calculated in the simulation. Therefore, the calculated pressure value for a low shear rates and low back pressures will be higher.

5 Summary

Based on the material rheology, this thesis studies the rheological and thermo-dynamical properties of ABS and PA66GF30 materials and uses a modified capillary rheometer as the basis to study the flow of ABS and PA66GF30 under pressure conditions. According to the theory of rheology, the pressure dependent apparent viscosity was obtained, and the pressure coefficient β was calculated by two different methods. The true viscosity and parameters of the polymer under pressure were calculated. On this basis, Sigmasoft® software was used to simulate the flow in the high pressure capillary rheometer, which proved the applicability of the pressure dependent viscosity calculation method. The main conclusions of this thesis are as follows:

- (1) The shear viscosity, specific heat capacity, pVT curve and thermal conductivity of two polymers of ABS and PA66GF30 under atmospheric pressure were measured in the experiment. The thermal stability of PA66GF30 was also measured and the reason for thermal degradation was analyzed. It is determined that the measuring time of PA66GF30 should be controlled within 2.5 minutes.
- (2) Using the back pressure modified high pressure capillary rheometer to measure the apparent viscosity of the two materials under pressure was successful. The pressure coefficients of the viscosity were calculated by means of the definition method and the master curve fitting method. Thus, the pressure sensitivity of the polymer melts could be calculated and characterized simply and intuitively.
- (3) Comparing the determined values of ABS and PA66GF30, it was found that amorphous polymers have higher pressure coefficients than semi-crystalline polymers. It shows that the stiffness of the polymer chain and the structure of the side chain affects the pressure dependence of the shear viscosity. The study additionally found that the pressure coefficient β of ABS decreases with the increase of shear rate while the pressure coefficient β of PA66GF30 has no obvious effect on the shear rate. From this it can be concluded that the molecular structure of the polymer has a certain influence on the pressure dependence of the shear viscosity. With the increase of the network structure, the effect of shear rate on the dependence of the shear viscosity on the pressure decreases. The pressure coefficient β of ABS decreases with increasing temperature. The pressure coefficient β of PA66GF30 decreases with increasing temperature below 290°C and then increases with increasing temperature, which indicates that hydrogen bonding and polarity significantly affects the pressure dependence of temperature on shear viscosity. In general, polar materials have completely different properties from non-polar and weakly polar materials.
- (4) Through comparison of rheological experiments with simulations of the polymer melt flow of the typical capillary rheometer using pressure dependent viscosity it was found that the simulated data performed with the "mean pressure method" were more in line with the actual experimental results than the traditional "entrance pressure method".
- (5) Using Sigmasoft®, the polymer melt flow in the capillary was simulated under pressure conditions. The simulation results show that after the right choice of mesh size and material data (pressure dependent viscosity data), the simulation software can simulate the flow in the capillary rheometer and its pressure demand very well. It was shown that different capillary die lengths have a great influence on the simulation results, and

the difference between the simulation and experimental results increases with the increase of the capillary length.

Due to maximum pressure limitation on the rheometer, only the viscosity coefficient under 1/100/300bar could be measured. So it was impossible to obtain the material viscosity coefficient above 2000 bar used in the actual injection molding of thin-walled parts. The influence of the fiber content and the polymer molecular structure for the pressure dependence was shown but needs to be studied further. Hence, additional research is needed on this topic.

6 References

- [1] Duchêne, V., and Coauthors, 2016: Identifying current and future application areas, existing industrial value chains and missing competences in the EU, in the area of additive manufacturing (3D printing). *European Commission-Executive Agency for Small and Medium-sized Enterprises, Brussels, doi, 10, 72202.*
- [2] Friesenbichler, W., I. Duretek, J. Rajganes, and S. R. Kumar, 2011: Measuring the pressure dependent viscosity at high shear rates using a new rheological injection mould. *Polimery, 56, 58-62.*
- [3] Market, G. M. C.: Global Engineering Plastic Market 2020 by Manufacturers, Regions, Type and Application, Forecast to 2025. [Available online at <https://www.marketstudyreport.com/reports/global-residential-smart-thermostats-market-2020-by-manufacturers-regions-type-and-application-forecast-to-2025>.] (Accessed on January 7, 2021)
- [4] Peters, E. N., 2002: *Plastics: thermoplastics, thermosets, and elastomers.* Wiley-Interscience, New York.
- [5] da Silva, C. M. D., A. L. A. Silva, R. Pacheco, and A. M. Rocco, 2009: Conductivity and Thermal Behaviour of Sulfonated ABS Membranes for Fuel Cell Applications. *ECS Transactions, 25, 881.*
- [6] Giles Jr, H. F., E. M. Mount III, and J. R. Wagner Jr, 2004: *Extrusion: the definitive processing guide and handbook.* William Andrew.
- [7] MatWeb, L., 2018: Overview of materials for Acrylonitrile Butadiene Styrene (ABS), Extruded.
- [8] RTP.Company: Chemical & Environmental Resistance of Thermoplastics. [Available online at <https://www.rtpcompany.com/technical-info/chemical-resistance/>.] (Accessed on October 18, 2020)
- [9] Engelhardt, A., 2010: The fibre year 2009/10-A world survey on Textile and Nonwovens Industry. *Oerlikon Corporation.*
- [10] Najafi, M., 2017: Improving Mechanical Properties of Nylon and Polyester Yarns by Horizontal Isothermal Bath Method, Fiber and Polymer Science, Dissertation at North Carolina State University.
- [11] Yashiro, S., H. Sasaki, and Y. Sakaida, 2012: Particle simulation for predicting fiber motion in injection molding of short-fiber-reinforced composites. *Composites Part A: Applied Science and Manufacturing, 43, 1754-1764.*
- [12] Palmer, R. J., 2003: *Polyamides, plastics.* John Wiley and Sons Inc.
- [13] Zakaria, Z., Z. Izzah, M. Jawaid, and A. Hassan, 2012: Effect of degree of deacetylation of chitosan on thermal stability and compatibility of chitosan-polyamide blend. *BioResources, 7, 5568-5580.*
- [14] MatWeb, L.: Overview of materials for Nylon 66, Unreinforced. [Available online at <http://www.matweb.com/search/datasheet.aspx?MatGUID=a2e79a3451984d58a8a442c37a226107>.] (Accessed on Spetember 25, 2019)
- [15] Lee, J.-Y., and K.-J. Kim, 2019: MEG Effects on Hydrolysis of Polyamide 66/Glass Fiber Composites and Mechanical Property Changes. *Molecules, 24, 755.*
- [16] Ningbo Huibang PA Technology Co., L.: Glass fiber reinforced nylon composites. [Available online at <http://www.nilong.net/en/contents/58/139.html>.] (Accessed on March 6, 2020)
- [17] Denault, J., T. Vu - Khanh, and B. Foster, 1989: Tensile properties of injection molded long fiber thermoplastic composites. *Polymer composites, 10, 313-321.*
- [18] MatWeb, L.: Overview of materials for PA 66, 30% Glass Fiber Filled. [Available online at

- <http://www.matweb.com/search/datasheet.aspx?MatGUID=27ded617b5894f4b84e18f0f61f0606b>.] (Accessed on Spetember 25, 2019)
- [19] Yang, L., and K. Du, 2019: A comprehensive review on the natural, forced, and mixed convection of non-Newtonian fluids (nanofluids) inside different cavities. *Journal of Thermal Analysis and Calorimetry*, 1-22.
- [20] Bird, R. B., R. C. Armstrong, and O. Hassager, 1987: *Dynamics of polymeric liquids. Vol. 1: Fluid mechanics*. John Wiley and Sons Inc.
- [21] Hagen, G., 1839: Ueber die Bewegung des Wassers in engen cylindrischen Röhren. *Annalen der Physik*, **122**, 423-442.
- [22] Rabinowitsch, B., 1929: Über die viskosität und elastizität von solen. *Zeitschrift für physikalische Chemie*, **145**, 1-26.
- [23] Bagley, E., 1957: End corrections in the capillary flow of polyethylene. *Journal of Applied Physics*, **28**, 624-627.
- [24] Wales, J., J. Den Otter, and H. Janeschitz-Kriegl, 1965: Comparison between slit viscometry and cylindrical capillary viscometry. *Rheologica Acta*, **4**, 146-152.
- [25] Vlachopoulos, J., and D. Strutt, 2003: The role of rheology in polymer extrusion. *New Technology for Extrusion Conference. Milan, Italy. Nov*, 20-21.
- [26] Gooch, J. W., 2010: *Encyclopedic dictionary of polymers*. Vol. 1, Springer Science & Business Media.
- [27] Rudolph, N., and T. A. Osswald, 2014: *Polymer rheology: fundamentals and applications*. Carl Hanser Verlag GmbH Co KG.
- [28] Mazumder, M. A. J., H. Sheardown, and A. Al-Ahmed, 2019: *Functional Polymers*. Springer.
- [29] Münstedt, H., 2020: Influence of hydrostatic pressure on rheological properties of polymer melts—A review. *Journal of Rheology*, **64**, 751-774.
- [30] Ferry, J. D., 1980: *Viscoelastic properties of polymers*. John Wiley & Sons.
- [31] Doolittle, A. K., 1951: Studies in Newtonian flow. II. The dependence of the viscosity of liquids on free - space. *Journal of Applied Physics*, **22**, 1471-1475.
- [32] Goldblatt, P. H., and R. S. Porter, 1976: A comparison of equations for the effect of pressure on the viscosity of amorphous polymers. *Journal of Applied Polymer Science*, **20**, 1199-1208.
- [33] Penwell, R. C., R. S. Porter, and S. Middleman, 1971: Determination of the pressure coefficient and pressure effects in capillary flow. *Journal of Polymer Science Part A - 2: Polymer Physics*, **9**, 731-745.
- [34] Somcynsky, T., and R. Simha, 1971: Hole theory of liquids and glass transition. *Journal of Applied Physics*, **42**, 4545-4548.
- [35] Duretek, I., S. Schuschnigg, A. Gooneie, G. Langecker, C. Holzer, and L. Gomze, 2015: Rheological properties of wood polymer composites and their role in extrusion. *J. Phys. Conf. Ser*, 012014.
- [36] Macosko, C., 1994: *Rheology principles, measurements, and applications*, VCH Publ. Inc, New York.
- [37] Kukla, C., I. Duretek, J. Gonzalez-Gutierrez, and C. Holzer, 2018: Rheology of highly filled polymers. *Polymer rheology*, 153.
- [38] Ehrenstein, G. W., G. Riedel, and P. Trawiel, 2012: *Thermal analysis of plastics: theory and practice*. Carl Hanser Verlag GmbH Co KG.
- [39] Selvasankar, R. K., 2008: Rheological characterisation of polymer melts on an injection moulding machine using a new slit die measurement system, Institut of Plastics Processing, Master thesis at University of Leoben.
- [40] Grellmann, W., S. Seidler, and P. I. Anderson, 2007: *Polymer testing*. Hanser Munich.
- [41] Hitachi: Specific Heat Capacity Measurements Using DSC I - The Principles of Specific

- Heat Capacity Measurements and an Example Using Epoxy Resin. [Available online at https://www.hitachi-hightech.com/file/global/pdf/products/science/appli/ana/thermal/application_TA_011e.pdf.] (Accessed on September 25, 2019)
- [42] Webster, J. G., 1999: *The Measurement, Instrumentation, and Sensors: Handbook*. Springer Science & Business Media.
- [43] Aho, J., and S. Syrjälä, 2010: Measurement of the pressure dependence of viscosity of polymer melts using a back pressure - regulated capillary rheometer. *Journal of Applied Polymer Science*, **117**, 1076-1084.
- [44] De, S., J. Kuipers, and E. Peters, 2017: Viscoelastic flow simulations in disordered porous media. *Progress in Applied CFD – CFD2017 Selected papers from 12th International Conference on Computational Fluid Dynamics in the Oil & Gas, Metallurgical and Process Industries*, 451-457.
- [45] Makke, A., O. Lame, M. Perez, and J.-L. Barrat, 2012: Influence of tie and loop molecules on the mechanical properties of lamellar block copolymers. *Macromolecules*, **45**, 8445-8452.
- [46] SIGMA-Engineering: SIGMASOFT ® Virtual Molding. [Available online at <https://www.sigmasoft.de/en/about-us/>.] (Accessed on January 21, 2020)
- [47] Barus, C., 1891: Note on the dependence of viscosity on pressure and temperature. *Proceedings of the American Academy of Arts and Sciences*, JSTOR, 13-18.
- [48] Maxwell, B., and A. Jung, 1957: Hydrostatic pressure effect on polymer melt viscosity. *Mod Plast*, **35**, 174-182.
- [49] Choi, S., 1968: Determination of melt viscosity as a function of hydrostatic pressure in an extrusion rheometer. *Journal of Polymer Science Part A - 2: Polymer Physics*, **6**, 2043-2049.
- [50] Penwell, R. C., and R. S. Porter, 1971: Effect of pressure in capillary flow of polystyrene. *Journal of Polymer Science Part A - 2: Polymer Physics*, **9**, 463-482.
- [51] Cogswell, F., and J. McGowan, 1972: The effects of pressure and temperature upon the viscosities of liquids with special reference to polymeric liquids. *British Polymer Journal*, **4**, 183-198.
- [52] Christmann, L., and W. Knappe, 1974: Viskositätsmessungen an Kunststoffschmelzen mit verschiedenen Molekulargewichten. *Colloid and Polymer Science*, **252**, 705-711.
- [53] Laun, H., 1983: Polymer melt rheology with a slit die. *Rheologica Acta*, **22**, 171-185.
- [54] Driscoll, P. D., and D. C. Bogue, 1990: Pressure effects in polymer melt rheology. *Journal of applied polymer science*, **39**, 1755-1768.
- [55] Kadijk, S., and B. Van Den Brule, 1994: On the pressure dependency of the viscosity of molten polymers. *Polymer Engineering & Science*, **34**, 1535-1546.
- [56] Pantani, R., and A. Sorrentino, 2005: Pressure effect on viscosity for atactic and syndiotactic polystyrene. *Polymer Bulletin*, **54**, 365-376.
- [57] Sedlacek, T., M. Zatloukal, P. Filip, A. Boldizar, and P. Saha, 2004: On the effect of pressure on the shear and elongational viscosities of polymer melts. *Polymer Engineering & Science*, **44**, 1328-1337.
- [58] Merabia, S., and D. Long, 2008: Heterogeneous dynamics and pressure dependence of the dynamics in van der Waals liquids. *Macromolecules*, **41**, 3284-3296.
- [59] Son, Y., 2009: Measurement of pressure dependence on the shear viscosity of polymer melts. *Journal of polymer research*, **16**, 667.
- [60] Sorrentino, A., and R. Pantani, 2009: Pressure-dependent viscosity and free volume of atactic and syndiotactic polystyrene. *Rheologica acta*, **48**, 467-478.
- [61] Piyamanocha, P., T. Sedlacek, and P. Saha, 2011: On pressure affected shear viscosity of poly (lactic) acid. *AIP Conference Proceedings*, American Institute of Physics, 194-

- 200.
- [62] Li, C., F. Jiang, L. Wu, X. Yuan, and X. Li, 2015: Determination of the pressure dependence of the shear viscosity of polymer melts using a capillary rheometer with an attached counter pressure chamber. *Journal of Macromolecular Science, Part B*, **54**, 1029-1041.
- [63] Ceccia, S., C. Cocquet, L. Trouillet-Fonti, and D. R. Long, 2014: Influence of pressure on polyamide 66 shear viscosity: a case study towards polar polymers behavior. *Rheologica Acta*, **53**, 181-190.
- [64] Friesenbichler, W., A. Neunhäuserer, and I. Duretek, 2016: Rheometry of polymer melts using processing machines. *Korea-Australia Rheology Journal*, **28**, 167-174.
- [65] Stieger, S., R. C. Kerschbaumer, E. Mitsoulis, M. Fasching, G. R. Berger - Weber, W. Friesenbichler, and J. Sunder, 2020: Contraction and capillary flow of a carbon black filled rubber compound. *Polymer Engineering & Science*, **60**, 32-43.
- [66] Friesenbichler, W., A. Neunhäuserer, M. A. Fasching, and E. Mitsoulis, 2017: THE IMPORTANCE OF VISCOELASTICITY AND PRESSURE DEPENDENCE OF VISCOSITY FOR SIMULATION OF MELT FLOW IN INJECTION MOLDING AND CAPILLARY RHEOMETRY. *International Conference on Industrial Tools and Advance Processing Technologies*.
- [67] Raha, S., H. Sharma, M. Senthilmurugan, S. Bandyopadhyay, and P. Mukhopadhyay, 2020: Determination of the pressure dependence of polymer melt viscosity using a combination of oscillatory and capillary rheometer. *Polymer Engineering & Science*, **60**, 517-523.
- [68] INEOS-Styrolution: Novodur® HH-106: Material data sheet. [Available online at https://www.ineos-styrolution.com/Product/Novodur-High-Heat_Novodur-HH-106_SKU401700150417_lang_en_GB.html.] (Accessed on July 6, 2019)
- [69] Radici-group: TORZEN® G3000HR BK34: Material data sheet. [Available online at <https://www.radicigroup.com/documents/b67c2cfb-a979-41ad-8160-5e50ab8f45be>.] (Accessed on July 6, 2019)
- [70] Aho, J., and S. Syrjäälä, 2005: Evaluation of pressure dependence of viscosity for some polymers using capillary rheometer. *Annual Transactions, the Nordic Rheology Society, the Nordic Rheology Conference, Tampere, Finland*, 55-60.
- [71] Jachowicz, T., I. Gajdos, and V. Krasinskiy, 2019: Numerical Modeling of pvT Rheological Equation Coefficients for Polypropylene with Variable Chalk Content. *Open Engineering*, **9**, 668-673.
- [72] Yoshizawa, Y., H. Saitô, and K. Nukada, 1972: A direct observation of the crosslinking unit in thermally degraded polyamides. *Journal of Polymer Science Part B: Polymer Letters*, **10**, 145-151.
- [73] Hill, R., 1954: Chemical and Physical Aspects of Synthetic Fibres. *CHEMISTRY & INDUSTRY*, 1083-1089.
- [74] Gong S.G., X. G. L., Qiu A.H., et al., 2003: Discussion on the relationship between calculation accuracy and grid division in CAE simulation analysis. *Modern Machinery*, **6**, 35-38.
- [75] Menges, G., E. Haberstroh, W. Michaeli, and E. Schmachtenberg, 2014: *Menges Werkstoffkunde Kunststoffe*. Carl Hanser Verlag GmbH Co KG.
- [76] Yan, P., 2011: Numerical simulation study of liquid flow and heat transfer characteristics in microchannels, Institute of Mechanical Engineering and Applied Electronic Technology, Master thesis at Beijing University of Technology.

7 Abbreviations and symbols

Abbreviation	Meaning	Unit
α	pressure shift factor	-
β	pressure coefficient of viscosity	Pa ⁻¹
$\dot{\gamma}$	shear rate	s ⁻¹
η	viscosity	Pa·s
λ	thermal conductivity	W/(m·K)
ρ	density	kg/m ³
τ	shear stress	Pa
ω	angular velocity	rad/s
c_p	specific heat capacity	J/(kg·K)
D	diameter	m
H	height	m
L	length	m
M	moment	N·m
m	weight	kg
p	pressure	Pa
q	heat flow per length	W/m
R	radius	m
T	temperature	°C
V	volume	m ³
ABS	Acrylonitrile Butadiene Styrene	
PA	Polyamide	
PA66GF30	Polyamide 66 reinforced with 30 weight-% glass fibers	
HPCR	High pressure capillary rheometer	
TLS	Transient line source	
DSC	Differential scanning calorimetry	

8 List of tables

TABLE 2.1: ABS /PA66 /PA66-GF30 PROPERTIES [7; 14; 18]	7
TABLE 3.1: MATERIAL PROPERTIES OF ABS AND PA66GF30 [68; 69]	27
TABLE 3.2: EXPERIMENTAL INSTRUMENTS AND INFORMATION.....	27
TABLE 3.3: DRYING TYPE, TEMPERATURE AND DRYING TIME FOR THE USED MATERIALS	28
TABLE 3.4: DOE FOR THE HPCR MEASUREMENT OF ABS.....	28
TABLE 3.5: DOE FOR HPCR MEASUREMENT OF PA66GF30.....	29
TABLE 3.6: DOE FOR THE MEASUREMENTS OF ABS USING THE MODIFIED HPCR	31
TABLE 3.7: DOE FOR THE MEASUREMENTS OF PA66GF30 USING THE MODIFIED HPCR	31
TABLE 3.8: PV/T COEFFICIENTS FOR ABS IN THE MELTING TEMPERATURE RANGE.....	33
TABLE 3.9: PV/T COEFFICIENTS FOR PA66GF30 IN THE MELTING TEMPERATURE RANGE.....	34
TABLE 3.10: BEST-FIT PARAMETERS OF EQUATION (2.3) AND (2.7).....	38
TABLE 3.11: PRESSURE COEFFICIENT B FOR ABS.....	42
TABLE 3.12: PRESSURE COEFFICIENT B FOR PA66GF30	42
TABLE 3.13: PRESSURE COEFFICIENT B FOR ABS CALCULATED BY MASTER CURVE METHOD.....	46
TABLE 3.14: PRESSURE COEFFICIENT B OF PA66GF30 BY MASTER CURVE METHOD.....	46
TABLE 4.1: VISCOSITY DATA FOR ABS AT THREE SELECTED TEMPERATURES AND TWO BACK PRESSURE LEVELS USED IN THE SIGMASOFT® SIMULATION AND DETERMINED FOR THE "MEAN PRESSURE" METHOD TAKING INTO ACCOUNT THE BAGLEY AND WEISSENBERG-RABINOWITSCH CORRECTION.....	53
TABLE 4.2: VISCOSITY DATA FOR PA66GF30 AT S THREE SELECTED TEMPERATURES AND TWO BACK PRESSURE LEVELS USED IN THE SIGMASOFT® SIMULATION AND DETERMINED FOR THE "MEAN PRESSURE" METHOD TAKING INTO ACCOUT THE BAGLEY AND WEISSENBERG-RABINOWITSCH CORRECTION	54
TABLE 4.3: VISCOSITY DATA FOR ABS AT THREE SELECTED TEMPERATURES AND TWO BACK PRESSURE LEVELS USED IN THE SIGMASOFT® SIMULATION AND DETERMINED FOR THE "ENTRANCE PRESSURE" METHOD TAKING INTO ACCOUT THE BAGLEY AND WEISSENBERG-RABINOWITSCH CORRECTION	57
TABLE 4.4: COMPARISON OF SIMULATION RESULTS AND EXPERIMENTAL DATA FOR ABS AND THE CAPILLARY WITH 10 MM LENGTH	63
TABLE 4.5: COMPARISON OF SIMULATION RESULTS AND EXPERIMENTAL DATA FOR ABS AND THE CAPILLARY WITH 30 MM LENGTH	63
TABLE 4.6: COMPARISON OF SIMULATION RESULTS AND EXPERIMENTAL DATA FOR PA66GF30 AND THE CAPILLARY WITH 10 MM LENGTH	64
TABLE 4.7: COMPARISON OF SIMULATION RESULTS AND EXPERIMENTAL DATA FOR PA66GF30 AND THE CAPILLARY WITH 30 MM LENGTH	64

9 LIST OF FIGURES

FIGURE 1.1: SCIENTIFIC APPROACH OF THIS THESIS	2
FIGURE 2.1 STRUCTURE OF ABS [5]	3
FIGURE 2.2: STRUCTURE OF PA66 [13]	5
FIGURE 2.3: COMPARISON OF SHEAR STRESS VERSUS SHEAR RATE DIAGRAM FOR NEWTONIAN AND NON- NEWTONIAN FLUIDS [19].....	8
FIGURE 2.4: WEISSENBERG EFFECT [20]	9
FIGURE 2.5: DIE SWELL OF A NEWTONIAN (LEFT) VERSUS A POLYMERIC (RIGHT) LIQUID [20]	9
FIGURE 2.6: FACTORS INFLUENCING THE VISCOSITY OF POLYMER MELTS [25].....	10
FIGURE 2.7: MEANING OF CARREAU MODEL PARAMETERS [28].....	11
FIGURE 2.8: SCHEMATIC DIAGRAMS OF HIGH PRESSURE CAPILLARY RHEOMETER [35].....	13
FIGURE 2.9: SCHEMATIC DIAGRAMS OF PARALLEL PLATES ROTATIONAL RHEOMETER [37].....	15
FIGURE 2.10: PVT MEASUREMENT OF AN AMORPHOUS ABS AS A FUNCTION OF TEMPERATURE AND PRESSURE, ISOBARIC COOLING [38].....	16
FIGURE 2.11: PVT MEASUREMENT OF A SEMICRYSTALLINE PA 6 AS A FUNCTION OF TEMPERATURE AND PRESSURE, ISOBARIC COOLING [38].....	17
FIGURE 2.12: SCHEMATIC DIAGRAMS OF DIRECT METHOD PVT MEASUREMENT [38]	17
FIGURE 2.13: STRUCTURE OF A DSC MEASURING CELL (HEAT-FLOW PRINCIPLE) DISK TESTER SYSTEM [40]	18
FIGURE 2.14: DSC MEASUREMENT OF SPECIFIC HEAT CAPACITY, A) EMPTY PAN, B) SAMPLE, C) REFERENCE [41]	19
FIGURE 2.15: SCHEMATIC DIAGRAMS OF TRANSIENT LINE SOURCE METHOD [39]	20
FIGURE 2.16: SCHEMATIC OF THE MODIFIED HPCR EXPERIMENTAL SET-UP [43]	21
FIGURE 3.1: TEMPERATURE CYCLE FOR DSC MEASUREMENTS	30
FIGURE 3.2: SPECIFIC HEAT CAPACITY (C_p) VERSUS TEMPERATURE (T) CURVES OF ABS (RED) AND PA66GF30 (BLUE)	32
FIGURE 3.3: THERMAL CONDUCTIVITY (λ) AT DIFFERENT TEMPERATURES OF ABS (BLUE) AND PA66GF30 (RED).....	32
FIGURE 3.4: ISOBARIC PVT CURVES OF ABS.....	33
FIGURE 3.5: ISOBARIC PVT CURVES OF PA66GF30.....	33
FIGURE 3.6: PVT CURVES APPROXIMATED AT MELTING RANGE BY SCHMIDT EQUATION(2.23) FOR ABS. THE FITTING PARAMETER VALUES ARE GIVEN IN TABLE 3.8	34
FIGURE 3.7: PVT CURVES APPROXIMATED AT MELTING RANGE BY SCHMIDT EQUATION(2.23) FOR PA66GF30. THE FITTING PARAMETER VALUES ARE GIVEN IN TABLE 3.9	34
FIGURE 3.8: INFLUENCE OF RESIDENCE TIME ON VISCOSITY FOR PA66GF30	35
FIGURE 3.9: LOW SHEAR RATE VISCOSITY CURVES OF ABS IN THE RANGE OF 0.1 TO 500 s^{-1}	36
FIGURE 3.10: LOW SHEAR RATE VISCOSITY CURVES OF PA66GF30 IN THE RANGE OF 5 TO 500 s^{-1}	36
FIGURE 3.11: HIGH SHEAR RATE VISCOSITY CURVES OF ABS AT DIFFERENT TEMPERATURES	37
FIGURE 3.12: HIGH SHEAR RATE VISCOSITY CURVES OF PA66GF30 AT DIFFERENT TEMPERATURES	37
FIGURE 3.13: VISCOSITY VERSUS SHEAR RATE FOR ABS WITH 1BAR/100BAR/300BAR BACK PRESSURE AT DIFFERENT TEMPERATURES.....	38
FIGURE 3.14: VISCOSITY CURVES FOR PA66 WITH 1BAR/100BAR/300BAR BACK PRESSURE AT DIFFERENT TEMPERATURES	39
FIGURE 3.15: LOGARITHM OF VISCOSITY $\ln(\eta)$ VERSUS MEAN PRESSURE (P_M) CURVES OF ABS AT 230°C	39
FIGURE 3.16: LOGARITHM OF VISCOSITY $\ln(\eta)$ VERSUS MEAN PRESSURE (P_M) CURVES OF ABS AT 250°C	40

9. LIST OF FIGURES

FIGURE 3.17: LOGARITHM OF VISCOSITY $\ln(H)$ VERSUS MEAN PRESSURE (P_M) CURVES OF ABS AT 270°C	40
FIGURE 3.18: LOGARITHM OF VISCOSITY $\ln(H)$ VERSUS MEAN PRESSURE (P_M) CURVES OF PA66GF30 AT 280°C	40
FIGURE 3.19: LOGARITHM OF VISCOSITY $\ln(H)$ VERSUS MEAN PRESSURE (P_M) CURVES OF PA66GF30 AT 290°C	41
FIGURE 3.20: LOGARITHM OF VISCOSITY $\ln(H)$ VERSUS MEAN PRESSURE (P_M) CURVES OF PA66GF30 AT 300°C	41
FIGURE 3.21: PRESSURE COEFFICIENT B AS A FUNCTION OF SHEAR RATE FOR ABS IN ACCORDANCE WITH EQUATION (2.34)	43
FIGURE 3.22: PRESSURE COEFFICIENT B AS A FUNCTION OF SHEAR RATE FOR A66GF30 IN ACCORDANCE WITH EQUATION (2.34)	43
FIGURE 3.23: EVOLUTION OF THE PRESSURE COEFFICIENT B WITH TEMPERATURE FOR PA66 AT 224 s ⁻¹ (CIRCLE) AND 447 s ⁻¹ (SQUARE). DATA ARE DRAWN FROM CECCIA [63]	44
FIGURE 3.24: VISCOSITY MASTER CURVES INDEPENDENT OF PRESSURE FOR ABS (REFERENCE AT ATMOSPHERIC PRESSURE), SHIFT FACTORS a_P ESTIMATED FROM CAPILLARY RHEOMETER DATA	45
FIGURE 3.25: VISCOSITY MASTER CURVES INDEPENDENT OF PRESSURE FOR PA66GF30 (REFERENCE AT ATMOSPHERIC PRESSURE), SHIFT FACTORS a_P ESTIMATED FROM CAPILLARY RHEOMETER DATA	45
FIGURE 3.26: PRESSURE COEFFICIENT B FOR ABS ESTIMATED BY THE DEFINITION AND THE SUPERPOSITION METHOD	47
FIGURE 3.27: PRESSURE COEFFICIENT B FOR PA66GF30 ESTIMATED BY THE DEFINITION (BARUS EQUATION) AND THE SUPERPOSITION METHOD	47
FIGURE 4.1: THE 3D SOLID MODELING OF THE RHEOMETER DIE AND THE PRESSURE HOLE WITH THE PRESSURE SENSOR	50
FIGURE 4.2: MESH SIZE AND QUALITY FOR THE CAPILLARY WITH 0.2MM MESH LENGTH	50
FIGURE 4.3: PRESSURE HOLE WITH THIN WALL CELLS OF 0.2MM MESH LENGTH	51
FIGURE 4.4: MESH SIZE AND QUALITY FOR THE CAPILLARY WITH 0.1MM MESH LENGTH	51
FIGURE 4.5: LOCATION OF THE TWO WALL CELLS AND THE CONTRACT CELLS OF 0.1MM MESH LENGTH ...	52
FIGURE 4.6: YOUNG'S MODULUS OF THE SELECTED MOLD STEEL	52
FIGURE 4.7: VISCOSITY VERSUS SHEAR RATE AT 230/250/270°C FOR ABS; CURVES FITTED WITH SIGMADATA	55
FIGURE 4.8: CROSS-WLF MODEL PARAMETERS FOR ABS, FITTED WITH SIGMADATA	55
FIGURE 4.9: VISCOSITY VERSUS SHEAR RATE AT 280/290/300°C FOR PA66GF30; CURVES FITTED WITH SIGMADATA	56
FIGURE 4.10: CARREAU-WLF MODEL PARAMETERS FOR PA66GF30, FITTED WITH SIGMADATA	56
FIGURE 4.11: VISCOSITY VERSUS SHEAR RATE CURVES FOR ABS, EXPERIMENTAL RESULTS AND CALCULATED CURVES USING SIGMASOFT® SIMULATIONS	58
FIGURE 4.12: VISCOSITY VERSUS SHEAR RATE CURVES FOR PA66GF30, EXPERIMENTAL RESULTS AND CALCULATED CURVES USING SIGMASOFT® SIMULATIONS	58
FIGURE 4.13: SIMULATED PRESSURE IN THE CYLINDRICAL FILLING CHAMBER AND THE CAPILLARY	59
FIGURE 4.14: SIMULATED PRESSURE VERSUS TIME FOR ABS	59
FIGURE 4.15: SIMULATED PRESSURE VERSUS TIME FOR PA66GF30	60
FIGURE 4.16: MELT FRACTURE PHENOMENON IN LAB EXPERIMENT FOR PA66GF30	60
FIGURE 4.17: SIGMASOFT® SIMULATION AND CAPILLARY PRESSURE CURVES VERSUS TIME OF THE EXPERIMENTS FOR ABS (T=270°C, 300 BAR BACK PRESSURE); 0.2 MM MESH LENGTH (BLUE), 0.1 MM MESH LENGTH (RED), LAB RESULTS (BLACK)	61
FIGURE 4.18: SIGMASOFT® SIMULATION AND PRESSURE CURVES VERSUS TIME OF THE EXPERIMENTS FOR ABS (T=270°C, 300 BAR BACK PRESSURE); ENTRANCE PRESSURE PROCESSED (BLUE), MEAN PRESSURE PROCESSED (RED), LAB RESULTS (BLACK)	62

10 Appendix

Table 10.1 Viscosity versus shear rate for ABS at atmospheric pressure

230°C	shear rate	58.6	115.5	391.8	710.5	1575.8	3448.6
	viscosity	988.7	784.6	405.2	279.9	160.0	88.4
250°C	shear rate	57.1	111.9	364.6	651.5	1431.2	3103.8
	viscosity	620.8	527.4	297.6	219.0	134.7	78.3
270°C	shear rate	54.9	107.8	349.5	617.7	1347.0	2896.6
	viscosity	395.3	348.4	221.6	167.4	108.6	65.2

Table 10.2 Viscosity versus shear rate for ABS with 100bar back pressure

230°C	shear rate	50.7	126.8	479.0	864.0	1872.8	3993.1
	viscosity	2218.3	1272.9	516.5	336.2	184.1	99.5
250°C	shear rate	50.7	117.4	420.7	747.1	1603.3	3386.6
	viscosity	1283.1	843.0	403.4	277.9	162.8	92.5
270°C	shear rate	50.7	114.4	398.9	703.2	1498.0	3156.7
	viscosity	851.4	597.5	308.3	218.8	132.6	78.0

Table 10.3 Viscosity versus shear rate for ABS with 300bar back pressure

230°C	shear rate	50.9	126.9	484.5	877.2	1909.6	4069.2
	viscosity	2600.8	1461.1	586.0	380.4	207.9	111.8
250°C	shear rate	52.1	126.5	456.7	816.5	1765.6	3729.9
	viscosity	1776.5	1095.1	463.4	307.7	173.4	94.8
270°C	shear rate	52.3	116.2	399.2	703.4	1487.6	3113.1
	viscosity	1013.4	704.7	362.4	260.8	157.0	91.5

Table 10.4 Viscosity versus shear rate for PA66GF30 at atmospheric pressure

280°C	shear rate	109	326.7	561.6	1196.9	2538.8	3977.1
	viscosity	323.65	245.16	204.36	150.91	98.1	77.17
290°C	shear rate	107.9	328	563.6	1185.8	2487.7	3850.7
	viscosity	264.28	201.01	172.81	129.1	86.77	68.62
300°C	shear rate	117.7	330.6	545.5	1109.6	2319.2	3576.5
	viscosity	164.8	116.3	100.5	84.5	64.1	51.1

Table 10.5 Viscosity versus shear rate for PA66GF30 with 100bar back pressure

280°C	shear rate	90.31	311.93	545.37	1152.2	2412.41
	viscosity	216.23	237.61	206.28	153.93	107.02
290°C	shear rate	98.23	324.12	560.05	1167.99	2415.35
	viscosity	222.36	200.90	171.39	127.20	86.66